Study of Magnetic Reconnection in Turbulent Plasma Using Satellite Data

Alexandros Chasapis

UNIVERSITÉ PARIS-SUD

ÉCOLE DOCTORALE 127 :
ASTRONOMIE ET ASTROPHYSIQUE D'ÎLE-DE-FRANCE

Laboratoire de Physique des Plasmas

THÈSE DE DOCTORAT

PHYSIQUE

par

Alexandros CHASAPIS GIANNAKOPOULOS

Étude de la reconnexion magnétique dans les plasmas turbulents à partir des données satellites

Date de soutenance : 28 Septembre 2015

Composition du jury :

Directeur de thèse :	Patrick CANU	Directeur de recherce (LPP)
Rapporteurs :	Benoit LAVRAUD	Charge de recherche (IRAP)
	William MATTHAEUS	Professeur (University of Delaware)
Examinateurs :	Karine BOCCHIALINI	Professeur (IAS)
	Alessandro RETINO	Charge de recherche (LPP)
	Pierre HENRI	Charge de recherche (LPC2E)
Membres invités :	Fouad SAHRAOUI	Charge de recherche (LPP)
	Jonathan EASTWOOD	Lecturer (Imperial College London)

Université Paris-Sud
DOCTORAL SCHOOL OF ASTRONOMY AND ASTROPHYSICS

Study of Magnetic Reconnection in Turbulent Plasma Using Satellite Data

Alexandros Chasapis Giannakopoulos

Doctoral Thesis

Supervisor: Patrick Canu

Laboratoire de Physique des Plasmas

CNRS / Ecole Polytechnique / Univ. Paris-Sud / UPMC / Observatoire de Paris

March 2016

“Le total peut être faux, mais le détail est vrai, pour une illusion du reel”

Acknowledgements

First of all I would like to thank Alessandro Retino for his guidance and support and patience, quite often way beyond what anyone could reasonably expect, through which I learned more than a few things about becoming a scientist. I would also like to thank Fouad Sahraoui for his scientific insights and contribution, as well as my thesis director, Patrick Canu for offering his perspective and experience during my thesis. I would like to acknowledge William Matthaeus and Benoit Lavraud for their time and effort as examiners of my thesis, as well as for their insightful and thorough comments on my work. Acknowledgments also are due to the president of my thesis committee Karine Bocchialini and the members Piere Henri, and Jonathan Eastwood, for their kind participation, their thoughtful comments and motivating discussion. Having spent four years at this laboratory, I must thank the Space Plasma group as well as everyone at LPP. I have to thank Colette Jan, Maryline Benzin, Nicolas Marsac and Bruno Katra for their invaluable administrative and technical support. I have to mention the productive and ongoing collaboration with David Sundkvist, Luca Sorisso-Valvo, Antonella Greco and Sergio Servidio, that gave rise to many of the results presented here and which will hopefully continue to be as fruitful and engaging. I am very grateful to Andris Vaivads, Yuri Khotyaintsev and everyone at the IRF Upsalla institue for their collaboration and their amazing work. The instrument teams of PEACE, EFW, FGM, STAFF and WHISPER as well as the CAA/CSA provided high quality data, thorough documentation, support and being responsive in every aspect from instrument operations to calibration all the way to the science output. I must recognize that this work would have not been possible without the support of the the doctoral school of Astronomy and Astrophysics, the Observatory of Paris and the Universite Paris-Sud. During the last 4 years, I had the chance to work with a real heavyweight, Khurom Kyiani, and profit from his turbulent perspective that amply offered, unique lessons about data analysis, life and plasma turbulence. Special thanks go to Sergey Stepanyan, Claudia Rossi, Lina Hadid, Katy Ghantous, Sumire Kobayashi, Ozgur Gurcan, Pierre Morel for the suspiciously long coffee breaks, and the associated intriguing discussions and valuable insights. Finally, I would like to thank Juliette Angotti for being a source of admiration, amazement, motivation and courage, and for enabling me to push through this whole mess.

Thank you.

Abstract

Study of Magnetic Reconnection in Turbulent Plasma Using Satellite Data

by Alexandros Chasapis Giannakopoulos

Magnetic reconnection is a fundamental energy conversion process in plasma. It occurs in thin regions of strong current known as current sheets and results in particle heating and acceleration. In turbulence, which is ubiquitous in space plasma, magnetic reconnection has been observed to occur in small scale structures that form therein, and is thought to contribute to dissipation of turbulent energy at kinetic scales. For this work we examine data from the Cluster spacecraft in the Earth's magnetosheath, downstream of the quasi-parallel shock. The detection of ion-scale current sheets was performed by implementing the Partial Variance of Increments (PVI) method for multiple spacecraft. The properties of the observed current sheets were different for high (> 3) and low (< 3) values of the PVI index. We observed a distinct population of high PVI (> 3) structures that accounted for $\sim 20\%$ of the total. Those current sheets have high magnetic shear ($> 90 degrees$). In order to estimate the local heating occurring within those current sheets, a proxy of the electron temperature was obtained at high time resolution ($125 ms$) from the partial distributions measured by Cluster. This allowed for the first time to study the localized electron heating within ion-scale current sheets. The observed enhancement of the estimated electron temperature within the high PVI current sheets suggest that they are important for local electron heating and energy dissipation. We also examined measurements inside the diffusion region of a thin reconnecting current sheet. Multi-spacecraft observations allow as to study electron distributions and wave activity at different distances from the x-line. Significant differences were observed in the electron populations as they were heated going through the current sheet. In particular electrons were heated in the direction parallel to the magnetic field in close proximity to the x-line, whereas no significant variation was observed in the perpendicular direction. However, the distribution was more isotropic downstream of the x-line with electrons heated in the perpendicular direction.

Resumé

Étude de la reconnexion magnétique dans les plasmas turbulents à partir des données satellites

by Alexandros Chasapis Giannakopoulos

La reconnexion magnétique est un mcanisme fondamental de conversion d'énergie dans le plasma. Il se déroule dans les régions minces de fort courant appelées couches de courants, et produit le chauffage et l accélération des particules. Dans un milieu turbulent, la reconnexion magnétique a été observée dans de petites structures qui se forment dans celui-ci, et on a postulé que cela contribue de façon importante la dissipation de l'énergie turbulente l'échelle cinétique. Pour ce travail, nous examinons les données des satellites Custer dans la magnétogaine de la Terre, en aval du choc quasi-parallèle. La dtection des couches de courant d'échelle ionique a été réalise par l'application de la méthode de la variance partielle des incréments (PVI) pour des satellites multiples. Les propriétés des couches de courant observées étaient différentes pour des valeurs de l'indice PVI élevées ($PVI > 3$) et bas ($PVI < 3$). Nous avons observ une population distincte de haut indice PVI (> 3) structures qui représentaient $\sim 20\%$ du total. Ces couches de courant ont une rotation du champ magnétique élevé ($> 90^o$). Afin d'estimer le chauffage local survenant dans ces couches de courant, une estimation de la temprature des électrons a été obtenue à haute résolution temporelle ($125ms$) par les distributions d'électrons partielles mesurées par Cluster. Cela a permis pour la première fois d'tudier le chauffage d'électrons localisés dans les couches de courant d'échelle ionique. L'augmentation observée de la température des électrons estimée dans les couches de courant aux PVI élevés suggèrent qu'ils sont importants pour le chauffage local d'électrons et de dissipation d'énergie. Nous avons également examiné les mesures l'intérieur de la région de diffusion d'une couche de courant o la reconnection magnétique est en cours. Les observations simultanées par des satellites multiples permettent aussi d'étudier les distributions d'électrons et l'activité des ondes à des distances différentes de la ligne x. Des différences significatives ont été observées dans les populations d'électrons comme ils ont été chauffés en passant par la couche de courant. En particulier, les électrons sont chauffés dans la direction parallèle au champ magnétique proximité de la ligne x, alors qu'aucune

variation significative n'a été observée dans la direction perpendiculaire. Cependant, la distribution est plus isotrope en aval de la ligne x, chauffées par des électrons dans la direction perpendiculaire.

Contents

List of Figures

List of Tables

Chapter 1

Introduction

A fundamental question in space and astrophysical plasma is how electromagnetic energy is dissipated into energy of charged particles in the form of heating and acceleration to high energies. Understanding energy dissipation and particle energization is crucial to explain important phenomena such as e.g. stellar flares, the heating of stellar coronae, stellar winds and accretion disks as well as particle acceleration in supernovae remnants and astrophysical jets. A number of energization mechanisms are considered to explain such phenomena which often invoke shocks, turbulence and magnetic reconnection or a combination of them.

Magnetic reconnection is one of the most important dissipation and energization mechanisms in plasma [116]. The idea that magnetic field lines can break and reconnect was first suggested by Dungey [32] and consequently formalized in a first model by Sweet and Parker [106, 142]. Since then, magnetic reconnection has been studied in a wide range of very different environments ranging from laboratory experiments dealing with laser and fusion plasma, to planetary magnetospheres, the solar wind, the solar corona as well as supernova remnants and active galactic nuclei in astrophysics [162] (Figure 1.2). It has been at the core of research in magnetic confinement in tokamaks, solar flares and the coronal heating, stellar and planetary dynamos, planetary and terrestrial mangetospheres and finally closer to Earth in the study of space weather and geomagnetic storms. As noted by Cowley and Peoples [21] the prevalence of magnetic reconnection is not a symptom of redundancy but of the underlying importance of this process.

As will be discussed in detail in the next chapter, reconnection takes place at boundaries that separate regions of different magnetic field. Such boundaries are

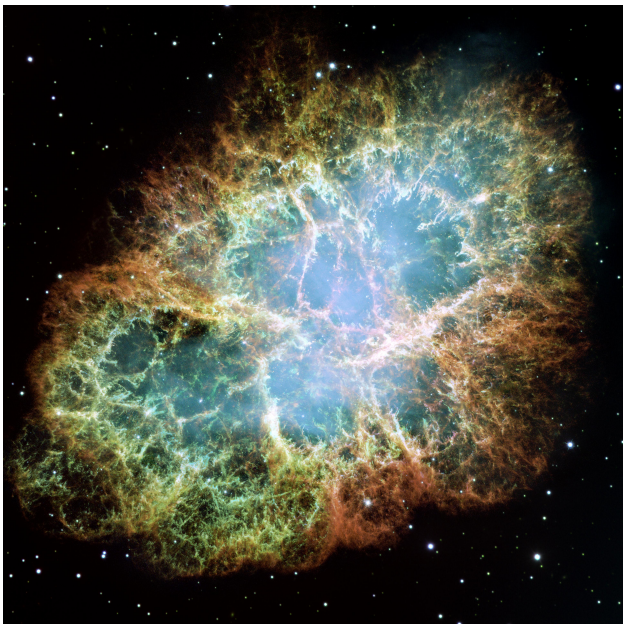

FIGURE 1.1: The Crab nebula as observed by the Hubble Space Telescope. This supernova remnant is an example of a highly turbulent region. Image Credit: NASA, ESA, J. Hester, A. Loll (ASU)

thin sheet-like regions of strong current, often referred to as current sheets. Magnetic field lines break within current sheets due to microphysical processes so that previously separated field lines on either sides of the current sheet get connected. This change in the magnetic topology leads to energy dissipation within the current sheet that results in plasma being heated and accelerated away in the form of reconnection jets, as well as particles being accelerated to high energies. Despite the fact that reconnection has been studied for decades through both theory/simulations and observations and much evidence of reconnection do exist, a number of key questions remain open, such as how reconnection starts (the so-called onset), how it proceeds in time (reconnection rate) and how exactly particles are heated and accelerated.

Plasma turbulence, on the other hand, is another fundamental phenomenon at the center of many areas of plasma research. Not only is turbulence ubiquitous in plasma, but additionally its inherently nonlinear and multi-scale behavior are at the heart of many long-standing problems associated with attempts to model this phenomenon [9]. A central property of turbulence, which is present both in neutral fluids and magnetized plasma, is the energy cascade. Energy is injected at large scales which stirs the fluid creating eddies. These eddies interact with each other creating smaller and smaller eddies, effectively creating an energy cascade that transfers the injected energy to smaller scales. At small scales this energy

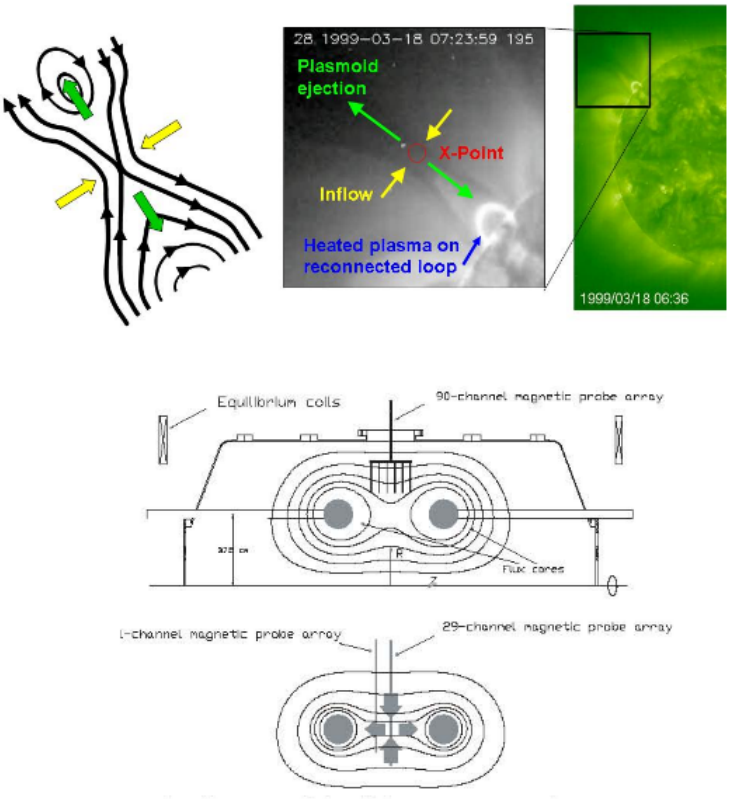

FIGURE 1.2: Examples of magnetic reconnection in different environments. Upper panel: Solar corona. Right: Image of the Sun in EUV from SOHO/EIT. Center: Image of the reconnection region in EUV showing evidence of plasma inflow into the current sheet [158]. Left: Schematic of the reconnection region. Yellow and green arrows represent plasma inflow and outflow respectively. Lower panel: Laboratory plasma (MRX experiment) [122]. The reconnection X-line is created by the merging of the magnetic field produced by two different coils. Grey arrows represent plasma inflow and outflow.

is eventually dissipated. The general description of this energy cascade has been found to be surprisingly similar in wildly different systems ranging from turbulent streams in rivers on Earth to the magnetosheath around the Earth and the turbulent solar wind in the interplanetary space. The dissipation of energy at small-scales, however, depends on the system. In the case of the river flow the dissipation is due to the viscous forces of the water, whereas in the case of most space plasma, such as the solar wind plasma studied in this thesis, it is due to processes occurring at kinetic scales, of the order of particle gyroradia and below, since in such plasma direct collisions between particles are absent or very infrequent. An important property of the turbulent energy cascade in space plasma is its spatial non-uniformity, that is often referred to as intermittency, and is associated with the presence of transient structures of different scales such as current sheets, magnetic islands, localized magnetic flux tubes, vortex structures, etc. Such coherent

structures are of particular importance at kinetic scales where they are sites of patchy but very efficient energy dissipation and particle heating.

Given that magnetic reconnection is a fundamental energy conversion process in plasma and turbulence is essentially omnipresent in space plasma, it is important to investigate the interplay between magnetic reconnection and turbulence [92]. There are two main directions from which this interplay can be approached [92]. The first is to consider the effect of turbulence on reconnection. In the case of a large scale planar boundary for example, turbulent fluctuations will perturb this relatively steady configuration. Diffusive effects of magnetic field and plasma are enhanced, the planar current sheet that defines the boundary becomes unstable and breaks down enhancing the reconnection process, while the fluctuations of the plasma flow mean that the process is neither steady nor continuous [24, 74, 90]. The second approach to the interplay between magnetic reconnection and turbulence is to look into the effect that reconnection has on turbulence. As mentioned above, the abundance of intermittent structures is a typical property of turbulent plasma. A subset of those structures are small-scale thin current sheets that can be sites of magnetic reconnection, and are a key component of the turbulence [124, 134, 135, 141]. It has been proposed that the dissipation of the magnetic field energy through reconnection is an important part of the observed turbulent dissipation at kinetic scales, and may lead to significant particle heating and acceleration [135, 141].

In the context of observations in space plasma, magnetic reconnection mostly takes place in two cases. The first is at large scale boundaries such as the Earth's magnetopause and the magnetotail. This kind of reconnection has been extensively studied in the last few decades. The second case is in small-scale current sheets that spontaneously form in turbulence. Such turbulent reconnection is the focus of the experimental research presented in this thesis. This broad categorization is instructive, but by no means strict, since there exists a range of examples that fall in between those two categories such as the reconnection taking place at the leading edge of coronal mass ejections in the solar wind. In situ spacecraft observations of turbulent reconnection are relatively recent. Intermittent structures such as current sheets have been the subject of several observational studies in solar wind plasma [20, 97, 111, 155, 161]. A few observations have provided direct evidence of reconnection in such current sheets [20, 44, 105, 124, 141] and shown that turbulent reconnection can significatively contribute to the energy dissipation and particle

heating and acceleration. However, observational studies remain relatively scarce, and the properties of turbulent reconnection as well as the impact of reconnection in turbulence have not been fully investigated.

In this thesis, I have studied turbulent reconnection by using *in situ* spacecraft data. In situ measurements of electromagnetic fields and particle distributions functions are required to understand the basic physics behind turbulent reconnection and associated particle energization. Such measurements are not available for distant astrophysical plasma and the information we have on such plasma mostly comes from the radiation they emit and that we remotely observe. Therefore, studying turbulent reconnection through *in situ* observations is also very important to help understanding if and how this mechanism is behind such emissions and ultimately assess many energetic phenomena in the plasma Universe. I used Cluster spacecraft measurements carried out in the near-Earth space, specifically in the magnetosheath downstream of the quasi parallel shock. It is a region of strong turbulence between the bow shock and the Earth's magnetopause (Figure 1.3) where the solar wind having passed the bow shock slows down and is deflected around the Earth. As this happens, the plasma is heated and strong turbulence is generated [82] while an abundance of small-scale intermittent structures is formed by the turbulence [63, 141, 159]. This region is one of the most turbulent in near-Earth space and its proximity allows for spacecrafts to perform high quality in situ measurements, offering a privileged environment for such a study. As discussed in more detail in Chapter 3, the Cluster mission (`http://sci.esa.int/cluster/`), launched by the European Space Agency in 2000, consists of four spacecraft flying in formation around the Earth which provided for the first time high quality multi-spacecraft measurements at different spatial scales. This provides numerous advantages compared to single spacecraft missions, such as being able to differentiate spatial from temporal variations and estimate quantities such as the electric current. The MMS mission (`http://mms.gsfc.nasa.gov/`), that was recently launched by NASA, as well as proposed future missions such as THOR (`http://thor.irfu.se/`), will allow further exploration of this subject.

The overall goal of this thesis was to focus on three main open questions related to turbulent reconnection. First, trying to understand which intermittent small-scale structures that form in turbulence contribute most to dissipation, through which mechanism and to what extent. Second, for the specific case of turbulent magnetic reconnection, which are the physical mechanisms that lead to particle heating

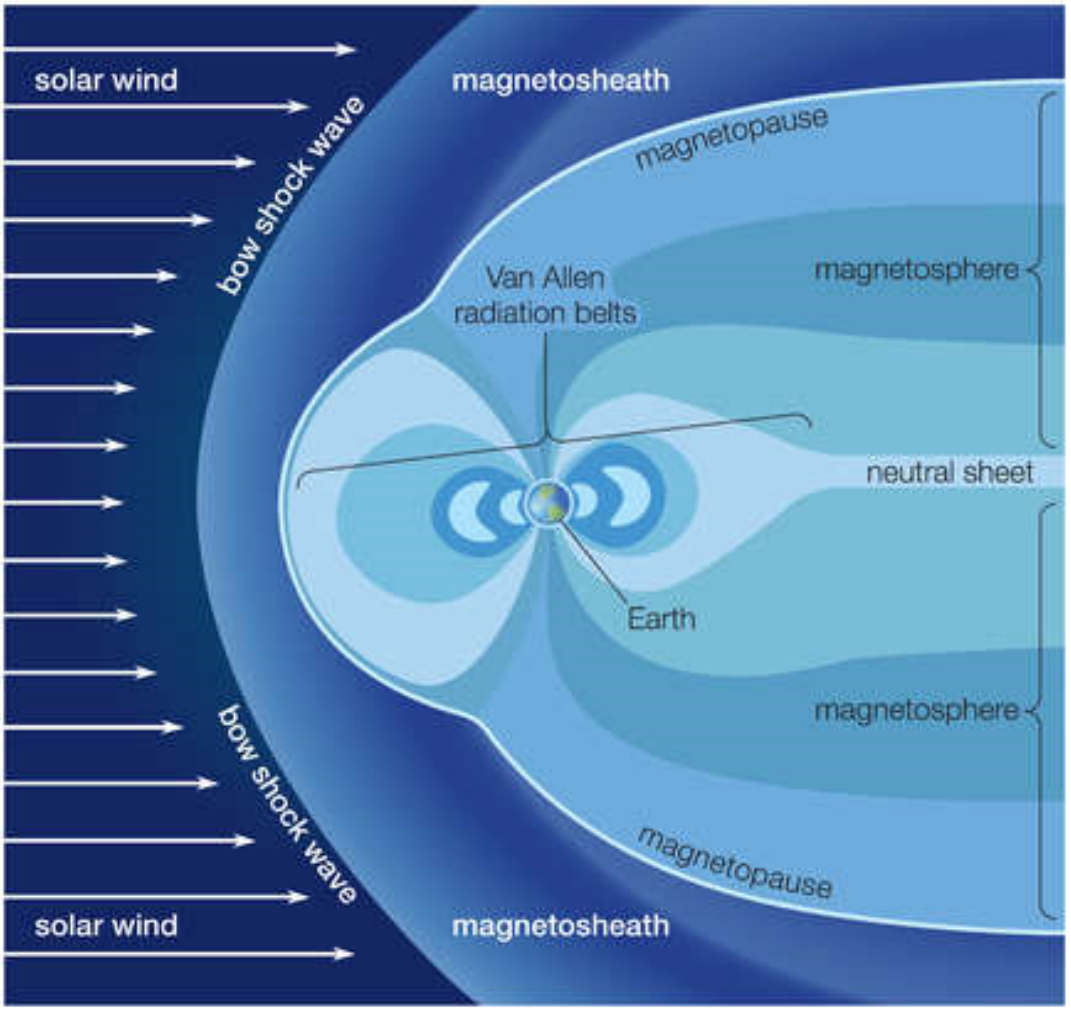

FIGURE 1.3: Diagram of near-Earth space. Solar wind blows from the left to the right. A bow shock is formed at the interface between the Earth's magnetic field and the interplanetary magnetic field as the solar wind impacts Earth's magnetosphere. The magnetosheath is the turbulent region that is formed between the bow shock and the magnetopause where the solar wind plasma is decelerated and heated.

and acceleration. Third, how important is the overall contribution of magnetic reconnection to the dissipation of energy at kinetic scales in turbulence. As a result of my research work, I have been able to partially address these questions.

The first part of this work focused on the detection of current sheets in the turbulence of the quasi-parallel magnetosheath and the examination of their properties, in order to investigate their contribution to dissipation and whether their characteristics are consistent with magnetic reconnection. Past studies have used the Partial Variance of Increments method (PVI) in order to identify intermittent structures of strong current [47, 48, 104]. Furthermore, numerical studies [135]

and recent solar wind observations [105] have established links between intermittent structures such as current sheets and magnetic reconnection. Additionally, recent kinetic simulations [63] have argued that magnetic reconnection is common in thin current sheets that are formed in the magnetosheath downstream of the quasi-parallel bow shock. Therefore, a more robust observational verification of this result was needed. Following this approach, the first step was the detection of intermittent structures of strong current using the PVI method. The next step was to try to estimate electron heating within those structures. Estimating the electron heating within thin current sheets is essential for the study of turbulent reconnection and dissipation at kinetic scales. However, this requires measurements of the electron temperature at high time resolution. The time resolution of electron temperature calculated on board the Cluster spacecraft is not sufficient. Therefore, the electron temperature was estimated using partial electron distribution functions which are provided at sufficiently high time resolution. This led to a statistical study of ion-scale current sheets that has provided evidence of local electron heating in such sheets and that has been published in [17].

The second part of this work was devoted to the examination of the mechanisms of electron heating within thin reconnecting current sheets. Numerical and observational studies have tried to answer relevant questions for large-scale reconnection in the Earth's magnetopause and magnetotail [22, 36, 45, 125, 136]. However, the electron heating mechanisms have not been investigated so far for the case of turbulent thin current sheets. Therefore, a detailed analysis of observations of a reconnecting thin current sheet was performed in an attempt to investigate the underlying mechanisms of electron heating. I focused on one case for which the electron distribution function was measured for both directions parallel and perpendicular to the magnetic field. Additionally, two of the four Cluster spacecraft crossed the current sheet simultaneously at different distances from the center of the reconnecting region, providing measurements in different regions within the current sheet. Analyzing the magnetic and electric fields, wave emissions as well as the electron temperature and distribution functions, lead to an investigation of the possible mechanisms of electron heating.

The contents of this thesis are organized as follows. After this introduction, Chapter 2 outlines the theoretical framework of this research. Chapter 3 presents the characteristics the Cluster instruments used and their data products. Chapter 4 details the data analysis methods that was used and the tests and diagnostics that

were performed to validate them. Chapter 5 summarizes the research results and is divided in two parts. The first part concerns the statistical study of ion-scale current sheets and their properties, focusing on the electron heating within those structures.The second part presents an investigation of the electron heating within the diffusion region of a specific reconnecting current sheet. Finally, Chapter 6 presents my concluding remarks and offers some future perspectives.

Chapter 2

Theoretical Background

A plasma is an ionized gas. Contrary to a usual fluid, a plasma is composed of charged particles. It is electrically conductive and therefore interactions are controlled by electromagnetic fields. The charged particles respond to the surrounding electromagnetic fields and in turn the movement of those particles modifies the electromagnetic fields. A number of different models can be used to describe a plasma, depending on the level of details that one needs to consider [7]. In the so-called magnetohydrodynamics (MHD), the plasma is described as a conducting fluid through the combination of the equations of hydrodynamics and Maxwell's equations. This description is valid at spatial scales much larger than ion gyroradius and at temporal scales much larger than the ion gyrofrequency. As such, MHD is not appropriate to address kinetic effects occurring at scales below particle gyroradius. In a two-fluid model, the ions and electrons are treated as separated fluids and such model can reproduce those effects due to the different dynamics of those species, such as Hall physics. Kinetic models of plasmas such as particle-in-cell (PIC) and Vlasov models take into account the full description of plasmas in terms of particle kinetics and distribution functions and provide the most complete description, including full distribution functions of particles. Hybrid models, where ions are treated as full particles while electrons as a fluid, are used in problems where understanding ion kinetics is sufficient.

The grand majority of ordinary matter in the universe exist in the form of plasma. For example, the stars or the matter in the intergalactic and intracluster medium are mostly in the plasma state. While we are constrained to remote observations of these systems, the solar system in general and the near-Earth space in particular

have offered a unique opportunity to perform in situ studies of space plasma. Plasma in near-Earth space is comprised mainly of electrons and protons, with small amounts of heavier ions. Its density is rather low, of the order of $\sim 1 - 10cm^{-3}$, which is several orders of magnitude lower than what would be considered industrial vacuum on Earth's laboratories. As such, collisions between particles are generally negligible, and the plasma can be considered collisionless. As mentioned in the introduction, this work will focus on investigating aspects of turbulent reconnection in small-scale current sheets, and in situ space observations in the Earth's magnetosheath provide a privileged environment for that research.

2.1 Magnetic Reconnection

Magnetic reconnection is a fundamental plasma physics process during which a change of the topology of the magnetic field occurring at small scales leads to energy dissipation and plasma transport, heating and acceleration at large scales [116]. Reconnection takes place at the boundary of different magnetic fields, which is a region of strong current usually referred to as current sheet. The change of the magnetic topology associated with reconnection is related to the violation of the so-called frozen-in condition in a small region within the current sheet, which is usually referred to as the diffusion region. This process can be understood as follows. In the context of the ideal MHD, where resistivity is zero, the magnetic field lines move together with the plasma with their topology being conserved. This is the frozen-in condition which can be illustrated as follows. Consider the magnetic flux Φ through a surface S defined by a closed contour C (Figure 2.1):

$$\Phi = \int_S \vec{B} \cdot d\vec{S} \tag{2.1}$$

The magnetic flux Φ can change in time due to a change of the magnetic field:

$$\frac{\partial \Phi}{\partial t} = \int_S \frac{\partial \vec{B}}{\partial t} \cdot d\vec{S} = -\int_S \nabla \times \vec{E} \cdot d\vec{S} \tag{2.2}$$

or by a movement of the surface S with a velocity $\vec{v}$:

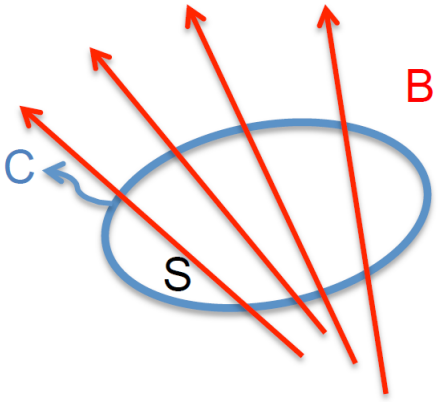

FIGURE 2.1: Magnetic flux through a surface S defined by a closed contour C.

$$\frac{\partial \Phi}{\partial t} = \int_C \vec{B} \cdot \vec{v} \times d\vec{l} = \int_C \vec{B} \times \vec{v} \cdot d\vec{l} = \int_S \nabla \times (\vec{B} \times \vec{v}) \cdot d\vec{S} \tag{2.3}$$

Combining the two relations gives:

$$\frac{d\Phi}{dt} = -\int_S \nabla \times (\vec{E} + \vec{v} \times \vec{B}) \cdot d\vec{S} \tag{2.4}$$

Since from Ohm's law we have $\vec{E} + \vec{v} \times \vec{B} = \eta \vec{J}$, and for a perfectly conductive plasma $\eta = 0$, therefore the right hand side of this equation is zero. Under such condition, the magnetic flux is conserved and the magnetic field lines must move with the plasma, meaning that the frozen-in condition holds. This also implies that no parallel electric fields can exist, as one can easily see by projecting the relation $\vec{E}+\vec{v}\times\vec{B} = 0$ along the magnetic field direction. Under such conditions, no reconnection is allowed. Yet, due to microphysical plasma processes, the frozen-in condition can be locally violated in the diffusion region so that adjacent magnetic field lines can change their connectivity, leading to a re-arrangment of the magnetic field. Such microphysical processes are able to produce a parallel electric field such that $\vec{E} + \vec{v} \times \vec{B} \neq 0$, which brings to the appearance of non-ideal terms on the right-hand side of the Ohm's law, as discussed in more detail below. A non-zero parallel electric field is therefore often used as a general definition of magnetic reconnection [131].

$$\int_S \vec{E}_{||} ds \neq 0 \tag{2.5}$$

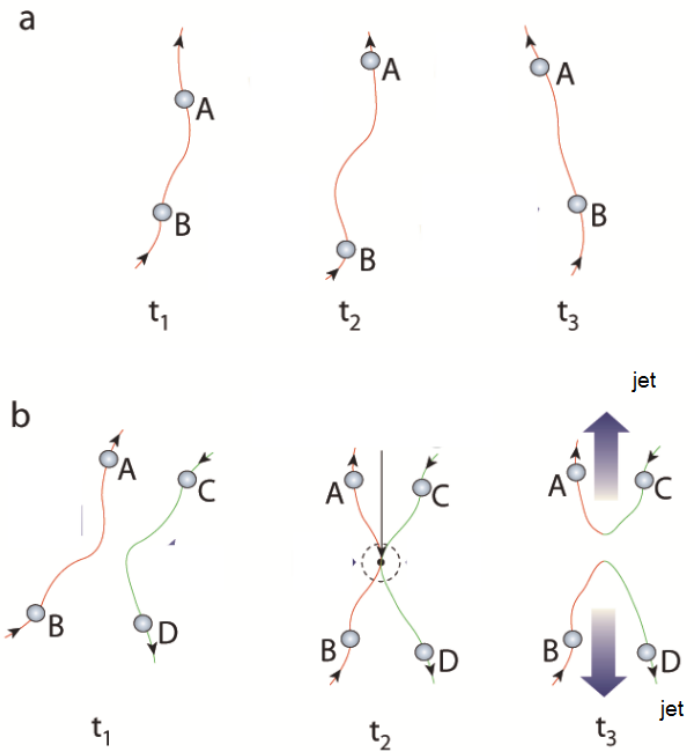

FIGURE 2.2: The basic process of reconnection. Case a: No reconnection; the frozen-in condition is valid and plasma particles are connected at all times to the same field line. Case b: Reconnection; frozen-in condition violated at kinetic scales in a small diffusion region for a collisionless plasma(dashed circle). Plasma particle connected at one time to one field line are later connected to different (reconnected) field line

where the integral is taken within the diffusion region where non-ideal terms exist. However, some research has found this definition a bit too general since it can include borderline phenomena such as magnetic diffusion [116]. The violation of the frozen-in condition and the onset of reconnection eventually lead to magnetic energy being dissipated and transferred to energy of charged particles in the form of local heating, bulk acceleration and non-thermal particle acceleration. The rate at which magnetic reconnection occurs is the rate of change of the magnetic field flux.

A first model attempting to describe the process of reconnection is the Sweet-Parker model which is shown schematically in Figure 2.3. The main feature of this model is that reconnection takes place in a thin diffusion region of width 2δ and length $2L$. The plasma outflow is along the horizontal Z axis. In this configuration, four distinct regions of the plasma are formed. Two inflow and two

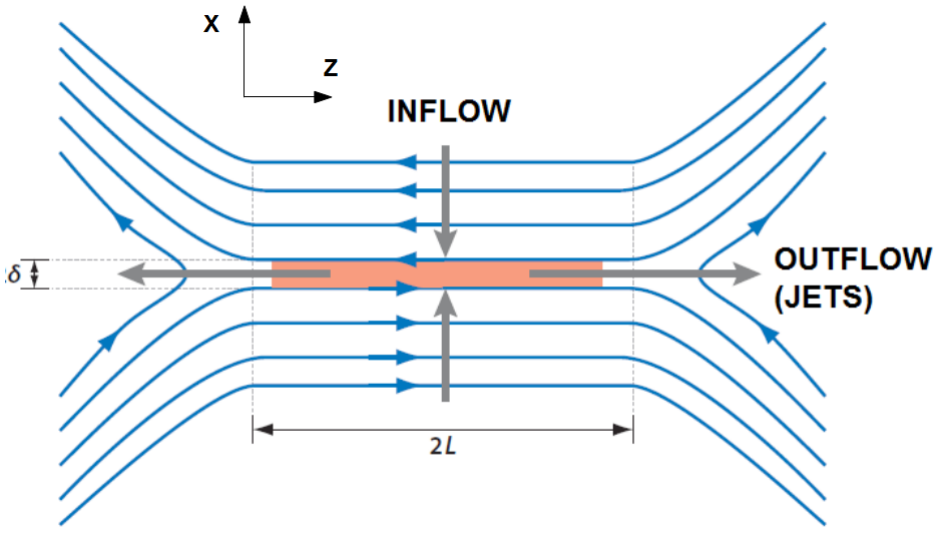

FIGURE 2.3: Sweet-Parker model of magnetic reconnection in the reconnection plane XZ [162] . Reconnection takes place in the red shaded region (diffusion region), where there is a localized resistivity. The reconnecting magnetic field (horizontal axis Z) is antiparallel on either side of the current sheet and vanishes in the center. The normal to the current sheet is along the vertical axis X. The black arrows denote the inflow and outflow of plasma

outflow regions. These regions are separated by four lines, called separatrices, that extend outwards from the edges of the diffusion region. The outflow speed is equal to the Alfvén speed $v_A = B/\sqrt{\pi\rho}$. The dimensionless reconnection rate can be expressed as the ratio between the inflow and the local Alfvén speed. Given all of the above and taking into account the conservation of mass for an incompressible flow, the reconnection rate is:

$$\frac{v_{in}}{v_A} = \frac{\delta}{L} \tag{2.6}$$

In the Sweet-Parker model, this ratio is equal to $S^{-1/2}$, where S is the Lundquist number. The Lundquist number is defined as the ratio of the Alvfén time to the Ohmic diffusion time: $S = \frac{Lv_A}{\eta}$, where η is the magnetic diffusivity. One issue of the Sweet-Parker model is that, since S is very large in most astrophysical systems, the reconnection rate is too slow to account, for instance, for the observations of solar flares. Other models, such as the Petschek model, provide a more accurate description of some aspects of magnetic reconnection such as the reconnection rate. A review of some of these models along with a more detailed presentation of the Sweet-Parker model can be found in [162].

In most astrophysical environments the mean free path of the particles is such that the plasma is essentially collisionless. Therefore a traditional resistive diffusion region such as the one used in the Sweet-Parker model is rather problematic. Accordingly, a successful description of magnetic reconnection in space plasmas must account for both the observed reconnection rates, which are much faster than the rate predicted by the Sweet-Parker model, while considering a collisionless plasma that has no classical resistivity. To meet these conditions we need to take into account kinetic physics in order to study dissipative effects. In this context it is instructive to consider the so-called generalized Ohm's law [7]:

$$\vec{E} = -\vec{v_i} \times \vec{B} + \eta \vec{J} + \frac{1}{ne}(\vec{J} \times \vec{B}) - \frac{1}{ne}\nabla \cdot \vec{\vec{P}}_e - \frac{m_e}{e}\frac{dv_e}{dt} \tag{2.7}$$

The first two terms of the right hand side of the equation are the ones from the classic formulation of the Ohm's law. They dominate at large scales where the MHD description is valid. The third term is known as the Hall term and becomes important at scales comparable to the ion inertial length. At those scales the ions decouple from the magnetic field, while the electrons remain frozen. The decoupling between the ions and the electrons produces a strong current, which, in turn, creates a magnetic field perpendicular to the reconnecting field. This does not break the frozen in condition and satisfy the equation 2.5. The two remaining terms, however, can break the frozen in condition. The fourth term is the gradient of the electron pressure tensor. It comes into play at the same scales as the Hall term but it is usually small compared to the Hall term. The last term is the electron inertia and becomes important at scales comparable to the electron inertial length. At this scale the electrons become unmagnetized as well and break away from the magnetic field. The scaling of those terms gives rise to a geometry more complex than the one provided by the Sweet-Parker model. As illustrated in Figure 2.4, two diffusion regions are created. An outer region where ions are decoupled but electrons remain magnetized and an inner region where electrons are decoupled as well. The outer ion diffusion region has scales compared to the ion gyroradius whereas the inner electron diffusion region is smaller and has scales comparable to the electron gyroradius.

Numerical simulations have studied the characteristics of collisionless reconnection [8, 117, 118], with an array of different numerical models. A comparison of the results regarding the observed reconnection rate is shown in Figure 2.5. A

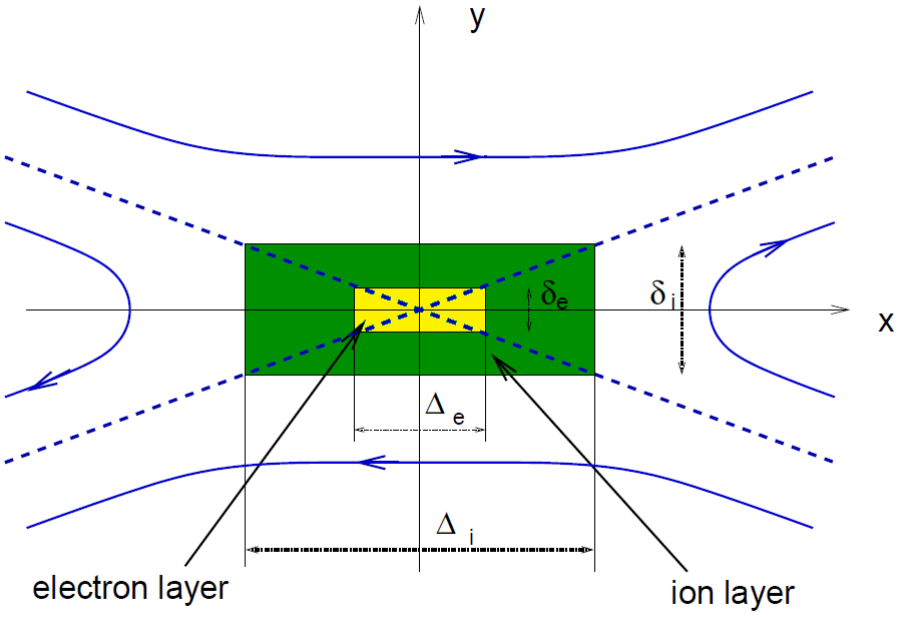

FIGURE 2.4: Model of collisionless reconnection. The ion diffusion region is marked by the green box. The electron diffusion region is marked by a the yellow box. δi and δe are comparable to the ion and electron inertial length respectively.

very important result of such simulation study is that the reconnection rate is not sensitive to the specific process breaking the frozen-in condition and that fast reconnection, that is reconnection with rate ~ 0.1, is obtained as long as the Hall effect is included. Recent kinetic simulations studied in more detail the structure of the ion and electron diffusion region, determining a number of defining characteristics of Hall collisionless reconnection [62, 77]. First, the presence of a quadrupolar out-of-plane magnetic field. Second, a bipolar in-plane electric field. Third, a distinct electron diffusion region separate from the outer ion diffusion region in which the pressure tensor and electron inertia have a promiment role. Finally, the presence of an electron outflow jet. In situ space observations have tested and verified these predictions [99, 113, 133, 140, 145]

A very important aspect of reconnection, in particular in terms of its role as dissipation mechanism, is how energy is partitioned between heating and non-thermal acceleration and between ions and electrons, and how the energy partition depends on the conditions under which reconnection takes place. The Sweet-Parker model predicts that half the energy is going into particle heating and half into bulk acceleration. Kinetic simulations have shown that about half the converted

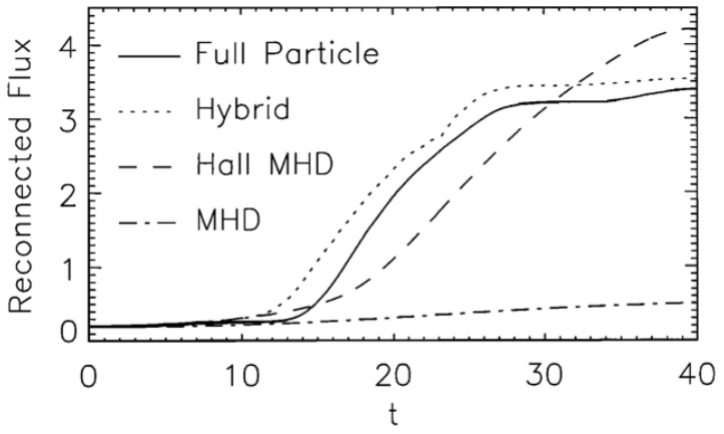

FIGURE 2.5: Numerical simulations of collisionless reconnection. Comparison of the observed reconnection rates for different numerical models [118].

energy goes to electrons in the form of heating and $\sim 25\%$ to ion heating [61]. The rest of the energy goes to bulk acceleration in the form of reconnection jets. Finally, a small percentage of the converted energy contributes to non-thermal high energy particle acceleration. Observations in the Earth's magnetotail [34] have shown evidence consistent with more energy going into ions than predicted by the simulations. Overall, the energy partition is not completely understood yet.

Another important aspect is how exactly the dissipated energy is converted into plasma heating and acceleration and how such energization mechanisms depends on different reconnection configurations such as the guide field, current sheet asymmetries etc. Also this aspect is not fully understood and its the topic of many reconnection studies. One important point is that during reconnection, the heating and acceleration are not exclusively localized in the diffusion region but also take place downstream in the outflow [22, 136] as well as along the separatrices [123]. The main mechanism invoked is the acceleration by the parallel electric field that is present in reconnecting regions (Equation 2.5) [35, 37, 45, 55, 61, 125, 140]. Other mechanisms have also been investigated such as acceleration due to the curvature of the reconnected magnetic field lines [23, 31, 49, 57, 160] and betatron acceleration downstream of the X-line [57, 125]. Another mechanism that has been invoked is wave-particle interactions with a number of wave modes such as whistler waves and Kinetic Alfvén Waves (KAW) [16, 45, 55, 81, 125]. Such interactions take place in the electron diffusion region and along the separatrices. The results so far both from observations and numerical simulations do give many indications but it seems that there does not exist a general consensus yet.

The study of magnetic reconnection in space plasma has yielded significant conclusions regarding many of the issues discussed above and has established its importance for dissipation, plasma heating and particle acceleration [148, 151]. In particular, the availability of high resolution spacecraft measurements in the near-Earth space (Cluster, Themis, MMS) have allowed very detailed in situ studies of the physics of reconnection. Observations of magnetic reconnection at the Earth's magnetopause [112, 114] and magnetotail [4, 103] have demonstrated that it is an effective process for heating and particle acceleration. In addition, reconnection has also been observed in structures that form and propagate in the solar wind [20, 44, 47, 48, 73, 97, 105, 127, 128, 135, 161].

2.2 Turbulence

The flow of a fluid can be of two different natures, laminar or turbulent. A flow is said to be laminar when the fluid flows smoothly in parallel layers with little disruption. There are no eddies or swirls and the particles of the fluid move orderly, following closely the general flow of the fluid. In contrast, a turbulent flow is irregular and generally unpredictable (some of its statistical properties may however be predicted). It is characterized by the formation of eddies of different sizes. The fluid particles follow a highly non-linear motion and the fluid flow becomes chaotic. The transition of a fluid flow from laminar to turbulent can empirically be determined with the help of the Reynolds number, defined as the ratio between the inertial and the viscous forces in the Navier-Stokes equation governing the dynamics of incompressible flows:

$$R_e = \frac{\rho v L}{\mu} = \frac{v L}{\nu} \tag{2.8}$$

Where ρ is the density of the fluid, v is the characteristic velocity, L is the characteristic length scale, μ is the dynamic viscosity of the fluid and ν is the kinematic viscosity of the fluid($\nu = \mu/\rho$). In a magnetized plasmas, a magnetic Reynolds number R_{eM} can additionally be defined in a similar way by substituting the dynamic viscosity μ for the magnetic diffusivity η:

$$R_{eM} = \frac{v L}{\eta} \tag{2.9}$$

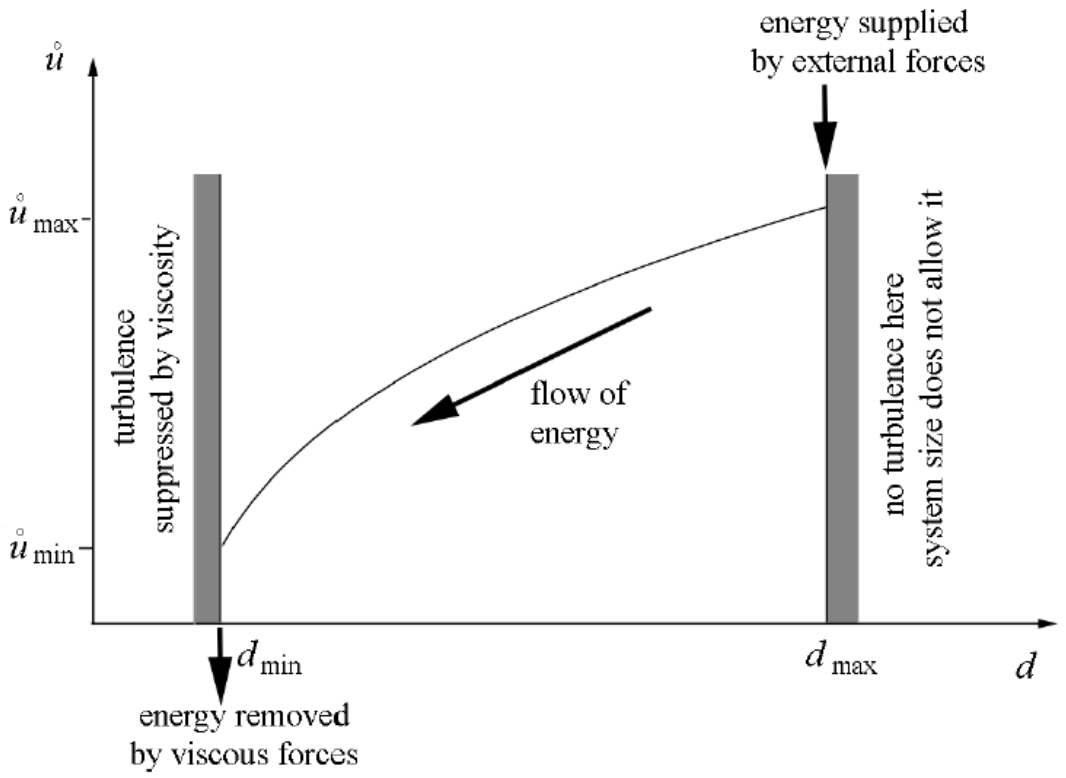

FIGURE 2.6: The turbulent energy cascade. Energy is injected at d_{max} and cascades down to d_{min}, where it dissipates. Adapted from Environmental Fluid Mechanics by Benoit Cushman-Roisin.

In hydrodynamics, a high Reynolds number ($R_e > 10^3 - 10^5$) leads to turbulent flow. In collisionless space plasmas, where no classical viscous effects exist, the Reynolds number goes to infinity. However, effective Reynolds numbers can be estimated. In the solar wind at $1AU$ it is found that values as high $R_{eMeff} \sim 10^{16} - 10^{17}$ can be reached [95]

The phenomenology of energy cascade in turbulence was introduced by Richardson in 1929. According to this idea, large scale eddies are initially formed by the large scale motion of the fluid. These eddies interact (or collide) with each other and break up forming smaller ones which in turn break up. That process goes on until very small scales are reached, where velocity shear becomes stronger and the viscous effects become more important. At the smallest scales, eddies eventually are dissipated due to viscous effects, leading to fluid heating (Figure 2.6). The scale range where the nonlinear effects (i.e., the cascade) dominates over dissipation is called the *inertial range*, while the region where dissipation dominates is called the *dissipation range*. In hydrodynamic and MHD turbulence, the power spectral density (PSD) of the turbulent fluctuations follow the so-called

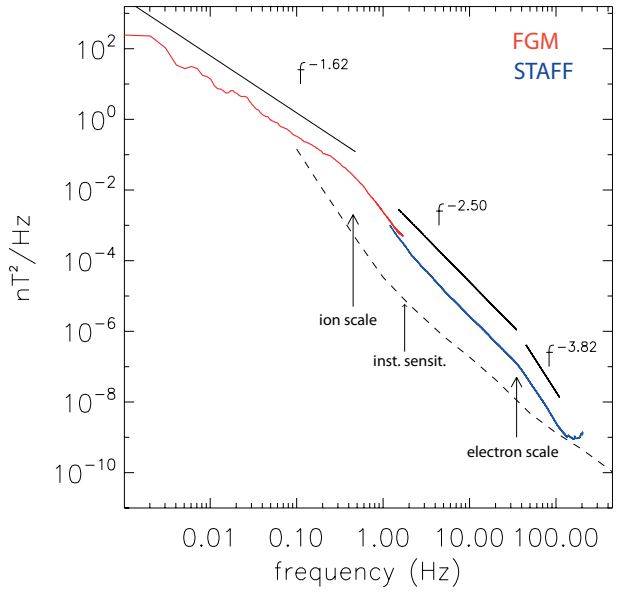

FIGURE 2.7: Magnetic field energy spectra, measured by the Cluster spacecraft in the solar wind. The transition from the inertial to the dissipation range happens around $1Hz$. The slope of the magnetic field spectrum becomes steeper above that frequency. The red and blue lines are measurements from the FGM and STAFF instruments (see Chapter 3.2). The dashed black line denotes the instrument sensitivity level. From [129].

Kolmogorov scaling $E(k) \sim k^{-5/3}$ in the inertial range. This spectrum can be obtained by simple dimensional analysis. However, Kolmogorov [68] provided the first exact derivation of the third order moment of the velocity increments, from which the second order moment (i.e., the power spectrum) can be inferred, under several assumptions (e.g. self-similarity, isotropy and homogeneity of the turbulent fluctuations). Note that in MHD turbulence, there is another competing theory introduced independently by Iroshnikov and Kraichnan that predicts a slightly different spectrum, $E(k) \sim k^{-3/2}$ [59, 71].

In situ observations in near-Earth space have enabled significant progress to be made in the understanding of turbulence in magnetized plasmas [9, 67]. In the solar wind, energy spectra at MHD scales (i.e. the inertial range) show an ubiquitous scaling close to the Kolmogorov spectrum. That inertial range is thought to form because of the nonlinear interactions between counter-propagating Alfvén wave packets that may originate near the Sun. In planetary magnetosheaths, a similar spectrum has been reported in a few case studies [1, 141]. However, recent large statistical surveys in the magnetosheath of Saturn [52] and Earth [58] showed that the $-5/3$ inertial range is not ubiquitous, and a spectrum close to f^{-1} seems to be the dominant feature at MHD scales.

In recent years, the interest of the turbulence community has shifted toward the kinetic scales. An example of the measured turbulent spectra in the solar wind that spans over five decades of scales (from the MHD down to the electron scale) is given in Figure 2.7. Because the near-Earth space plasmas are collisionless (or weakly collisional), classical resistivity cannot account for dissipation of the turbulent fluctuations. Therefore, kinetic effects should effectively dissipate the electromagnetic fluctuations at small scales. A classical signature of that dissipation is the steepening of the magnetic energy spectra observed near the ion and electron gyro-scales (or inertial lengths). However, the exact processes that are responsible for that dissipation are still hotly debated. Indeed, a variety of dissipation mechanisms operate at kinetic scales. These include resonant or non-resonant wave-particle interactions such as Landau and cyclotron resonances or stochastic heating. The proper identification of any of these mechanisms requires the knowledge of the nature of the turbulence at kinetic scales. Two main candidates are generally debated, the Kinetic Alfvén Wave (KAW) and the whistler turbulence. To those modes one can add other electrostatic modes that may dominate the turbulence at electron or sub-electron scales, such as the lower hybrid and the Langmuir modes. To make the picture even more complex, one should add the generation of a variety of coherent structures as the turbulent cascade proceeds to smaller scales because of the increase of the strength of non-linearities in the system. These structures include magnetic islands, solitons, shocklets and vortices. These structures are generally associated with current sheets that may be sites magnetic reconnection, where significant localized dissipation occurs. This underlines the strong relationship between turbulence and magnetic reconnection in magnetized plasmas, as discussed in the next section.

2.3 Magnetic Reconnection in Turbulence

Magnetic reconnection in turbulent plasmas takes place in small-scale current sheets that form spontaneously in the turbulence [90, 91, 134, 135]. An illustration of turbulent reconnection can be seen in Figure 2.9, that shows the results of numerical simulations. In this figure we observe a large number of thin current sheets forming in the turbulence. A subset of those current sheets are sites of ongoing magnetic reconnection. Such reconnection has been observed for the first time in the terrestrial magnetosheath downstream of the quasi-parallel shock [124]

as shown in Figure 2.8, and later also in the solar wind [20, 44]. Although it has been evoked in other astrophysical environments such as solar flares to account for the observed energetic particles [76, 153], observational evidence remains relatively scarce due to the limited availability of in situ data. Recent statistical observations [105] have indicated a link between the structures formed in the turbulence and reconnection regions although measurements could not specifically address kinetic scales due to limitations in the resolution of plasma measurements. These observations strongly support magnetic reconnection as a major mechanism of energy dissipation in turbulent plasma at kinetic scales, as indicated by [141]. However, how significant is the contribution of magnetic reconnection as a dissipation mechanism at kinetic scales remains largely an open question.

Turbulent reconnection can have different characteristics from that occurring in laminar boundaries such as the magnetopause and the magnetotail. One important aspect is related to the reconnection rate, specifically if turbulent reconnection can occur with similar rates as laminar reconnection (rate $\sim 10\%$) or even with faster rates. A number of studies have investigated the properties of turbulent reconnection in theory and numerical simulations [69, 74, 80, 90, 134] and discussed this aspect. These studies have demonstrated that turbulent reconnection has a much weaker dependence to the Lundquist number compared to the predictions of the Sweet-Parker model and therefore can be fast. Figure 2.10 shows a cartoon of turbulent reconnection, where the introduction of small-scale magnetic field fluctuations in the inflow region can make reconnection faster by locally reducing the elongation of the diffusion region, that is otherwise much larger than its thickness in the Sweet-Parker model. The fact that turbulent reconnection is fast has been verified by in-situ observations during which a rate of $\sim 10\%$ was measured [124]. Recent simulations [134] also suggest that turbulence can significantly enhance the reconnection rate beyond the typical value of $\sim 10\%$ typical of Hall reconnection, but such expectations has not yet been experimentally verified.

Another very important aspect of turbulent reconnection is the capability to efficiently heat and accelerate particles to high energies at kinetic scales. This aspect has very important potential implications for energization in many astrophysical plasmas, such as the solar corona, the solar wind and more distant objects such as accretion disks and supernovae remnants. Many recent results from numerical simulations have suggested that reconnection occurring in small-scale current sheets forming in turbulence can efficiently energize plasma [13, 53, 54, 61, 89, 160].

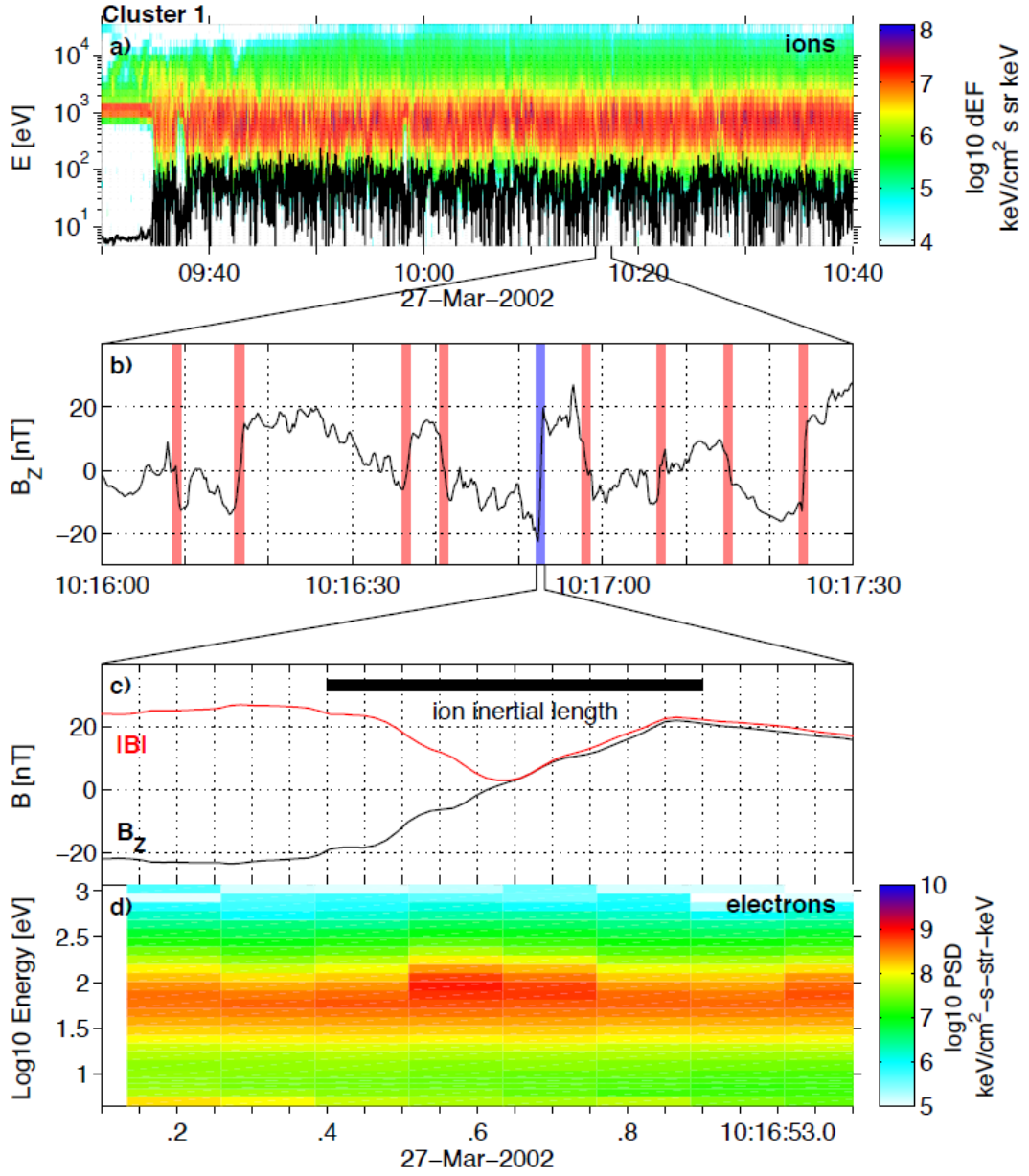

FIGURE 2.8: Reconnecting current sheet in the Earth's Magnetosheath observed by the Cluster spacecraft. From [124].

However, no detailed in situ observations of the specific mechanisms that drive this heating inside small-scale reconnection sites in turbulence are available.

Figure 2.11 shows that electron heating occurs at kinetic scales in small scale reconnecting current sheets forming in the turbulence. Such expectation has been verified for one case by [124], as shown in the bottom panel of Figure 2.8. A more recent study performed in this thesis has further shown on a statistical basis that thin current sheets in turbulence are sites of major electron heating at kinetic scales [17], although the exact heating mechanisms have not yet been identified.

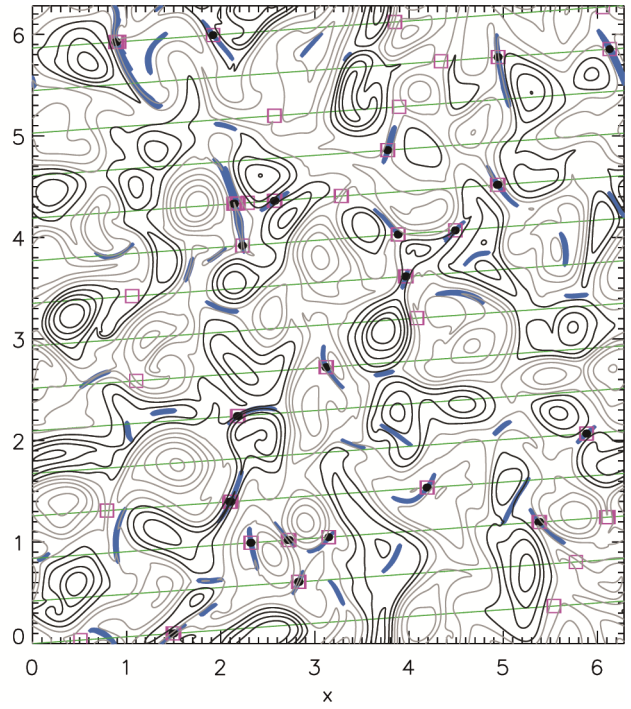

FIGURE 2.9: Numerical simulation of reconnection in turbulence. The black lines are the contours of the magnetic field, the blue shaded regions are the current sheets, the black dots are the regions where reconnection is ongoing. From [135].

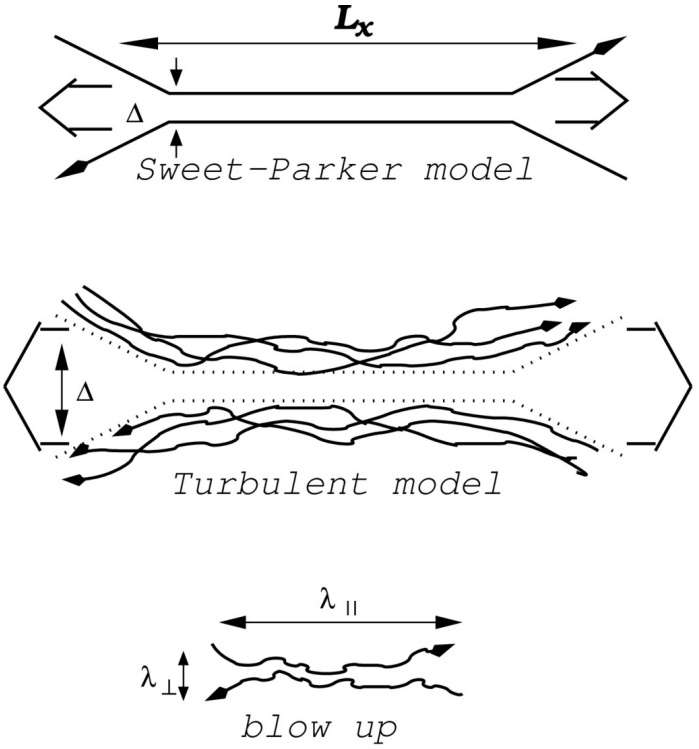

FIGURE 2.10: Theoretical model on the effects of turbulence on a reconnecting current sheet. From [74].

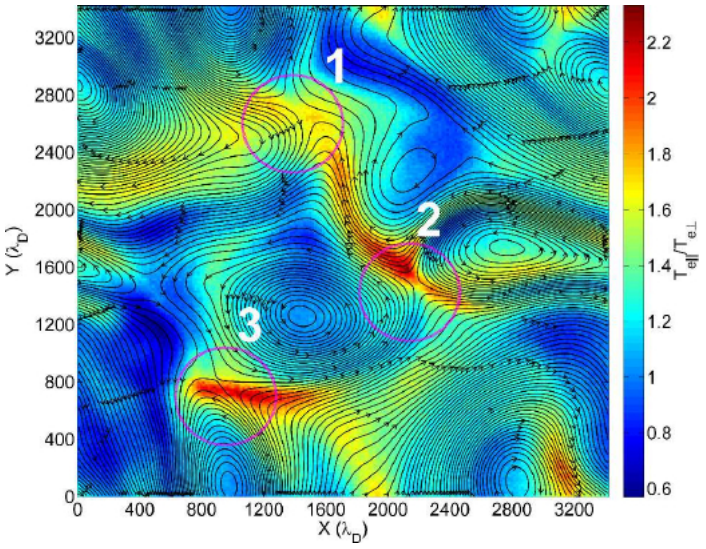

FIGURE 2.11: PIC simulations of turbulent reconnection by [53]. Electron heating was observed in thin reconnecting current sheets that formed in the turbulence.

Similar expectations hold for the acceleration to energies higher than thermal energies. Figure 2.12 shows the acceleration of electrons to suprathermal energies (up to $\sim$ several times larger than the thermal energy) in thin current sheets forming within shear-flow turbulence. The simulation shows that the energization is highly non-uniform and patchy. Other simulation studies have shown how particles can be accelerated to very high energies (up to many times larger than the thermal energy) by interacting multiple times with thin current sheets and magnetic islands [31, 54, 89]. Such expectations have not yet been verified through in situ measurements, although turbulent reconnection is often invoked as an energetic particle acceleration mechanism in distant astrophysical objects [89].

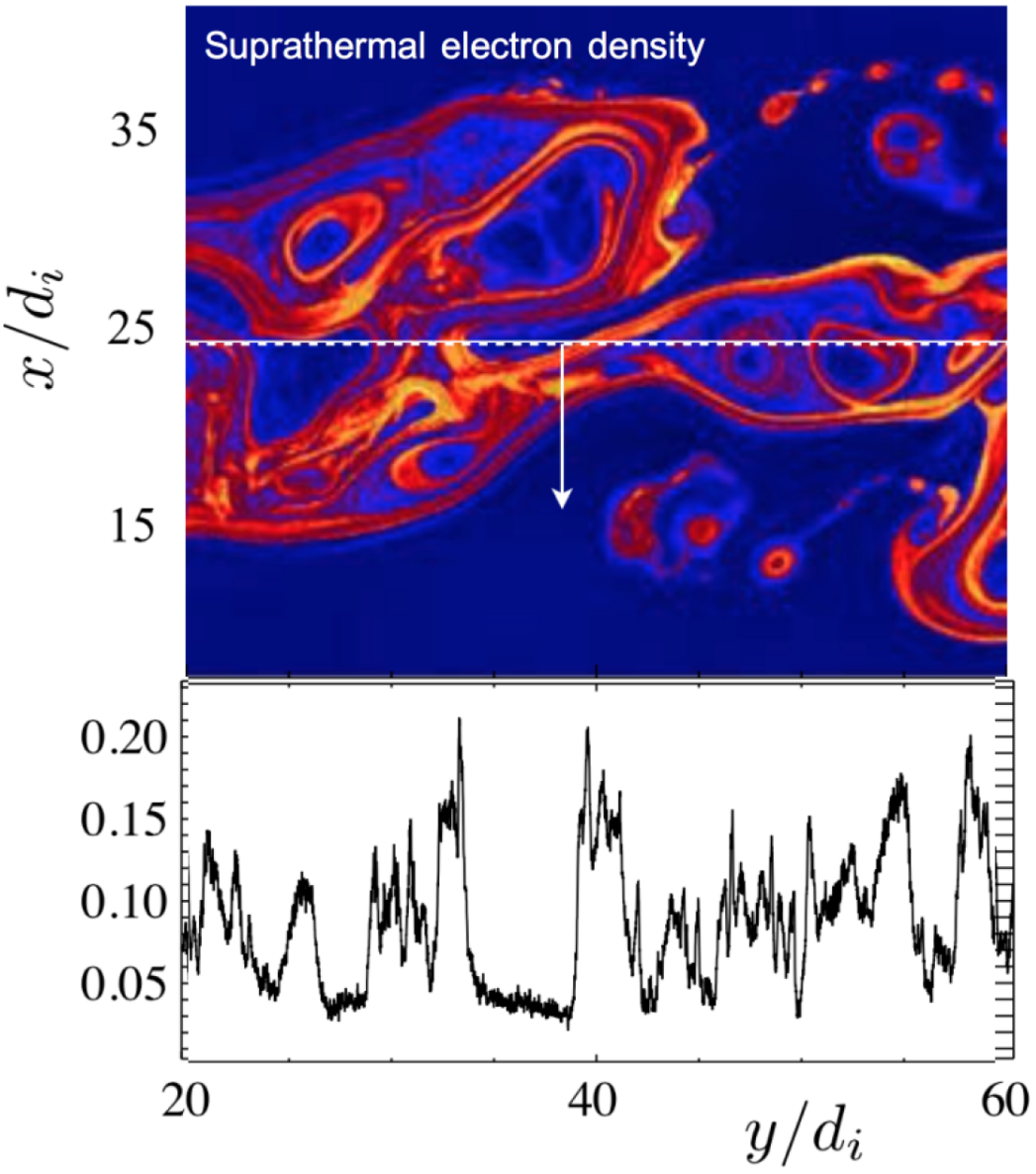

FIGURE 2.12: The top panel shows a two-dimensional particle-in-cell simulation of shear-flow turbulence by [61]. The color denotes the density of suprathermal electrons. The bottom panel is a horizontal cut along the dashed line showing the density of suprathermal electrons. Electron acceleration is observed in small-scale structures.

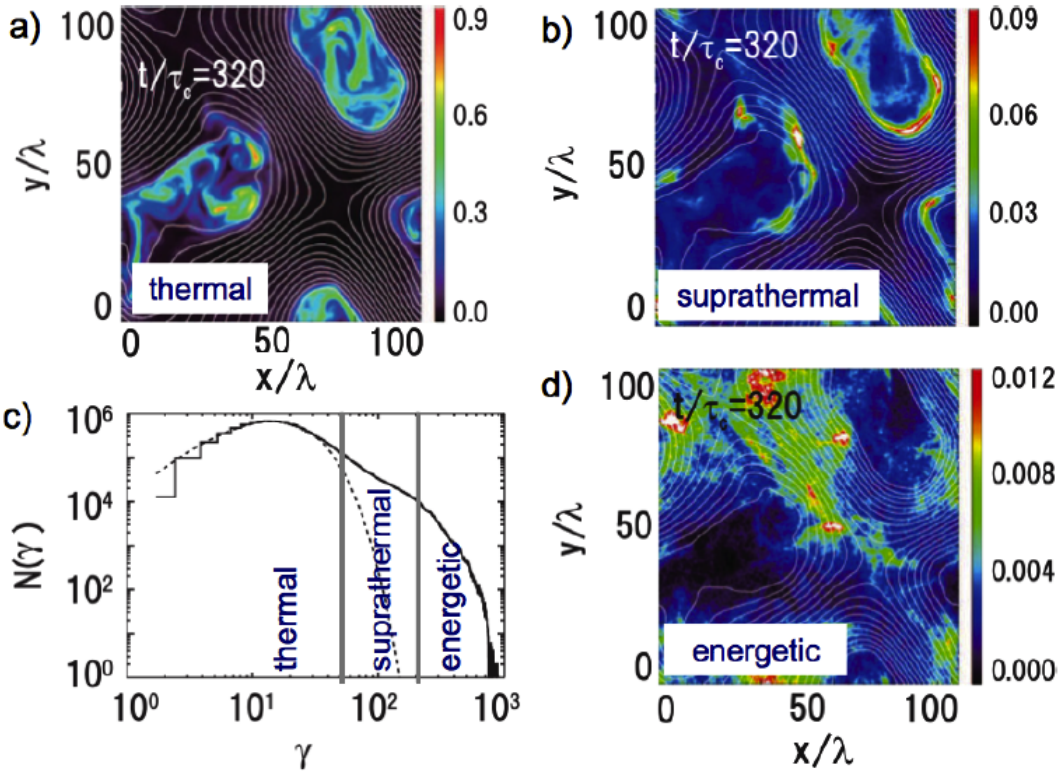

FIGURE 2.13: Numerical simulations of particle heating and acceleration during magnetic reconnection [54]. Plasma heating and acceleration occurs at different regions and is highly localized.

Chapter 3

Instruments and Data Products

This work focuses on the analysis of *in situ* data in turbulent space plasma. The bulk of this work used data from the Cluster mission. In this chapter, the basic principles, operating modes and data products of the instruments used for the results of this study are detailed.

3.1 Cluster Mission Overview

Cluster is a mission of the European Space Agency which was launched in 2000. Its objective is to study the magnetic environment in near-Earth space. The scientific payload consists of 11 instruments which are focused on *in situ* plasma observations. Those instruments measure the properties of the electric and magnetic fields, ion and electron velocity distribution functions [38]. The mission consists of four identical spacecraft flying in a tetrahedral formation, in a highly elliptical orbit. The distance between the spacecraft is varying during the mission from $10.000km$ to $100km$. The combination of the measurements of the four spacecraft allowed for the first time the application of multi-spacecraft methods in the study the physics of involve complex 3-dimensional processes at the scales of the separation of the spacecraft. Specifically, these methods allow us to differentiate between spatial and temporal variations, to estimate quantities such as $\vec{J} = \nabla \times \bar{B}$ and their structure [43]. At pre-defined intervals the spacecraft operate in Burst Mode. In Burst Mode high resolution data from all instruments is gathered and transmitted to Earth. The Burst Mode has a typical duration of 3 hours and is usually triggered around areas of scientific interest such as the magnetopause and

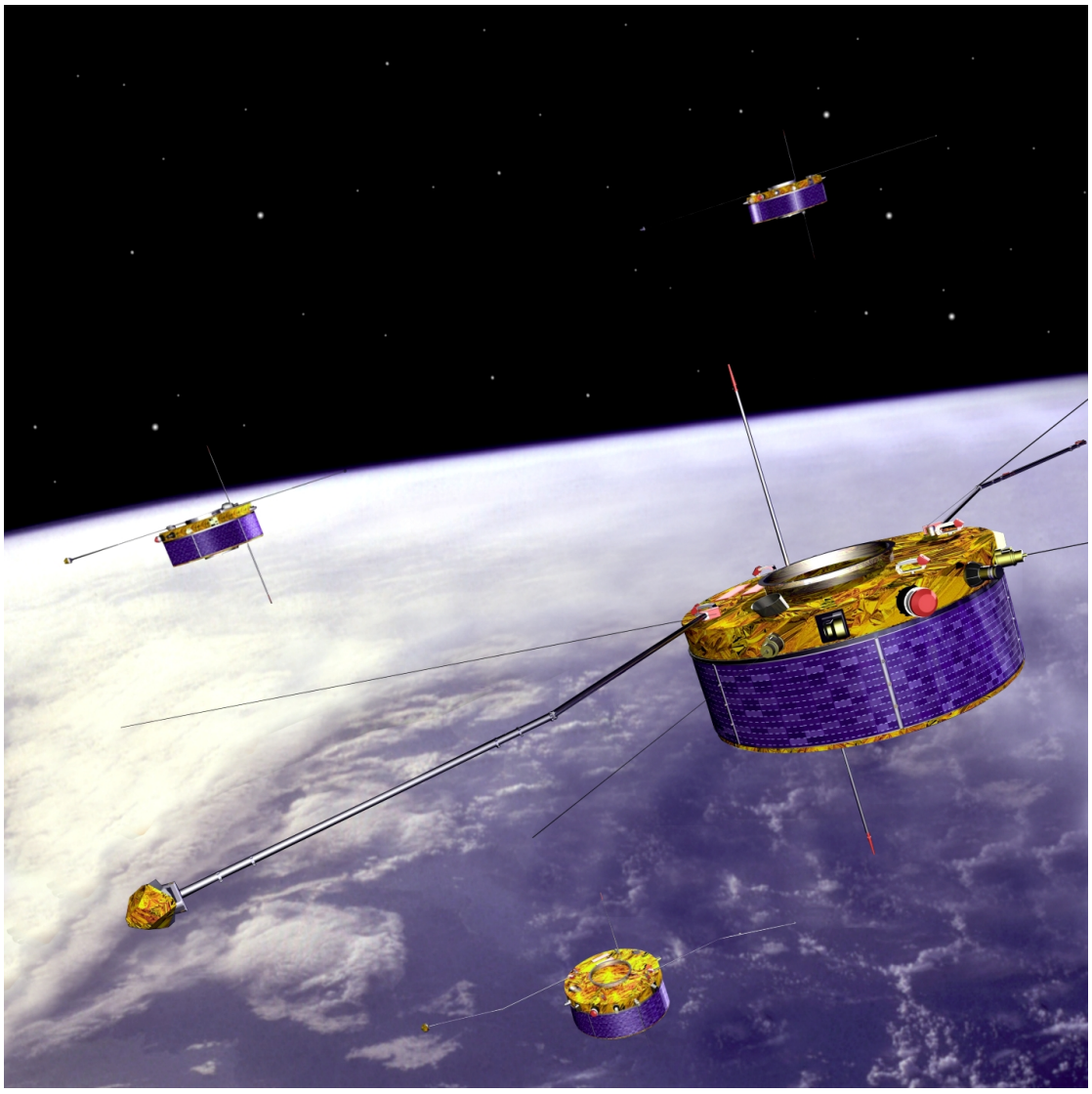

FIGURE 3.1: Cluster mission. Rendering of the 4 spacecraft. Courtesy of ESA.

the magnetotail. The spacecraft are spinning with a period of $4s$, in the equatorial plane and tilted a few degrees ($\sim 2^o - 7^o$) in order for the probes of the EFW instrument to be sunlit at all times. The data is measured in the spacecraft reference frame (ISR2). The reference frame commonly used is GSE, with most data products provided in that format. A schematic of the spacecraft and the positions of the different instruments are shown in Figures 3.2 and 3.3.

3.2 Magnetic Field Measurements

The magnetic field is measured by two instruments on board Cluster, a flux-gate magnetometer (FGM) (Figure 3.4) and a search-coil magnetometer (STAFF)(Figure

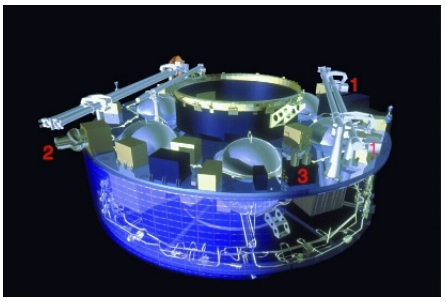

FIGURE 3.2: Cutaway of Cluster spacecraft main equipment platform, showing the FGM (1), EDI (2) and ASPOC (3) instruments. Courtesy of ESA.

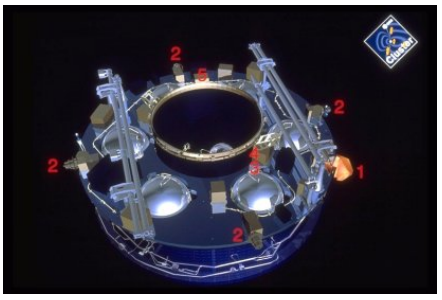

FIGURE 3.3: Cutaway of Cluster spacecraft main equipment platform, showing the STAFF (1), EFW (2), DWP (3), WHISPER (4) and WBD (5) instruments.

3.5). FGM focuses on DC field measurements while STAFF measures fluctuations of the magnetic field.

3.2.1 Flux-gate magnetometer

A flux-gate magnetometer consists of two coils wrapped around a ferromagnetic core. Alternating current is applied to the primary coil creating an induced current in the secondary coil. If there is no external magnetic field the current induced in the secondary coil will be the same as the current applied in the primary coil. An external magnetic field will create an offset between two currents which yield a measurement of the magnetic field.

The FGM instrument on board Cluster consists of two tri-axial sensors measuring the three components of the magnetic field [51]. One sensor is placed at the end of a 5.2 meter boom while the other is placed on the same boom 1.5 meter away from the spacecraft body, in order to control the magnetic interference from the spacecraft. The flux-gate sensors are nominally sensitive in the range $0Hz$ to $10Hz$, although in practice the instrument noise level is such that the sensitivity

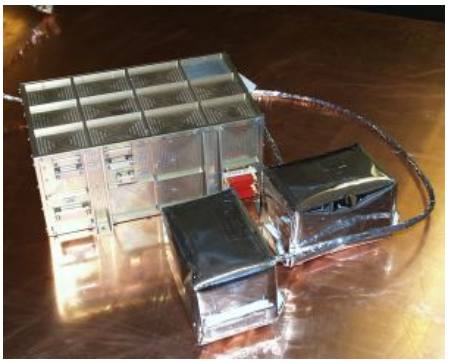

FIGURE 3.4: FGM instrument. Courtesy of Imperial College.

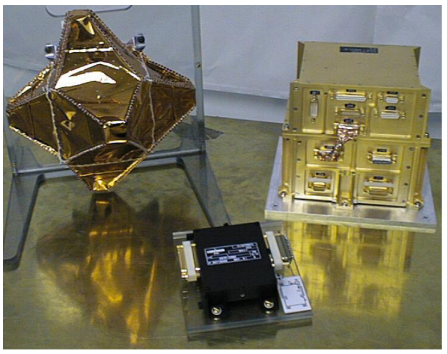

FIGURE 3.5: STAFF instrument. Courtesy of LPP.

degrades significantly above $1Hz$. For the DC field the accuracy of the instrument is $\sim 0.1nT$. The sampling rate in Burst Mode operation is $67Hz$.

3.2.2 Search-coil magnetometer

STAFF consists of a magnetic waveform unit (STAFF-SC) and a spectrum analyzer (STAFF-SA). The first measures fluctuations of the magnetic field from $0.1Hz$ up to $4kHz$ while the second computes spectra of the magnetic and electric field from $8Hz$ up to $4kHz$. It consists of a coil wrapped around a ferromagnetic core. In the presence of a varying external magnetic field, the variation of the magnetic flux induced by the field is proportional to the voltage induced in the coil. The STAFF instrument has a tri-axial search-coil sensor operating at frequencies between $0.1Hz$ and $4kHz$. Given the transfer function of the instrument noise, the measurements are less sensitive than FGM below $1Hz$. STAFF-SC provides waveforms of the 3 components of the magnetic field with a sampling frequency of up to $450Hz$ in Burst Mode. STAFF-SA provides spectral matrices and power spectral densities for each of the 3 components of the magnetic field (B_x, B_y, B_z) and for two components of the electric field (E_x, E_y) at different time resolutions

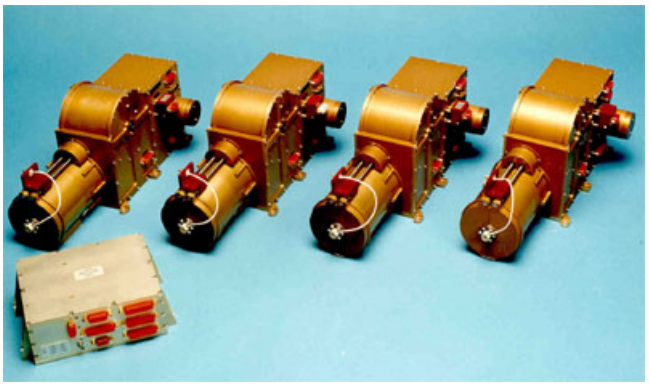

FIGURE 3.6: EFW instrument. Courtesy of IRF.

for frequencies from $8Hz$up to $4kHz$. Those quantities are calculated on board using measurements by the magnetic field sensors (STAFF) and electric field probes (EFW). In Burst mode, spectral matrices are provided in the frequency range of $64Hz$ to $4kHz$ with $1s$ resolution, while the power spectral densities are provided for the same frequency range but at higher time resolution ($0.125s$ or $0.25s$).

3.3 Electric Field Measurements

The electric field is measured by the EFW instrument [50] using four spherical probes located at the end of thin wire booms extending outwards from the spacecraft in the spacecraft spin plane and phased by 90^o in that plane [110]. Two probes in each pair are kept at a distance of about $88m$ from each other by the rotation of the spacecraft around its axis. The requirement for a relatively long distance between the probes and the spacecraft comes from the necessity to overcome the effects of the Debye shielding as well as the photoelectron cloud around the spacecraft. Additionally, the larger distance between the probes results in a larger potential difference, which is easier to measure. The potential difference between two opposed probes yields a measurement of the electric field in the direction along the axis defined by the two probes (Figure 3.7). The use of the 4 probes allows an estimation of two orthogonal components of the electric field in the plane of the spacecraft spin. There is no antenna to measure the component of the electric field along the spin axis, that can only be estimated from the two components measured in the plane. Such third component is deduced by using the assumption $\vec{E} \cdot \vec{B} = 0$. This assumption leads to significant errors when the angle between the magnetic and the electric field is small and cannot be used at

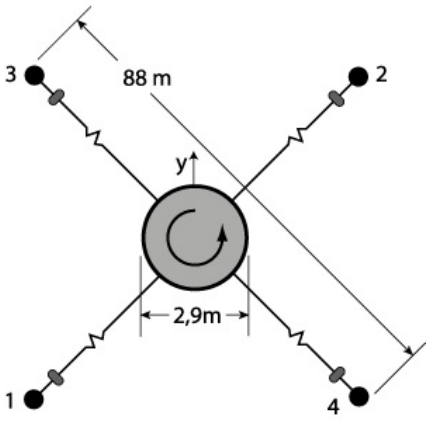

FIGURE 3.7: Schematic of the Langmuir probes of the EFW instrument configuration. Courtesy of IRF.

all when they are aligned since it degenerates. In the case of EFW the third component is usually not calculated if the angle between the magnetic and the electric field is below 15^o. More recent missions such as MMS are equipped with a rigid antenna and directly measure the component of the electric field along the spin axis. For Cluster, the probe to probe potential and the subsequent electric field measurement are given at a sampling rate of up to $450Hz$ in when operating in Burst Mode.

3.4 Spacecraft Potential

The spacecraft and the probes are conductive bodies in a plasma. There are two effects that lead to electric charge. Photons from the Sun cause photo-electron emission by the spacecraft. That leaves the spacecraft positively charged, which in turns attracts some of the photo-electrons back to the spacecraft. On the other hand, the spacecraft is a conducting body in a plasma. Ions and electrons impact the spacecraft. The electrons are faster and impact at a much greater rate leading to the spacecraft being negatively charged. That in turn attracts some of the ions and repels some electrons, reaching an equilibrium when the charge is such that the ion and electron currents are balanced. Both of these effects are in action, leading to an equilibrium state where the photo-electron current plus the plasma ion current are equal to the plasma electron current. These currents depend on the plasma density and therefore the value of the potential of the spacecraft can act as a proxy of the density [108, 109]. In tenuous plasma such as the magnetosheath

and the solar wind, the photo-electron current completely dominates. That leads to relatively high potential ($> 10V$). Additionally, the spacecraft potential has large variations for small fluctuations of the currents. In order to mitigate that effect an additional current is drawn by the instrument. This bias current adjusts the spacecraft potential to an operating point to a small positive value. This offers the advantage of a relatively steady spacecraft potential, since for such values the potential is significantly less sensitive to fluctuations the photo-electron current.

One important feature of the potential around the spacecraft, is that its structure is not completely isotropic. The main anisotropy is due to the differences between the sun-lit and dark side of the spacecraft. Although the spacecraft surface is conductive, small changes in conductivity of different components and asymmetric structures such as booms introduce perturbations in the structure of the potential around the spacecraft. Additionally, the rotation of the spacecraft introduces a time variation to this effect as different components come in and out of sunlight. This effect becomes noticeable at sub-spin resolution and can influence the measurements of the potential and electron distributions at low energies, as discussed in the next section.

The Cluster spacecraft is equipped with a potential control system. This role is performed by Active Spacecraft Potential Control instrument (ASPOC). It consists of an ion cannon. It functions by heating up and ionizing indium atoms, which are then emitted away from the spacecraft. This allows to lower the spacecraft potential to tolerable values. However, the indium source is limited and therefore ASPOC is not always operational. It must be also noted that its consumption increases the closer the spacecraft potential comes to zero. Its operation is determined by a trade off between a sufficiently low spacecraft potential that does not interfere with low energy measurements on the one hand and on the other hand the consumption rate of the available ion source.

The value of the spacecraft potential on Cluster is deduced from the probe-to-spacecraft potential measured by EFW at a sampling rate of $5Hz$ [110]. Although the probes are at a distance of $44m$ from the spacecraft they are at the edge but inside the potential created by the spacecraft. It is estimated that the probe to spacecraft potential measured by EFW is 80% of the spacecraft to space potential. A correction is made to account for that offset. As mentioned above, the value of the spacecraft potential depends on the density of the ambient plasma around

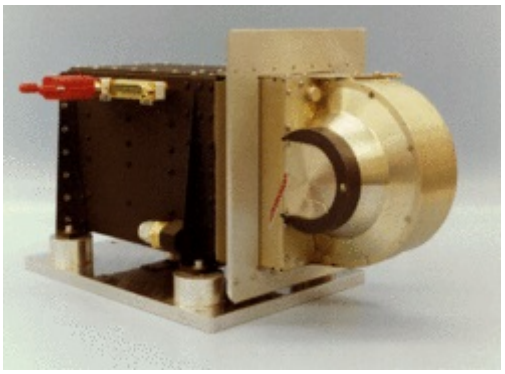

FIGURE 3.8: PEACE HEEA sensor. Courtesy of MSSL.

the spacecraft and therefore it can also serve as a proxy for the plasma density at high time resolution [108, 109].

3.5 Electron Measurements

The two instruments aboard Cluster that measure the properties of the electrons are PEACE and RAPID. PEACE consists of two top-hat electrostatic analyzers (shown in figure 3.8) that measure 3-dimensional electron distribution functions at energies up to $30keV$. RAPID uses pin-hole detectors to measure high energy electrons in the range from $39keV$ to $406keV$.

As illustrated in figure 3.9, the electrostatic analyzers used by PEACE operate by applying a specific voltage between two plates that are shaped as part of a circle. Electrons that enter with energy corresponding to that voltage follow the path down to the detector, whereas electrons with different energies collide with the walls of the detector and are absorbed. Therefore using different values of the voltage, the distribution function is sampled.

The PEACE instrument has two sensors, designated HEEA and LEEA. Both are top hat electrostatic analyzers but have different geometric factors. This means that they are optimized for different ranges of electron fluxes and energies making them suitable for different environments. LEEA is the Low Energy Electron Analyzer and its geometric factor makes it appropriate for higher fluxes and relatively low energies, such as those found in the magnetosheath and the solar wind. HEEA (High Energy Electron Analyzer) is more suitable for environments where the electrons have lower density and higher energy such as those found the outer

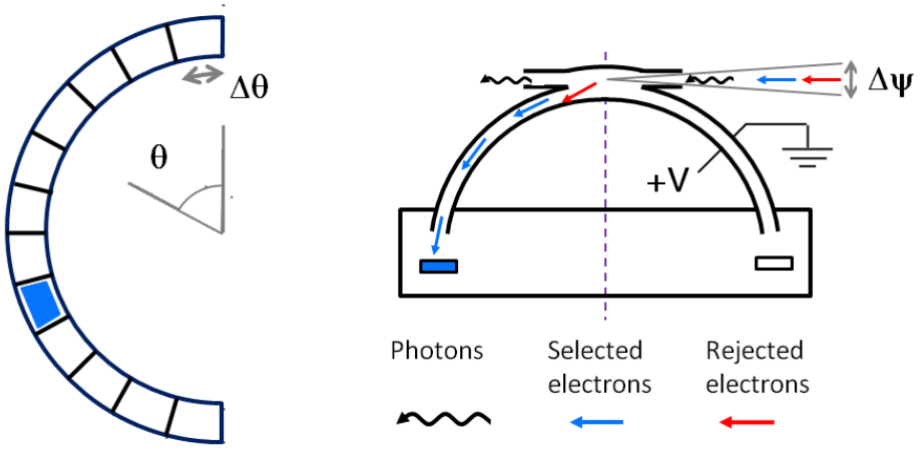

FIGURE 3.9: Illustration of top-hat electrostatic analyser. In the case of PEACE there is simultaneous coverage of a 180^o in elevation angle in 12 equal parts. Adapted from [39].

magnetosphere and the magnetotail. The two PEACE sensors are placed on opposite sides of the spacecraft.

3.5.1 Instrument Operation

Each of the two top hat analyzers has 12 anodes covering 15^o each in the polar direction, so that a combined field of view of 180^o is provided. As illustrated in figure 3.10. They are placed perpendicular to the spacecraft body allowing a coverage of all 180^o elevation angles with respect to the spin axis of the spacecraft. For each measurement, a sweep through the appropriate energy channels is done simultaneously for all the anodes. Hence, as the spacecraft rotates, different azimuthal directions are scanned. Each different measurement scans a part of the sky with a 180^o field of view in elevation and a slice of a few degrees in the azimuthal direction. Every $4s$ the spacecraft completes a full spin and both sensors are able to complete a scan of the whole sky. The resolution of this scan in terms of azimuth angle and energy channels depends on the mode of the instrument. Higher angular resolution comes at the expense of reduced energy resolution, given that each anode has a defined geometry and requires a sufficient accumulation time to complete a meaningful measurement.

There are three modes of operation of the instrument in terms of angular resolution, scanning over a different number of energy channels: LAR ($250ms$ sweep

time) , MAR ($125ms$ sweep time) and HAR ($62.5ms$ sweep time), which stand for Low, Medium and High angular resolution respectively. So, in MAR mode for example the energy sweep lasts $125ms$, performing 32 sweeps per spin, with each spin covering 11.25^o in azimuth and 180^o in elevation. The sensors have a nominal energy range from $0.6eV$ to $26,460eV$, which is divided into 88 channels spaced linearly up to $9.5eV$ and logarithmically above that value. The sensor sweeps through these energy channels from high energies to low energies. The number of energy channels covered by each sweep depends on the instrument mode. The accumulation time for each energy channel is equal. For the three modes of operation, LAR, MAR and HAR, the number of energy bins is 60, 30 and 15 respectively. That yields the different time it takes for a full sweep in each mode. The time it takes for the voltage to be reset for the next sweep ("fly-back time") varies according to the mode. The data collected during the fly-back time is discarded and the corresponding bins are empty in the final data product. The final measurement has 64 energy bins for the LAR mode (with 4 being empty corresponding to the fly-back time), 32 for the MAR (with 2 for the fly-back time) and 16 for the HAR mode (with 1 for the fly-back). There are always 12 polar angle bins. The number of the azimuth angle slices varies also with respect to how many energy sweeps the sensor has the time to do in each spin. Hence, in LAR mode there are 16 azimuth bins, 32 in MAR and 64 in HAR mode. With this configuration the sensor returns always 11,520 values per spin. This is the basic data product with the best resolution available. However, it must be noted that both energy and angular resolution at the final data products vary to conform with telemetry limitations.

3.5.2 Data Products

While the sensor operates most of the time in MAR mode, the resolution of the data transmitted to Earth depends on the available telemetry. The most commonly available data product is the moments of the electron distribution function, namely the density, the velocity and the temperature at the spin resolution of $4s$, calculated on board or on the ground. The other spin-resolution products are the $PITCH\_SPIN$ and PAD. They provide two measurements per spin at the two moments during the spin where the field of view of the sensor is aligned with the direction of magnetic field vector. That offers full pitch angle coverage provided that the magnetic field is relatively stable during the time interval of the spin.

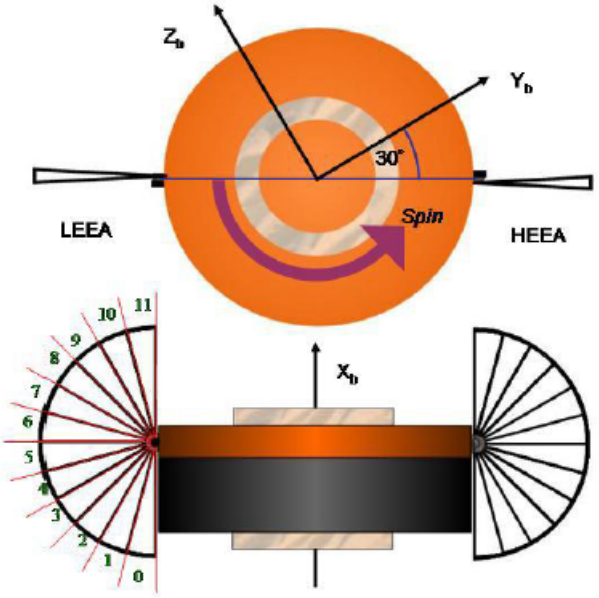

FIGURE 3.10: Schematic of Cluster spacecraft. Placement of the HEEA and LEEA sensors of the PEACE instrument. The field of view of each sensor is a fan arranged looking radially out from the spacecraft body. Courtesy of MSSL.

There are a number of sub-spin data products which provide some of the information of the individual measurements at different azimuth angles which make up the final distribution from which the moments are calculated. The data products $PITCH\_FULL$,$PITCH\_3D$ and $3DR$ offer resolution that depends on the available telemetry. The data products $3DX$ and $3DXP$ have the best resolution the instrument can provide, and is usually always available when the spacecraft operates in Burst Mode.

3.5.3 Main issues

There are a number of known issues and caveats regarding PEACE measurements. They are issues that concern top-hat analysers and particle detectors in general and are always a cause of concern in space missions with *in situ* plasma instruments. The most important of them are outlined below.

The first issue is the effect of the spacecraft potential on the measured electrons. A spacecraft orbiting in space, in the environments that Cluster operates in, has usually a small positive electric charge. It ranges from a few eV to tens of eV depending on the technique and the strategy of potential control. The charged

particles that end up in the detectors travel through that potential and are influenced by it. In practice, that means that the electrons are accelerated by a few eV and that the measured velocity distribution is shifted accordingly in velocity space. While this is not a problem for high energies, it has a significant impact on lower energy electrons. In the case where the bulk of the thermal population is in the range of the spacecraft potential, such effect must be taken into account. This issue requires careful calculation of the potential around the spacecraft. It must be noted that, while the spacecraft surface is conductive, there are still minor spatial and temporal anisotropies of the potential around the spacecraft. This means that electrons are not affected equally and in the same way in all directions. In the case of fast rotating spacecraft like Cluster this is mostly due to the differences between the sun-lit and the dark side of the spacecraft. However, usually this effect is small and can be safely ignored or averaged out.

The second issue is the effect of the photo-electrons that are emitted by the sunlight that hits the spacecraft. Due to the positive charge of the spacecraft, the photo-electrons that have energies below the spacecraft potential will return to it, with some of them being captured by the detectors. Although the photo-electron flux can be significant, the bulk of this problem can be mitigated by discarding measurements below the energy of the spacecraft potential. It must be noted however that the actual energy cut-off of the photo-electron population is not always clear and can partially contaminate higher energies. Additionally, given the complex and varying structure of the spacecraft potential, the photo-electron flux is slightly anisotropic. Those effects are usually not very significant and rather complex. A cut-off value at the energy corresponding to the spacecraft potential remains the most widely used approach. However, it must be noted that in some cases where the electron temperature is relatively low and the potential of the spacecraft relatively high (e.g. due to limited potential control), the presence of photo-electrons can dominate the entire thermal part of the electron population. In such cases the estimation of moments of the electron distribution function becomes less reliable. This is frequently the case in the solar wind.

A final issue that is present in most top hat analyzers, including PEACE, and should be mentioned here, is UV-photon produced electrons inside the sensors. Such electrons are produced when UV photons from the Sun (or to a lesser extent from other luminous objects), hit an anode. For that reason the interior of the analyzer plates is covered by appropriate absorbing coating and has a grating

surface. However, such protection does not completely mitigate the effect. When the Sun is directly in the field of view of an anode, the effect will be measurable. It results in a sharp spike at low energies at a specific azimuthal direction once for every spin. It is limited to a single azimuth bin and usually does not have a dramatic impact on the data.

Chapter 4

Methods of data analysis

In this chapter, I present the methods used in the thesis to analyze the in situ data as well as the relevant diagnostics that were performed to test the robustness of such methods.

The first set of methods concerns how to detect regions of strong electric current in turbulent space plasma, usually referred to as current sheets, since these are the regions where reconnection is expected to occur. As it follows from Ampere's law, current sheets are associated with a sharp change of the magnetic field in terms of its magnitude and direction. Three different methods have been used, namely the Partial Variance of Increments (PVI), the magnetic shear angle and the direct computation of current through four-point magnetic field measurements by the curlometer technique.

A second set of methods concerns how to determine the orientation and motion of current sheets in the hypothesis that they are planar structures, that is, their local reference frame and velocity. The frame was estimated using the Minimum Variance Analysis. The timing method was used to estimate the velocity of the current sheet in the normal direction to the current sheet plane. This method also provides the normal direction that has been compared with that from minimum variance for consistency checks.

The last set of methods are related to the estimation of electron temperature from partial distribution functions measured at sub-spin time resolution. These estimates are necessary since the full distribution function are available on spinning spacecraft at spin resolution ($4s$ for Cluster), while the typical duration of current

sheet crossings in the turbulent plasma studied here is of the order of 1s or below. In this chapter I also discuss in detail the diagnostics performed to check the robustness of the sub-spin data analysis, as well as the limitations and caveats associaetd to this analysis. The derived estimates of the electron temperature have been used to study the electron heating associated to the current sheets, as discussed in section 5.

The tests and the diagnostics presented here for the different methods were done by using the same dataset presented in Chapter 5, that consists of $1h30'$ of Burst Mode data in the Earth's magnetosheath downstream of the quasi-parallel bow shock. The Cluster data was provided by the Cluster Science Archive. The data analysis tools used in this work were implemented in MATLAB.The IRFU-MATLAB toolbox (https://github.com/irfu/irfu-matlab) was used to construct the sub-spin distribution functions as well as for data visualization.

4.1 Methods for the detection of current sheets

4.1.1 Partial Variance of Increments

The Partial Variance of Increments (PVI) method has been described in [47] and [48] and has been implemented for the detection and study of intermittent structures such as current sheets in simulations [135] and in solar wind observations [105]. It consists of calculating the change of the magnetic field vector over a time lag τ:

$$|\vec{\Delta B}_\tau(t)| = |\vec{B}(t) - \vec{B}(t+\tau)| \tag{4.1}$$

which is then normalized as follows:

$$PVI_\tau(t) = \sqrt{\frac{|\vec{\Delta B}_\tau(t)|^2}{<|\vec{\Delta B}_\tau(t)|^2>}} \tag{4.2}$$

where $<|\vec{\Delta B_\tau}(t)|^2>$ denotes the time average over the interval that is used to normalize the time series.

This computation produces a time series of the PVI index for a given time lag τ. An example of a PVI analysis in simulation data by [135] is shown in Figure 4.1. Current sheets are associated with sharp gradients of the magnetic field and therefore are expected to appear as large values of the PVI index. The selection of current sheets of different intensity is then obtained by imposing a threshold N on the equation 4.1.1, $PVI_\tau(t) > N$, where $N = 1, 2, 3, ...$ typically indicates a multiple of standard deviations of magnetic field increments. Previous work has established a link between high values of the PVI index and non-Gaussian tails associated with intermittent structures such as current sheets [47, 48, 104]. Specifically, it has been proposed from empirical results, that a PVI index lower than 1 is associated with low intensity Gaussian fluctuations, a PVI index between 1 and 3 is likely to be associated with intermediate structures such as magnetic islands, whereas highly intermittent structures such as reconnecting current sheets are significantly more likely to have a PVI index larger than 3. This aspect will be discussed in more detail in Section 5.1.1, where specific thresholds and selection criteria will be applied to Cluster data. Figure 4.1 also shows the effect of using averaging intervals of different lengths for the normalization of the PVI index. Specifically, the signal becomes weaker as the averaging interval is reduced. It is important to notice here that, for a meaningful PVI analysis, the length of the normalization interval should be much larger than the typical correlation length of the turbulence, that roughly corresponds to the size of the biggest structure in the turbulence. This is expected to provide a stable value of the average as discussed by [135] and also in Section 5.1.1.

It must be noted that the PVI method has been used so far in single spacecraft observations. In those cases, however, there is no information regarding the size and the velocity of the observed current sheets. Using data from multiple spacecraft allows us to observe directly structures of size comparable to the separation between the spacecraft. In this thesis, I have implemented the PVI technique for multi-spacecraft data and used this multi-spacecraft technique to detect the current sheets studied in Chapter 5. The results and the comparison with the single spacecraft approach used in previous studies is discussed in detail in Section 5.1.1.

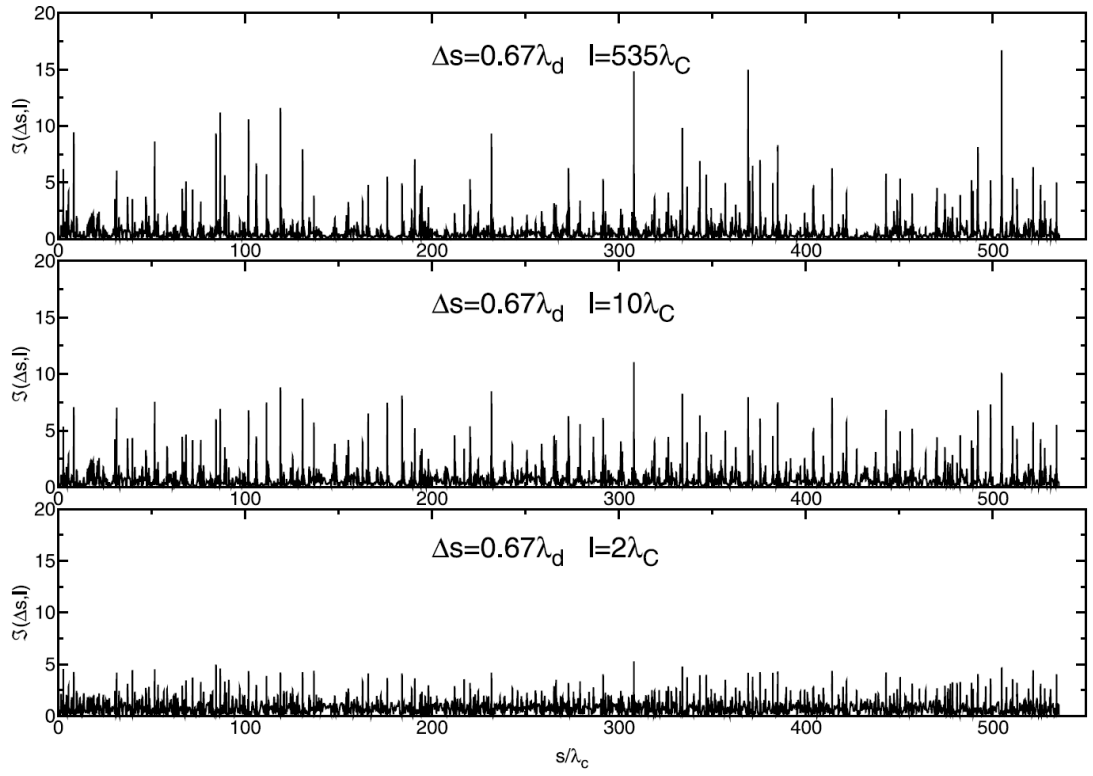

FIGURE 4.1: PVI index with different averaging intervals obtained from simulation results by [135]. The signal becomes weaker as the averaging interval l decreases. λ_C denotes the turbulence correlation length and λ_d the dissipation length as defined in [135]. From [135].

4.1.2 Magnetic Shear Angle

A number of previous studies have focused on the rotation of the magnetic field across current sheets in turbulent plasma [20, 97, 111, 161]. The value of the magnetic shear angle has been used both as an identification method and as an important element for the physical processes occurring within the current sheet, e.g. magnetic reconnection or other instabilities. In these studies, the magnetic shear angle is calculated from single spacecraft measurements of the magnetic field by using the formula:

$$\theta_\tau(t) = cos^{-1} \frac{\vec{B}(t) \cdot \vec{B}(t+\tau)}{|\vec{B}(t)| \cdot |\vec{B}(t+\tau)|} \tag{4.3}$$

where τ is an arbitrary time delay between two measurements.

Figure 4.2 shows an example of current sheet detection in the solar wind by using the magnetic shear angle performed by Miao et al. [97].

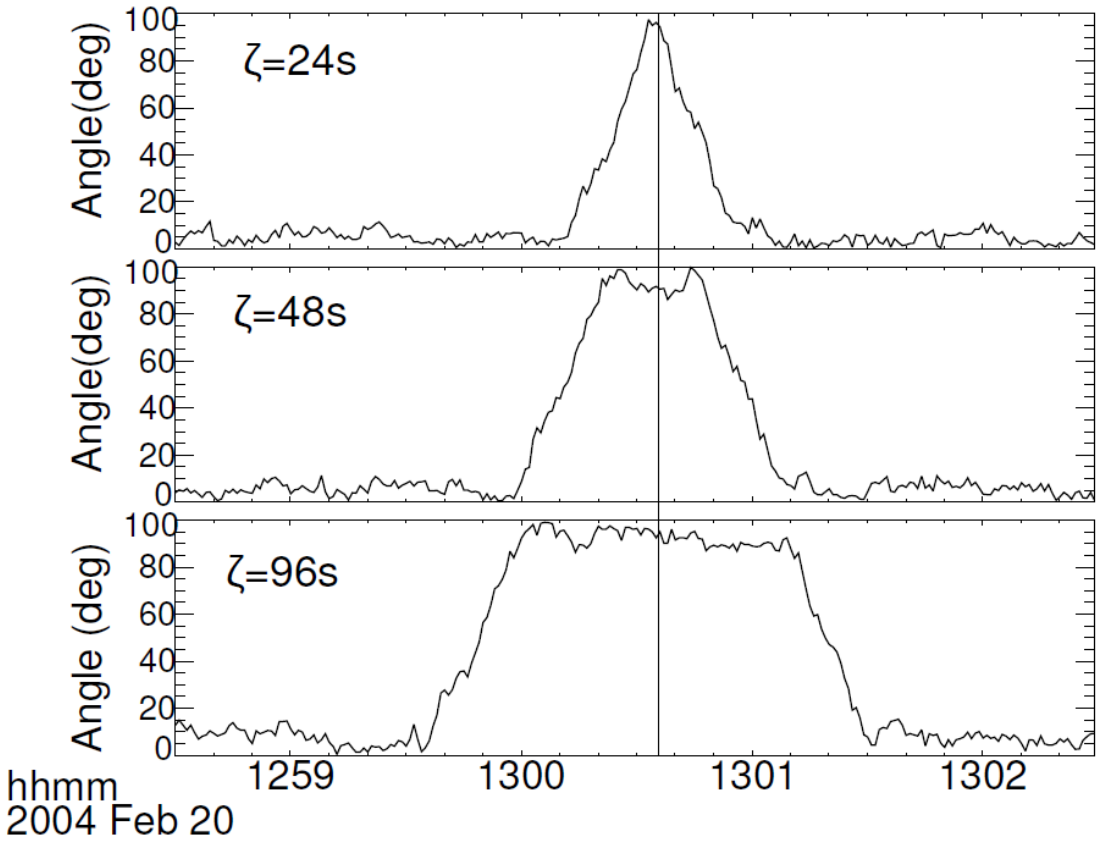

FIGURE 4.2: Example of the calculation of the magnetic shear angle for a current sheet in the solar wind using data from the Ulysses spacecraft [97]. The time lag ζ in the figure corresponds to the lag τ discussed in the text .

The figure shows that, for different values of τ, θ_τ increases gradually to a maximum value that corresponds to the rotation of the magnetic field across the current sheet (shear angle). Once this maximum value is reached, further increase of the values of τ leads to the peak becoming wider, but the maximum value does not change. The time τ_0 it takes to reach the maximum value corresponds to the time it takes for the spacecraft to cross the current sheet. If the velocity of the current sheet is known, then this crossing time can be converted to the actual current sheet thickness.

It should be noticed, however, that if the τ chosen for the analysis is smaller than τ_0, then θ does not reach its maximum value and the magnetic shear as well as the duration of current sheet is underestimated. This could lead to underestimate the thickness of the current sheet. However, as for the case of the PVI index, the magnetic shear angle can also be computed using simultaneous measurements from multiple spacecraft, as discussed in detail in Section 5.1.1. While this limits

the analysis to a given scale set by the spacecraft separation, it allows us to avoid the issue discussed above related to undersampling the current sheet.

4.1.3 Curlometer technique

The curlometer technique is a multi-spacecraft technique that allows us to directly compute the electric current at the barycenter of a tetrahedron of spacecraft such as Cluster [43], by using four-point magnetic field measurements. The main assumption of the method is that the variations of the magnetic field are linear inside the tetrahedron so that non-linear terms of $\bar{B}$ are neglected and the current is assumed uniform over the tetrahedron. Under this assumption, the current is computed through Ampere's law $\mu_0 J = \nabla \times \bar{B}$ in the following way. First, the reciprocal vectors of the tetrahedron $\bar{k}$ are computed:

$$\bar{k}_1 = \frac{\vec{r}_{bc} \times \vec{r}_{bd}}{\vec{r}_{ba} \cdot \vec{r}_{bc} \times \vec{r}_{bd}} \tag{4.4}$$

where $a, b, c, d = 1, 2, 3, 4$ and $\vec{r}_{ij} = \vec{r}_i - \vec{r}j$ which is the vector between spacecraft i and spacecraft j. The vectors are defined by this formula with cyclic permutations of the indices. After this computation, $\nabla \times \bar{B}$ can be estimated using the formula:

$$\bar{LC}[\bar{B}] = \sum_{a=1}^{4} \bar{k}_a \times \bar{B}_a \tag{4.5}$$

where $\bar{LC}$ stands for linear estimation of the curl.

The divergence of the magnetic field $\nabla \cdot \bar{B}$ is estimated in similar way:

$$LD[\bar{B}] = \sum_{a=1}^{4} \bar{k}_a \cdot \bar{B}_a \tag{4.6}$$

where LD stands for linear estimation of the divergence.

As it is demonstrated in detail in [43], the quantity $\frac{\nabla \cdot \bar{B}}{|\nabla \times \bar{B}|}$ serves as an indication of the quality of the current estimation, with small values of this quantity corresponding to good estimations of the current. More recent studies have shown

that this quantity should not be considered a good estimate of the quality of the technique.

A measurement error on the current can be estimated by using the formula:

$$\frac{\delta J}{< J >} = F_S \frac{\delta r}{< r >} + F_B \frac{\delta B}{< B >} \tag{4.7}$$

where $< r >$ is the average separation between the spacecraft, $< B >$ is the average magnetic field respectively, δr and δB are the measurement errors of the separation and the magnetic field respectively, and F_S and F_B are defined empirically in [43].

As mentioned above, the curlometer is based on the assumption that gradients are linear. This is not always the case for thin current sheets, that can have a thickness smaller than the spacecraft separation. The curlometer technique provides an average current over the space of the tetrahedron formed by the four spacecraft. Therefore, sharp gradients at scales smaller than the scale of the separation between the spacecraft tend to be smoothed out, leading to an underestimation of the electric current. This is illustrated in figure 4.3 where one component of the current is estimated for one current sheet using both the curlometer and a single spacecraft estimation of the current through Ampere's, law assuming a planar current sheet moving with constant velocity. The use of the curlometer for detecting thin current sheets and its relationship with other detection methods is discussed in detail in Section 5.1.1.

4.2 Orientation and motion of current sheets

In this section, I will discuss few standard methods to determine the orientation and motion of current sheets. The most important assumption below such methods is that the current sheet is a planar structure where variations occur only in the direction normal to the current sheet plane, as sketched in Figure 4.4. Other assumptions, namely time stationarity for the timing method, are discussed below.

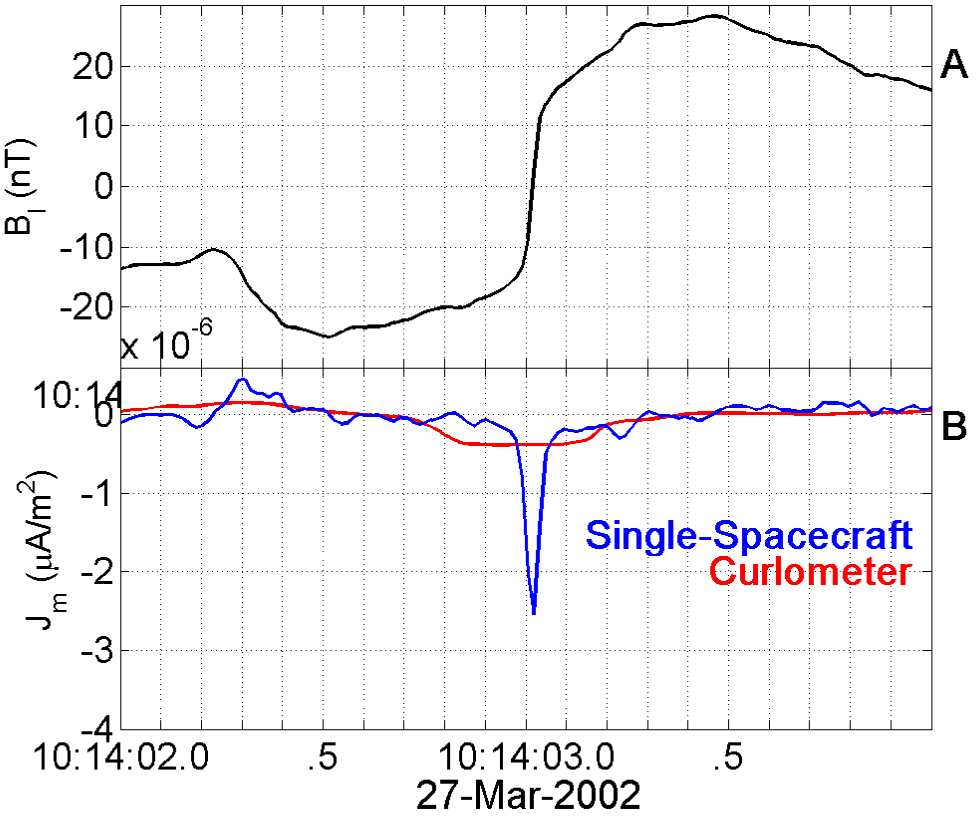

FIGURE 4.3: Estimation of the electric current for a single current sheet. Panel A shows a component of the magnetic field that changes sign across the current sheet. Panel B shows a component of the electric current estimated using a single spacecraft (blue line) and the curlometer technique (red line).

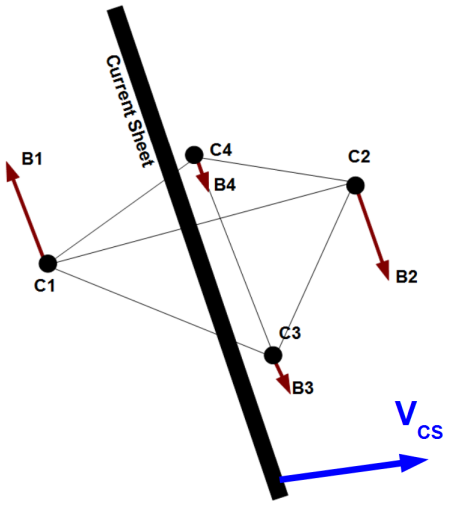

FIGURE 4.4: Configuration of the Cluster spacecraft crossing a planar boundary.

4.2.1 Minimum Variance Analysis

As mentioned above, during the crossing of a current sheet by the spacecraft, we expect to have a variation of the magnetic field along the normal to the current sheet plane. Such direction, as well as the other two directions in the current sheet plane, can be obtained through the minimum variance analysis of the magnetic field [43] and can be used to define a local reference frame for the current sheet. The normal direction is defined as the direction along which the magnetic field has the smallest variation across the current sheet (minimum variance), as follows directly by integrating the equation $\nabla \cdot \bar{B} = 0$ across the current sheet. The direction of the component of maximum variance corresponds to the direction in the current sheet plane along which the magnetic field changes the most. The intermediate variance direction is the second component in the current sheet plane and coincides with the direction of the electric current.

The direction of the normal $\hat{n}$ is the minimum variance direction. It is obtained in spacecraft data by the minimization of the quantity:

$$\sigma^2 = \frac{1}{M}\sum_{m=1}^{M} |(\bar{B}^{(m)} - < \bar{B} > \cdot\hat{n}|^2 \tag{4.8}$$

where M is the number of measurements and $m = 1, 2, 3...M$ at different times.

The minimization of $\hat{n}$ leads to three homogeneous linear differential equations. In matrix form we get:

$$\sum_{\nu=1}^{3} M^B_{\mu\nu} n_\nu = \lambda n_\mu \tag{4.9}$$

where:

$$M^B_{\mu\nu} =< \bar{B}_\mu \bar{B}_\nu > - < \bar{B}_\mu >< \bar{B}_\nu > \tag{4.10}$$

is the magnetic variance matrix. The solution of the system lies in finding the three eigenvalues and the corresponding eigenvectors. The minimum eigenvalue corresponds to the minimum variance. Thus, the direction of the normal $\hat{n}$ is that of the associated eigenvector. Accordingly, the intermediate and maximum

eigenvalues denote the directions of intermediate and maximum variance. Using these three eigenvectors, we define the reference frame of the current sheet. It must be noted that the three eigenvalues correspond to the variances of the field along the direction of the eigenvector, since in the eigenvector basis the magnetic variance matrix becomes $M_{ii}^{B} =< B_i B_i > - < B_i >< B_i >= \lambda_i$.

An indicator of the quality of the analysis is the ratio of the eigenvalue of the intermediate variance to the eigenvalue of the minimum variance. A typical condition is that this ratio should be > 10, although lower values down to about 5 are often considered appropriate as well [43].

4.2.2 Timing Analysis

When the four Cluster spacecraft cross a plasma structure, the timing and position of the individual crossings by each spacecraft can be used to determine its orientation and normal velocity [43], assuming that several conditions are fulfilled. First, the observed structure must be a planar boundary over the scale corresponding to the spacecraft separation. Second, the boundary does not evolve significantly between the crossings by different spacecraft that is, its a stationary structure convected past the spacecraft. If such conditions are fulfilled, one can use the timing and position of the four Cluster spacecraft in order to solve the following system:

$$\begin{pmatrix} \bar{r}_{12} \\ \bar{r}_{13} \\ \bar{r}_{14} \end{pmatrix} \frac{1}{V_{CS}} \begin{pmatrix} n_x \\ n_y \\ n_z \end{pmatrix} = \begin{pmatrix} t_{12} \\ t_{13} \\ t_{14} \end{pmatrix}.$$

The solution to this system of equations gives the direction of the normal $\hat{n}$ and the propagation velocity along the normal V_{CS}. It must be underlined that in cases where the spacecraft separation is very large the assumption of planarity regarding the boundary may no longer be valid. In such cases a Minimum Variance Analysis on each spacecraft can be done. Additionally, contrary to the case of the minimum variance analysis, we have no information regarding the direction of the reconnecting component and therefore timing must be combined with Minimum Variance or other methods to provide the full current sheet reference frame. Finally, the velocity estimated here refers to the velocity normal to the boundary. No

information is provided regarding lateral movement of the boundary, or potential acceleration.

4.3 Estimation of electron temperature at sub-spin time resolution

As described in the previous chapter, the two sensors LEEA and HEEA of the PEACE instrument on board Cluster scan the full sky as the spacecraft rotates, covering all directions once every spin which lasts about $4s$, see Figures 3.9 and 3.10. Each sensor measure electron counts $N(E, \theta, \phi)$ in a given energy range E and two angles θ (elevation angle from the spin plane) and ϕ (azimuthal angle in the spin plane). The phase space density is then obtained as:

$$f(v, \theta, \phi) = \frac{2N(E, \theta, \phi)}{t_a v^4 G(E)} \tag{4.11}$$

where t_a is the accumulation time, $v = sqrt(2E/m_e$ is the velocity associated with the measurement energy and $G(E)$ is the energy-dependent geometric factor of the instrument. The full three-dimensional electron distribution function is then obtained by combining all such distribution functions over the $4s$ spin period. The moments of the distribution function are calculated from the full three-dimensional distribution by integrating the distribution function in the velocity space, according to the following formula [7, 79].

$$M(\vec{x}, t) = \int \vec{v}^r f(\vec{v}, \vec{x}, t) d^3\vec{v} \tag{4.12}$$

The first several moments density, velocity and temperature are the most used:

$$n(\vec{x}, t) = \int f(t) d^3\vec{v} \tag{4.13}$$

$$\vec{v}(\vec{x}, t) = \int \vec{v} f(t) d^3\vec{v} \tag{4.14}$$

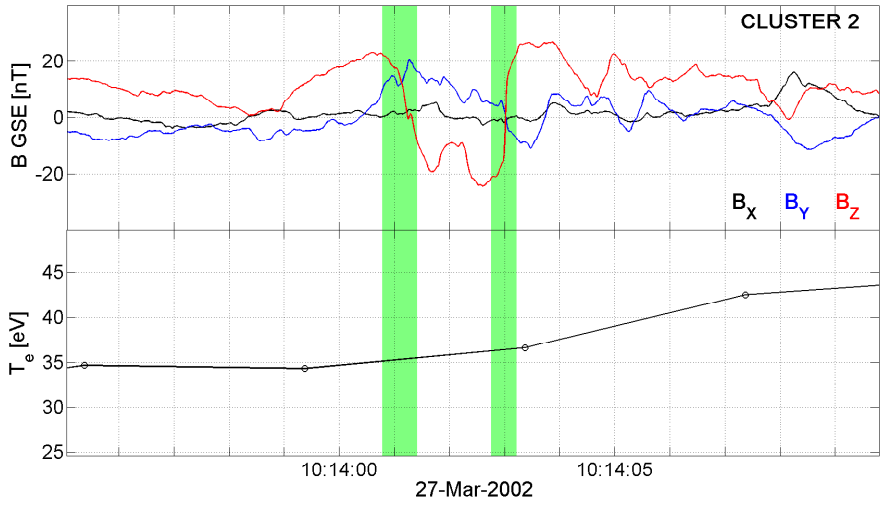

FIGURE 4.5: Interval of Cluster 2 measurements of magnetic field (top panel) and electron temperature (bottom panel) measured at spin-resolution by PEACE. Green shading highlights the detected structures. Interval of $1h30'$ of in the Earth's magnetosheath. PEACE and FGM data provided by the Cluster Science Archive.

$$\vec{\vec{P}}(\vec{x},t) = m_e \int (\vec{v}-\vec{V})(\vec{v}-\vec{V}) f(t) d^3\vec{v} \tag{4.15}$$

where m_e is the electron mass. The last equation gives the pressure tensor, which using the definition $\vec{\vec{P}} = Nk\vec{\vec{T}}$ can be converted to the temperature tensor. The scalar temperature can be obtained from the trace of the associated tensor $T = Tr(\vec{\vec{T}})/3$. The moments obtained by the procedure discussed above have a time resolution that the same of the three-dimensional distribution function and is at best equal to the spacecraft spin period. However, as discussed already earlier, my work investigates proton-scale current sheets which have thicknesses much smaller than the spatial scale corresponding to the spacecraft spin. For the case of the magnetosheath studied in this thesis, the typical ion gyroradius/inertial length is $\sim 50-100km$ and the typical current sheet velocity $\sim 100-200km/s$, yielding a typical duration of the current sheet crossing $\sim 1s$ and below. This means that the spin-resolution data products are not sufficient to study electron heating within such structures. Figure 4.5 shows an example of two current sheets detected in the Earth's magnetosheath. In the lower panel we see that the temperature calculated at spin-resolution has too low time resolution to give any information about heating within these sheets.

Since the time resolution of full three-dimensional distribution functions is set

by the spin period, it is not possible neither with Cluster nor with any other currently available spacecraft to obtain the electron temperature at higher time resolution. In the future we will use data from the recently launched spacecraft NASA/MMS, which is able to provide full electron distribution at $30ms$ time resolution. However, the Cluster/PEACE detector measures two-dimensional slices of the full electron distributions at sub-spin time resolution ($\sim 120ms$) that can be used to study small-scale physics [64, 101, 123, 132, 152] and provide, under certain assumptions, a proxy of the electron temperature at high time resolution. This proxy has been used in this thesis to study electron heating within current sheets in turbulence, as discussed in detail in Chapter 5. The details of such sub-spin estimations together with its assumptions and diagnostics are discussed below. It should be noted that a similar approach is also used in planetary measurements on non-spinning spacecraft such as the Cassini spacecraft [79], where the instrument does not provide full coverage of the distribution function.

4.3.1 Implementation

In Burst Mode, the PEACE electron instrument measures slices of the full three-dimensional electron distribution function having a width of 11.25^o in azimuthal direction (spin plane) and of 180^o in elevation angle (away from spin plane), as sketched in Figure 3.10). The resolution in elevation angle is 15^o, that is, there are 12 bins in that direction. Since the Cluster spin period is about $4s$, one has 32 such slices over one spin each corresponding to a time resolution of about $125ms$. For each slice, PEACE scans a different number of energy bins in the nominal energy range of the instrument, depending on the particular instrument mode (see Section 3.5). In this thesis, I have mostly used LEEA data since the average temperature of electrons in the magnetosheath is relatively low $\sim 30eV$. The most frequent LEEA mode that I used has 32 energy bins and energy coverage in the range $5eV - 2.5keV$.

The construction of sub-spin distribution functions has been performed by using routines available on the IRFU-MATLAB package. The PEACE data products on the Cluster Science Archive do not provide any explicit timing information for each of the sub-spin measurements. The timestamps of each sub-spin measurements are instead reconstructed combining the azimuthal angle of each measurement

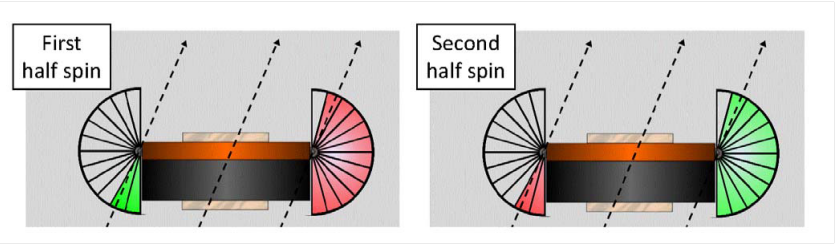

FIGURE 4.6: Pitch angle coverage of the PEACE detectors with respect to the magnetic field orientation. From [39].

with the spin rate of the spacecraft. The 12 elevation angle bins of each two-dimensional slice are converted into pitch angles by projecting the direction of each bin onto the magnetic field measured by the FGM at high-time resolution ($67Hz$ corresponding to a 0.015 s) and averaged over the $125ms$ duration of the subspin measurement. It should be noted that, as the spacecraft spins, the electron distribution in the direction perpendicular to the magnetic field will be measured at all times. However, the electron distribution in the parallel/antiparallel direction is measured only when the magnetic field is aligned/anti-aligned with the field of view of the detector (see figure 4.6). For a generic orientation of the magnetic field, this happens only twice during each spin (once for parallel and once for antiparallel), assuming that the magnetic field orientation does not change much over the spin.

Therefore it is not possible in general to measure both perpendicular and field-aligned directions at sub-spin time resolution. In such case, a proxy of the total temperature can be instead be derived by averaging over all elevation angles. This proxy of the temperature has been used in the first part of my work presented in 5.1, where I performed a statistical analysis of the electron heating in thin current sheets. However in the very specific case when the magnetic field is very close to being parallel/antiparallel to the spin axis, both perpendicular and field-aligned directions can be measured at sub-spin time resolution, as reported earlier by [132] and discussed in Section 5.2 where I studied in detail the heating mechanisms within a single current sheet.

The computation of the proxy of the total electron temperature obtained from sub-spin distributions relies mainly on two conditions, which are well satisfied for the case of magnetosheath studied here. The first condition is that the two-dimensional slices of the distribution function are well representative of the thermal part (core) of the full distribution. This happens because the thermal speed of electrons is

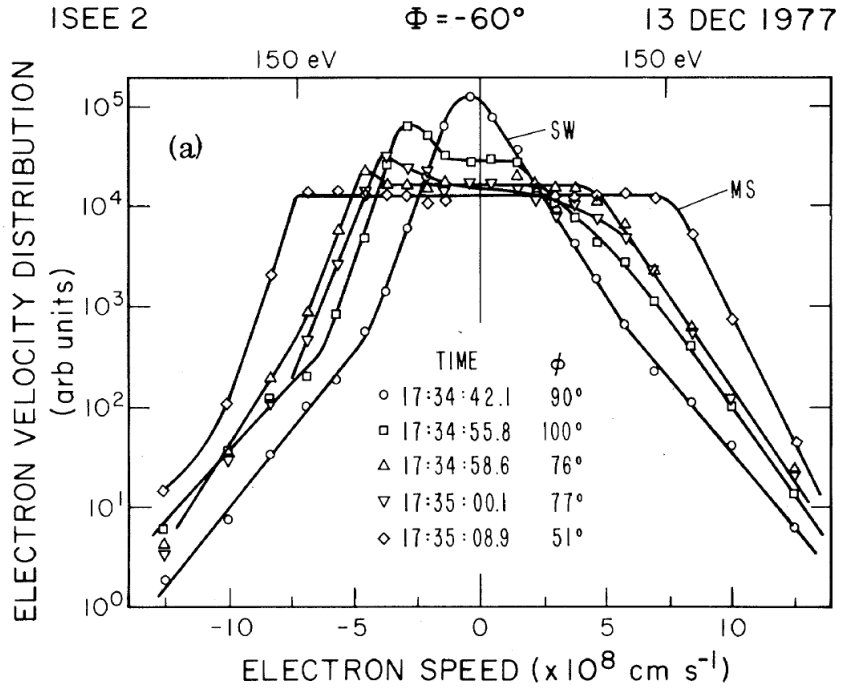

FIGURE 4.7: Electron distributions in the solar wind and the magnetosheath. ISEE-2 measurements. From [40].

typically much larger than the bulk flow speed, so that electrons usually fill all the anodes of the detector. It should be noted that this is not true for protons in the magnetosheath (and even more for the solar wind) where protons are recorded mainly in the anodes that are close to the flow direction. For this reason, a sub-spin proton analysis is not straightforward to implement and has not been performed here. The second condition is that the anisotropy of the core of the distribution function is small, so that the average of the distribution function over all measured polar sectors is not very different from the value in each sector. This is usually true for solar wind electrons, see Figure 4.8, as well as for magnetosheath electrons close to the bow shock, which are solar wind electrons that have been recently heated across the bow shock as shown in Figure 4.7, reporting the evolution of the electron distribution function from the pristine solar wind, through the bow shock and into the magnetosheath. The isotropy of the core of the distribution function has been verified directly for the event studied here. As shown in Figures 4.7 and 4.8 anisotropies of the electron distribution functions are observed but typically at energies larger than the thermal energy (supra-thermal range) which were not considered in this study.

The estimation of the temperature proxy was performed by implementing two

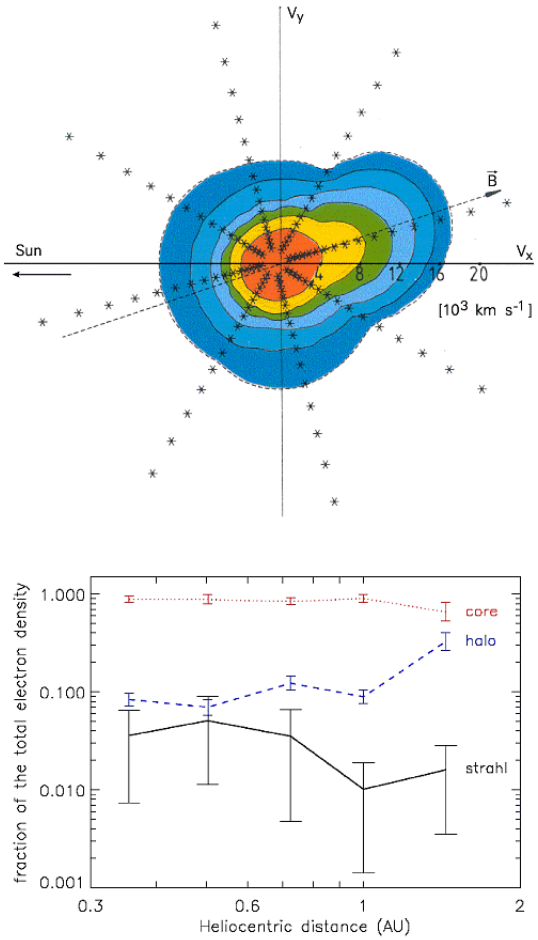

FIGURE 4.8: The top panel shows an electron distribution function in the solar wind as measured by the plasma instrument on the Helios spacecraft at 1 AU. (after [115]). The bottom panel shows evolution of the core, halo and strahl with heliocentric distance from the Sun according to the Helios, WIND and Ulysses measurements (after [84]). Adapted from [87].

different methods. The first approach assumes that the core of the distribution is Maxwellian. In that case the maximum of the differential energy flux $dEF_e(E) = 2\frac{E^2}{m_e^2} f_e(E)$ is twice the temperature T_e [79]. Visual inspection of the electron distribution functions indicates that the core is indeed well represented by a Maxwellian and confirms the validity of the method. Additionally this approach was found to be less sensitive to fluctuations of low energy photoelectrons that contaminate the distribution and was therefore more robust.

The second approach was to directly fit a Maxwellian distribution to the data. This allows to estimate both the temperature and the density. The function that was used for the fit had the form: $f(E) = C(\frac{n}{kT})^{3/2} e^{\frac{-(E-E_0)}{kT}}$, where C for the SI is $C = 0.86 \cdot 10^6$. In the above, it was assumed that $E_0 << E$ for the thermal part of the distribution. The electron bulk flow velocities in the magnetosheath

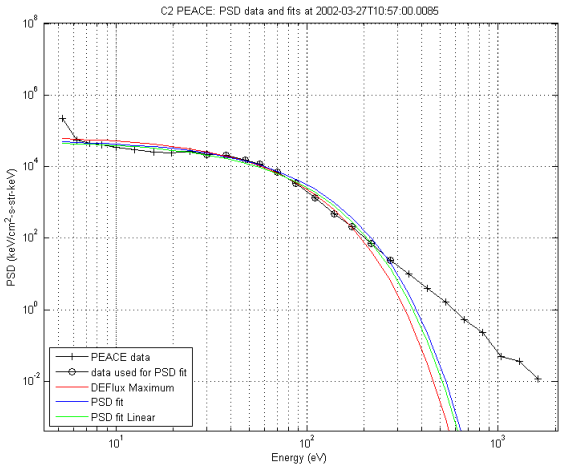

FIGURE 4.9: Example of an electron distribution function in the Earth's magnetosheath, measured at sub-spin time resolution. The black crosses are the measurements by PEACE. The black circles are the subset that were used to estimate the temperature, after excluding low energy photo-electrons and high energy non-thermal electrons. The red line was produced using the temperature estimated by the maximum of the differential energy flux and the density measured by WHISPER. The blue and green lines are the fits of a maxwellian using a non-linear least squares method (blue line) and a linear least squares method on logarithmic space (green). PEACE 3DXPL data provided by the Cluster Science Archive.

correspond to energies of the order of magnitude of a fraction of eV. The thermal velocities on the other hand, given that the average temperature is of the order of $30eV$, are much higher. Therefore, it follows that $kT_e >> v_e$, which justifies the assumption that $E_0 << E$. The fit is a non-linear least squares fit that was implemented by using a Levenberg-Marquardt algorithm and by using the average temperature and density as initial guess values. An alternative approach was to take the logarithm of the data, since in this case the expression for the maxwellian becomes a linear function and a simple least-squares approach can be used. An example of a sub-spin electron distribution function with these three different estimations is shown in Figure 4.9. Since we are interested in the thermal core of the distribution, we excluded the high energy part of the distribution which is dominated by the non-thermal halo and limited the analysis to energies smaller than $\sim 1keV$. Additionally, the very low energies are dominated by the photo-electrons emitted by the spacecraft, which were also excluded. The specific thresholds depend on instrument limitations and are discussed in Section 4.3.3 below.

4.3.2 Diagnostics

In order to evaluate the quality of the estimations of the electron temperature proxy obtained from the sub-spin distribution functions, I compared to the spin-resolution temperature which is computed from the three-dimensional full distribution function (middle panel of Figure 4.10). The sub-spin estimations of T_e were found overall in good agreement with the spin-resolution temperature. In addition, the density obtained by the maxwellian fit was compared to the density measured by PEACE at $4s$ resolution, but also with the density measured by the EFW and WHISPER instruments at higher time resolution (bottom panel of Figure 4.10). The differences between sub-spin and spin resolution values of the temperature give an indication of the error associated to the sub-spin estimations. For this case, the difference is $\sim 10\%$ which corresponds to $\sim 3eV$, given that the average electron temperature for this event is $\sim 30eV$. When compared with the spin-resolution temperature measured by PEACE, the estimation given by the maximum of the differential energy flux appears more robust and accurate compared to the one given by the maxwellian fit. The deviations observed between the latter and the spin-resolution temperature are justified in part by the issues highlighted in the following section. Consequently, the estimation that was used in the results presented in Chapter 5 was the one given by the maximum of the differential energy flux.

4.3.3 Instrumental Limitations

Since the temperature in the magnetosheath is dominated by the core of the distribution function, we have limited the energy range to the core ($E < 832eV$) and exclude supra-thermal electrons. At low energies, the photoelectrons emitted by the spacecraft dominate. These electrons are excluded from the analysis using the spacecraft potential as a threshold as measured by the EFW instrument.

One observed effect was a sinusoidal modulation of the temperature. This effect was subtle but persistent with an amplitude of $\sim 1eV$. It is clearly shown in Figure 4.11 for one spin period averaged over an hour of data. According to feedback from the PEACE and EFW teams, this is not due to an anisotropy of the plasma but is thought to be an instrumental artifact. It is an effect due to the anisotropic structure of the spacecraft potential and photoelectron cloud

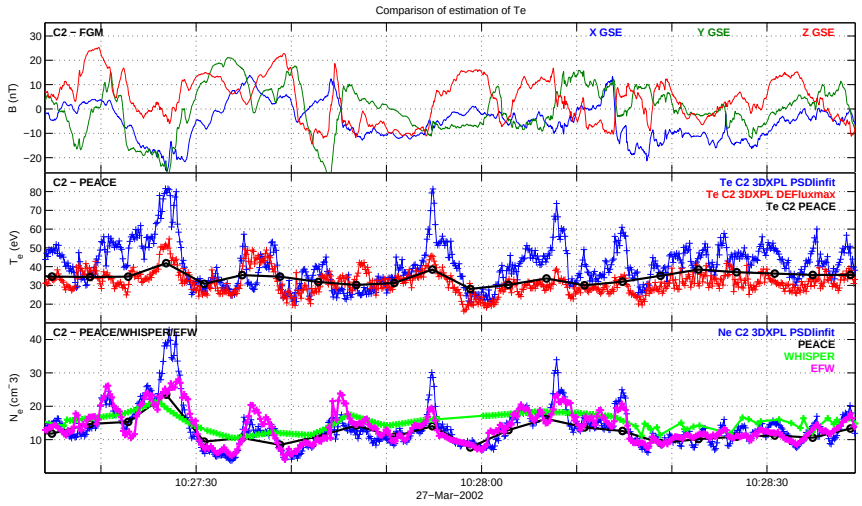

FIGURE 4.10: Comparison of estimated electron temperature in the Earth's magnetosehath. The top panel shows the magnetic field measured by FGM for Cluster 2. The middle panel shows the spin-resolution temperature estimated by PEACE (black line), the sub-spin estimation produced by the maximum of the differential energy flux (red line) and the maxwellian fit (blue line). The bottom panel shows the density estimated by PEACE (black), EFW (magenta), WHISPER (green), and the estimation from the maxwellian fit on the sub-spin data (blue). Data provided by the Cluster Science Archive.

around the spacecraft. Specifically, due to the differences between the sun-lit and dark side of the spacecraft and its rotation. It must be also noted that while the spacecraft surface is conductive within the specified parameters, the conductivity of different parts varies. These phenomena, while they do not influence much the calculation of particle moments at spin resolution, they have an impact at sub-spin electron measurements. As it is shown in Figure 4.11 that effect is mitigated to a certain extent by raising the photo-electron cut-off energy level. In that case the maxwellian fits with both methods tend to converge towards the estimation obtained by the maximum of the differential energy flux. The latter approach is more robust than the maxwellian fits since it relies on the maximum of the energy flux and is not influenced by fluctuations at low energies. Additionally, it must be noted that limiting the energy range of the fit by raising the cut-off energy for the photo-electrons, although it mitigates this problem it jeopardizes the quality of the estimation since the fit is done over a smaller number of data points. In this work the observed variations due to the spin modulation were considered to be within the errors of our method, which was estimated at $\sim 10s\%$.

Another instrumental artifact was a sharp peak observed at low energies when the detector was facing towards the sun. This is caused by photo-electrons emitted

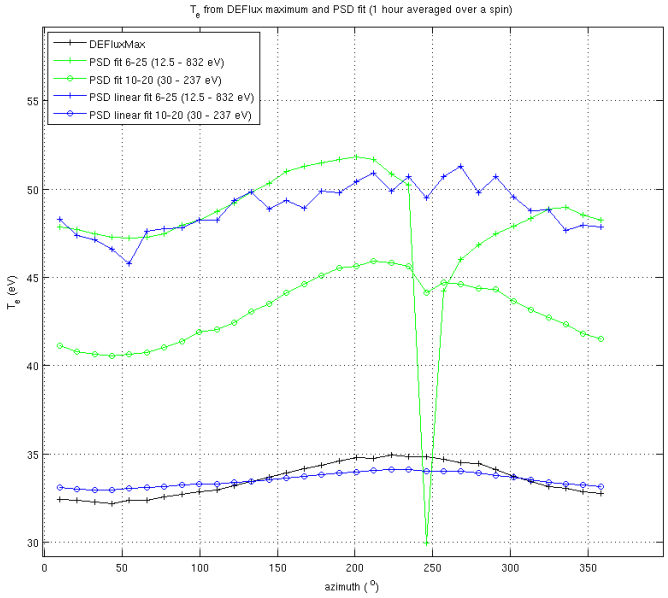

FIGURE 4.11: Electron temperature estimated with different methods over one spin, averaged over one hour of data. The black line is the temperature estimated by the maximum of the differential energy flux. The blue and green lines are the fits of a maxwellian using a non-linear least squares method (blue line) and a linear least squares method on logarithmic space (green) for two different energy ranges. Interval of $1h30'$ of in the Earth's magnetosehath. PEACE 3DXPL data provided by the Cluster Science Archive.

inside the anodes of the detector by solar UV radiation, seen in figure 4.12. This is a known issue in such detectors and is mitigated to an extent by the design of the detector, mainly by grating design of the interior surface of the optics and coating with UV-absorbent materials. It is highly directional and impacts mostly low energies. It skews the estimation of the electron temperature in the case of a maxwellian fit as seen by the negative spikes in Figure 4.11. As it can be seen in Figure 4.11, it is somewhat mitigated when the fit is done at a more narrow energy range which is less influenced by the low energy part of the distribution. The linear fit in logarithmic space produces a more robust result compared to a non-linear fit. This is expected since by taking the logarithm of the probability distribution one essentially applies statistical weights to the distribution so that the least squares fit is less influenced by the low energy part which in this case is problematic. The non-linear least-squares fit on the other hand is dominated by the low energy part of the distribution that has values higher by order of magnitude. Hence it deviates more when there are fluctuations in the low energy part due to instrumental effects. The alternative approach of estimating the temperature by taking the maximum of the differential energy flux, however, is consistently more robust. The peak of

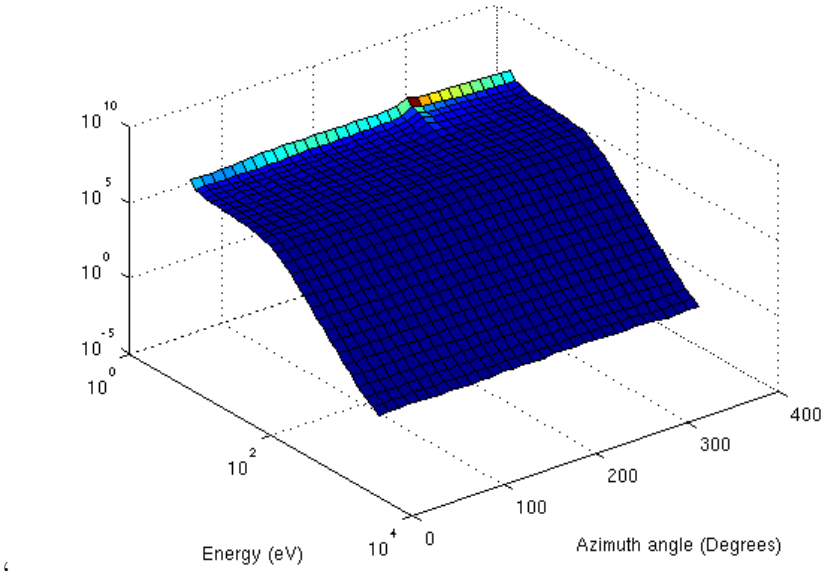

FIGURE 4.12: Electron distribution function over one spin, averaged over one hour of data. The spike observed in low energies coincides with the sun-ward direction. Interval of $1h30'$ of in the Earth's magnetosehath. PEACE 3DXPL data provided by the Cluster Science Archive.

the differential energy flux lies at higher energies, at around $\sim 60eV$. Therefore, fluctuations of the flux at much lower energies, such as the one caused by the UV radiation, do not impact this estimation.

Chapter 5

Results

The near-Earth space offers a unique natural laboratory to experimentally study turbulent reconnection as a mechanism of energy dissipation and particle heating at kinetic scales in turbulent plasmas, thanks to in situ spacecraft measurements of both electromagnetic fields and particles at high resolution. The turbulent solar wind plasma, in particular, is a key environment to perform such studies both for the case of the so-called pristine solar wind (upstream of the Earths bow shock) and for the case of the shocked magnetosheath (downstream). The pristine solar wind and the magnetosheath have different turbulence properties and plasma conditions, such as the amplitude of turbulent fluctuations, compressibility, homogeneity and Mach number, so that comparing observations of turbulent reconnection in both regions can help understanding how turbulent reconnection depends on such conditions. The work presented in this thesis focuses on Cluster measurements in the magnetosheath downstream of the Earth's quasi-parallel bow shock. The quasi-parallel portion of the shock is where the normal to the shock is almost parallel to the interplanetary magnetic field in the pristine solar wind (Figure 5.1).

One main reason for focusing on the quasi-parallel magnetosheath is the fact that the turbulence therein is one of the strongest in the near-Earth space and it is comprised of a large number of thin current sheets where reconnection is expected to occur, as indicated by earlier observations [124, 141] and supported by recent kinetic simulations [63]. Figures 5.1 and 5.2 show results of kinetic simulations where the quasi-parallel magnetosheath is abundant of thin current sheets and small-scale magnetic islands, while such structures are infrequent downstream of

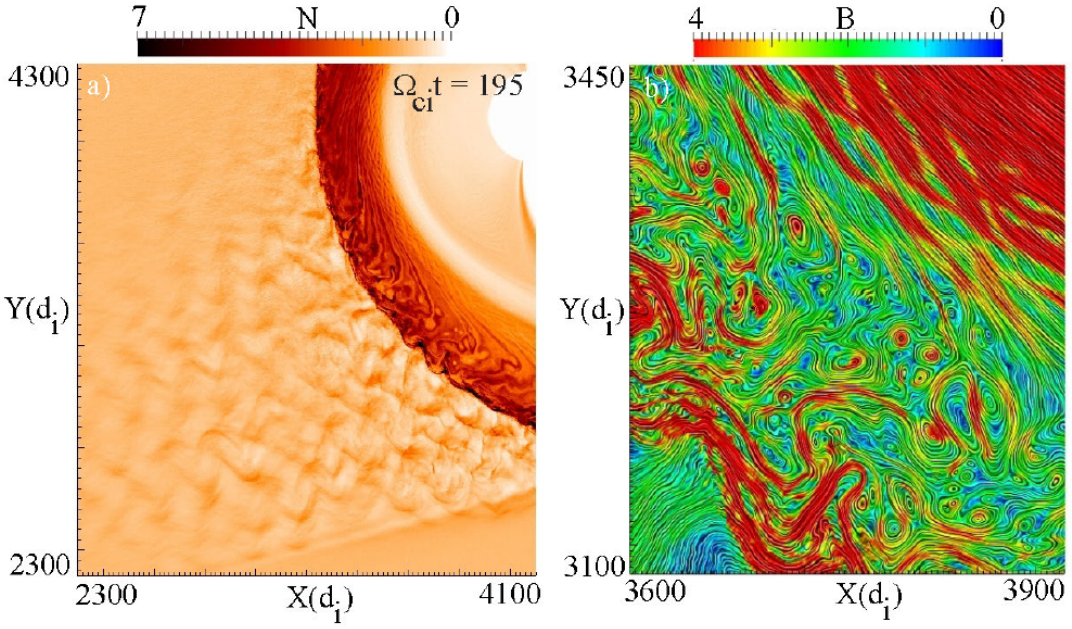

FIGURE 5.1: Results of large-scale kinetic simulations of the Earth's bow shock and magnetosheath [63]. The left panel shows the density. The right panel shows the magnetic field lines colored from blue to red for increasing values of $|B|$. Strong turbulence and the formation of small-scale magnetic islands and current sheets is a common feature of the quasi-parallel magneotsheath.

the quasi-perpendicular magnetosheath [63]. This simulation also shows that the strongest plasma heating is found where thin current sheets and islands are located (see Fig. 5.2), strongly suggesting that the heating is locally produced within such structures by processes at kinetic scales.

Another important reason for focusing on the magnetosheath is that the measurements required to resolve kinetic physics suffer less limitations in the magnetosheath when compared to the pristine solar wind. The amplitude of magnetic fluctuations is higher in the magnetosheath and the noise level of the magnetometers is normally not an issue. The DC electric field is less affected by wake effects since the shocked solar wind is slower. Furthermore, the typical amplitude of the reconnection electric field is higher in the magnetosheath and is therefore less affected by the limited accuracy of DC electric field measurements. Finally, the thermal energy of electrons in the magnetosheath is higher than that of photoelectrons and the bulk flow is lower compared to the thermal velocity, contrary to the pristine solar wind, making much easier to compute electron moments as discussed in Chapter 4.3.

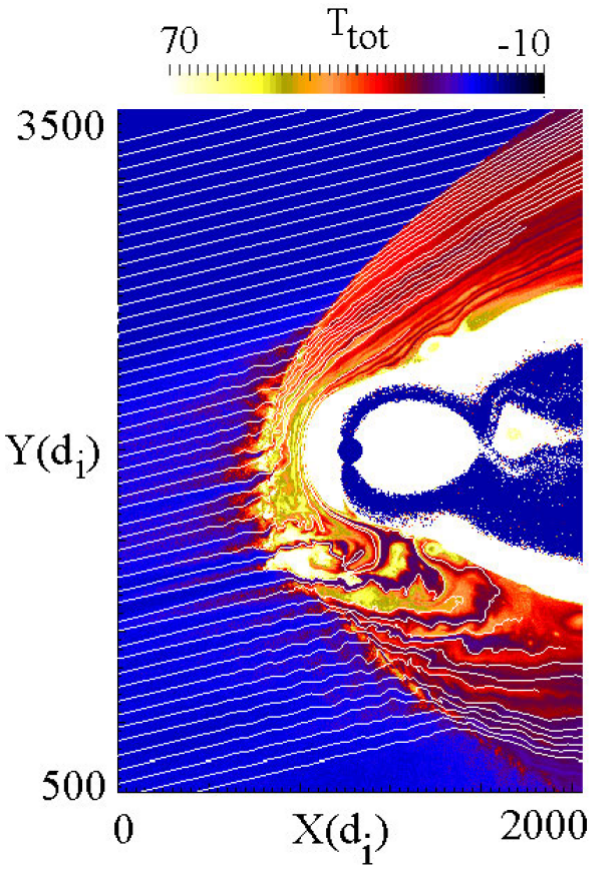

FIGURE 5.2: Total ion temperature of solar wind plasma around the shock region and in the magnetosheath [63]. The white lines denote the magnetic field lines. The heating is stronger in the quasi-parallel magnetosheath with respect to the quasi-perpendicular one

Published experimental evidence of turbulent reconnection and associated particle heating at kinetic scales is scarce. Magnetic reconnection in turbulent plasma has been observed for the first time by Cluster within proton-scale current sheets downstream of the quasi-parallel shock [124] and has been considered as an important mechanism of dissipation of turbulent energy at kinetic scales [141]. Other recent studies have investigated current sheets and reconnection in the pristine solar wind [20, 44, 72, 97, 105, 161]. However, it was not possible to establish a direct link with kinetic scales and dissipation due to the low time resolution of measurements and limitations of particle measurements. Recent Cluster observations have shown the presence of sub-proton scale current sheets in the pristine solar wind but no direct evidence of reconnection was given due to the lack of electric field and particle measurements [111]. Despite these observations, no statistical study on reconnecting current sheets and associated particle heating at kinetic scales is currently available. This thesis attempts to perform such study

by using Cluster observations downstream of the quasi-parallel shock and extending the results by Retinò et al. [124] and Sundkvist et al. [141]. In addition to the statistical study of thin current sheets and associated electron heating, in the thesis I have also investigated which are the physical mechanisms responsible for the observed heating. Such mechanisms have been experimentally studied in large-scale laminar reconnecting current sheets at the Earth's magnetopause [45] and magnetotail [36, 57, 125], but not within small-scale current sheets in turbulence, where different physical phenomena may dominate.

The presentation of the results is structured in two main parts. The first part (section 5.1) is a statistical study of the properties of thin current sheets observed in turbulent plasma downstream of the quasi-parallel shock, with a focus on the electron heating observed within such structures. This first part has been published in the paper Chasapis et al. [17], which is included in Appendix A. The second part of the results (section 5.1.3) is focused on one particular current sheet which is studied in detail to provide evidence of reconnection and to investigate the mechanisms of electron heating. This part of the results is the subject of a paper in preparation.

During the thesis, I have also considered possible heating mechanisms other than reconnection for the same event of quasi-parallel shock turbulence. In particular, I have considered one case of a steepening wave that could be consistent with the formation of a small-scale shock, for which substantial electron heating is found. I have also started to investigate thin current sheets in the pristine solar wind as well as in Saturn's magnetosheath, aiming to compare to the case of the quasi-parallel shock. Yet, due to limitations of the data and lack of time, the results on this part are very preliminary and are only discussed in 6 along with several ideas for future work.

5.1 Statistics of thin current sheets

The first part of my work is a statistical study of thin current sheets in the quasi-parallel magnetosheath by using Cluster spacecraft data. First, I studied different methods for detecting current sheets by using both single-spacecraft and multi-spacecraft data (5.1.1). After careful diagnostics and comparison among different approaches, the Partial Variance of Increments (PVI) on multi-spacecraft data

proved to be the most robust and reliable approach for this study. The next step was to examine the properties of the detected current sheets. A number of properties were examined, starting from the magnetic shear angle (i.e. the rotation of the magnetic field across the current sheet) and its relationship with the PVI index. The main conclusion of this analysis has been establishing the presence of two distinct populations of high and low PVI and different shear angle, with significantly different properties. In this part, I have also studied the distribution of current sheet waiting times (i.e. the distance between two different current sheets) and the spatial distribution of current sheet with respect to the distance from the shock. The final step was to study the local increase of the electron temperature inside each current sheet and to investigate the statistical properties of heating within current sheets (5.1.3). This was done by estimating the temperature at high time resolution using the partial distribution functions measured at sub-spin time resolution. The main result is that significant heating is consistently observed for the high PVI population, whereas low or no heating occurs in low PVI current sheets.

The statistical study has been performed on a Cluster spacecraft event earlier studied by [124, 141] to provide evidence of reconnection. However, the analysis of electron data was not performed in detail therein. The event occurred on March, 27th 2002 and lasted about one and a half hour ($9h35'$ to $11h05'$), during which the spacecraft were in the Earth's magnetosheath downstream of the quasi-parallel shock (Figure 5.3). During the event, the separation of the four Cluster spacecraft was $100km$, which is comparable to the local proton inertial length $d_i = c/\omega_{pi}$ (where ω_{pi} is the proton plasma frequency). This event is therefore ideal to study structures having scales of the order of d_i and slightly below, while electron scales $\sim d_e = c/\omega_{pe} \sim 2km$ cannot be studied with the available data. Another important feature of this event is the fact that many of the instruments onboard the spacecraft operated in high-resolution mode (Burst Mode). This aspect was crucial, in particular to obtain high resolution measurements of the electron distribution functions. Panels A and B of Figure 5.3 show the crossing of the bow shock around $9h35'$ and the entry of Cluster spacecraft in the very turbulent quasi-parallel shock region, characterized by high magnetic field $\delta B/B \sim 1$ and density $\delta N/N \sim 1$ fluctuations. Panel C presents one component of the magnetic field during a shorter interval of time where the detected current sheets are highlighted. The shock becomes quasi-perpendicular around $11h30'$ and the number of current sheets dramatically decreases (not shown), confirming that thin

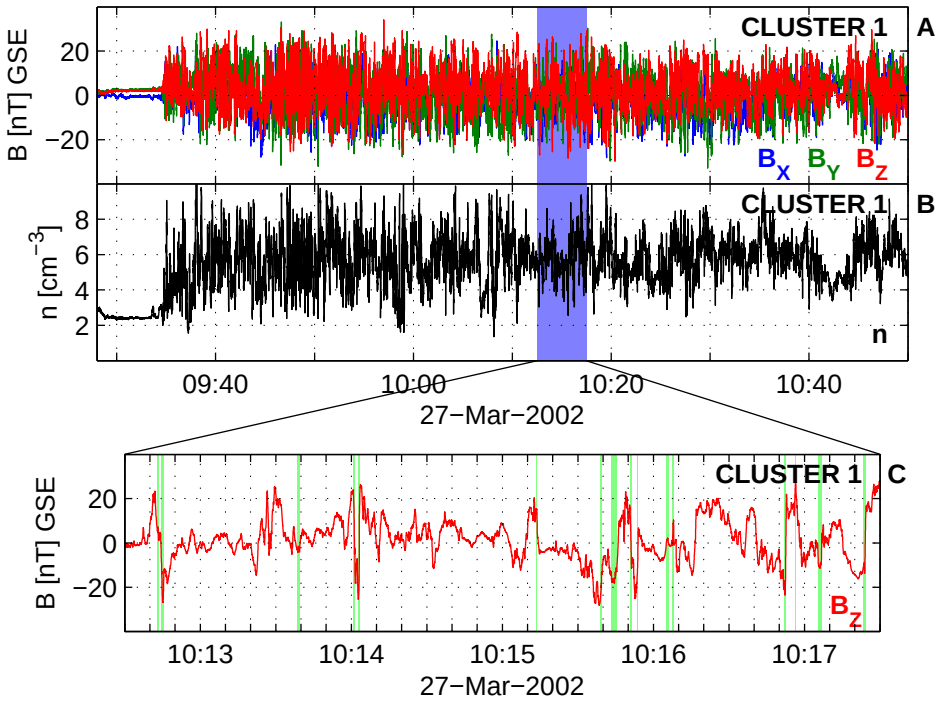

FIGURE 5.3: Interval of magnetic field data from Cluster 1 in the GSE coordinate system. Panels and B show respectively the evolution of the magnetic field components and the density during the interval used for this analysis. The four spacecraft cross the bow shock at 09:35 and enter into the magnetosheath. Panel C shows the z-component of the magnetic field during a shorter interval. The detected current sheets are shown by green highlighted bands.

current sheets are indeed a very specific properties of quasi-parallel magnetosheath turbulence.

5.1.1 Detection of current sheets

In this section I describe the techniques that I used to detect thin current sheets for the event of quasi-parallel magnetosheath turbulence studied in this thesis. As discussed in Section 4.1, current sheets can be detected through the PVI method, the magnetic shear angle or computing directly the current through curlometer and all these methods have been used in earlier studies [20, 97, 111, 124, 141, 161]. While the last method is a multi-spacecraft method, the first two have been earlier applied to single spacecraft data. In this thesis, I have implemented a multi-spacecraft version of both the PVI and the shear angle calculation and I have

compared with the same methods but applied to single spacecraft data. After comparing all these methods, the conclusion has been that the multi-spacecraft PVI is the most efficient method to detect thin current sheets for the case of magnetosheath turbulence which, as discussed below, is comprised not only by rotations of the magnetic field but also by regions of strong currents related to gradients in the magnitude of the magnetic field.

As mentioned in chapter 4.1, in past studies the PVI index has been calculated with data from a single spacecraft at increments separated by a time delay τ. The value of τ was set to correspond to the spatial scale of interest, assuming that structures are convected at a typical velocity past the spacecraft. In the case of Cluster, however, the four spacecraft provide multiple simultaneous measurements at the scale of the separation of the spacecraft. For the event studied here the separation of the spacecraft is comparable to the proton gyroradius, which allows us to focus on current sheets of that scale only. The multi-spacecraft PVI is calculated by using the increments of the magnetic field measured simultaneously by a couple of spacecraft separated by a distance d: $|\Delta\vec{B}_d(t)| = |\vec{B_{r+d}}(t) - \vec{B}_r(t)|$. This gives the following equation:

$$|\Delta\vec{B}_{ij}(t)| = |\vec{B}_i(t) - \vec{B}_j(t)| \tag{5.1}$$

which is then normalized as follows:

$$PVI_{ij}(t) = \sqrt{\frac{|\Delta\vec{B_{ij}}(t)|^2}{<|\Delta\vec{B}_{ij}|^2>}} \tag{5.2}$$

where i and j denote each pair of the four Cluster spacecraft and $<|\Delta\vec{B}_{ij}|^2>$ denotes the time average over the span of the time series. The normalization was done by averaging over the entire $1h30$ interval. This interval corresponds to a spatial scale $\sim 10^6 km$ that is much larger than the typical correlation length of the turbulence which is estimated to be $\sim 2000 km$ (~ 50 proton scales).

A comparison of the results of PVI analysis between single and multi-spacecraft approach is shown for one specific current sheet in Figure 5.4 for different values of time delay τ.

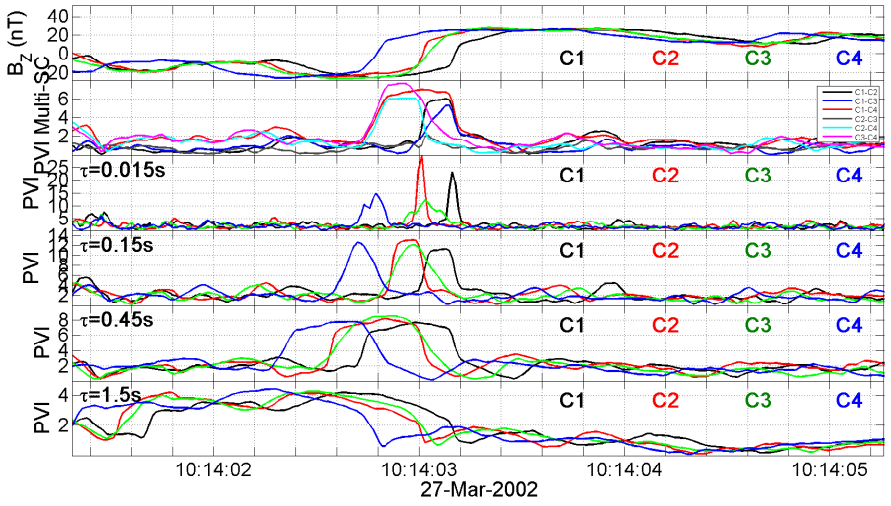

FIGURE 5.4: PVI index during the crossing of a current sheet detected in the Earth's magnetosheath. The first panel shows the full resolution magnetic field data ($67Hz$) in GSE coordinates. The multi-spacecraft approach is shown in the second panel. The single-spacecraft approach for $\tau = 0.015s$, $0.15s$, $0.45s$ and $1.5s$ is shown on panels 3 to 6.

The two methods are in good agreement when the appropriate value τ is selected. Firstly, for $\tau = 0.015s$ the single-spacecraft method gives lower values of θ. As we increase τ, the values of the PVI increase. The peak reaches a plateau and becomes wider for further increase of τ. The best agreement is found for $\tau = 0.45$. This time delay corresponds to the separation between the spacecraft, given that the velocity of this current sheet is $\sim 200km/s$. This agreement is further confirmed when considering all current sheets detected by the PVI for this event, as shown in Figure 5.5 where the best match is obtained for $\tau = 0.45s$. In the scatter plot there are, however, variations due to the fact that the single spacecraft approach includes assumptions about the velocity and the thickness of the structure. This analysis indicates that for a given spatial scale, that is comparable with the spacecraft separation, the multi-spacecraft PVI provides a more accurate way to detect current sheet than the single spacecraft, since no assumption on the current sheet velocity is needed and there is a smaller risk of underestimation due to an improper choice of τ, which is the case for the single spacecraft approach. For this particular study, the multi-spacecraft PVI is suitable for studying current sheet at proton scales since the inter-spacecraft separation is $\sim 100km$ which is comparable to the proton gyroradius/inertial length. The disadvantage of such multi-spacecraft approach is of course that only a limited range of spatial scales

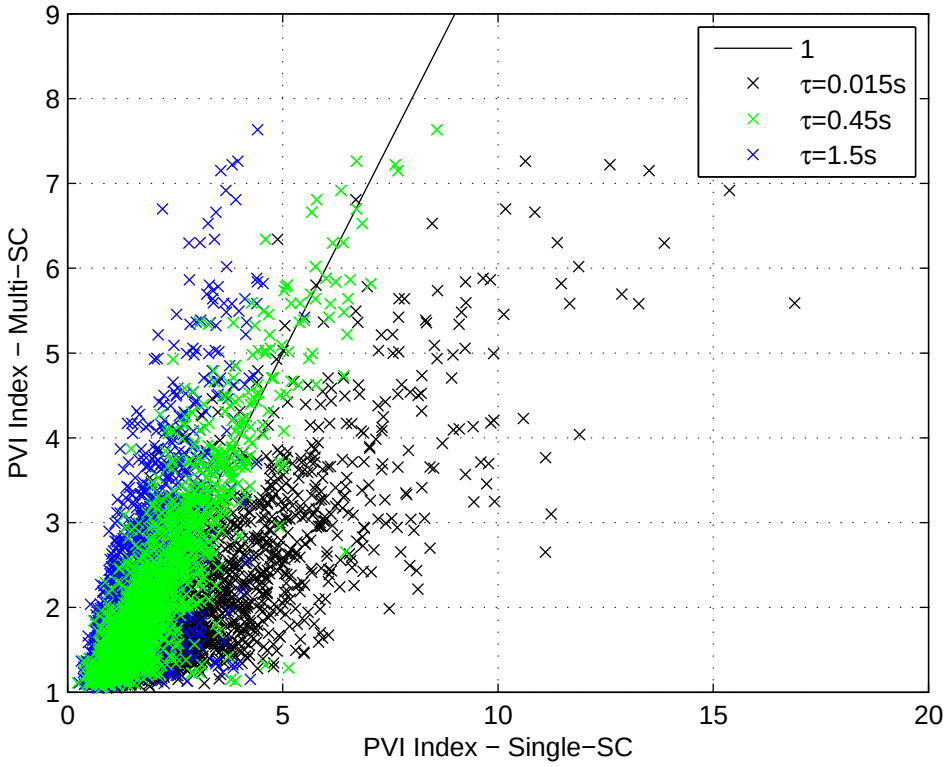

FIGURE 5.5: Comparison between multi-spacecraft and single-spacecraft methods for calculating the PVI index. Each point represents one current sheet. The maximum PVI index for the multi-spacecraft approach is on the horizontal axis. The maximum for the single-spacecraft approach is on the vertical axis. Black points represent the results for $\tau = 0.015s$, green points for $\tau = 0.45s$ and blue points for $\tau = 1.5s$. The black line has a slope of 1 and corresponds to the best agreement between the two methods obtained for is for $\tau = 0.45s$. Interval of $1h30'$ in the Earth's magnetosheath of Full resolution Magnetic field data $(67Hz)$in GSE coordinates provided by the Cluster Science Archive.

can be investigated at a time. In particular, electron scales where important dissipation is expected to occur, cannot be sampled by Cluster but recently available NASA/MMS spacecraft data would be used for this purpose.

As for the PVI, a multi-spacecraft calculation of the magnetic shear angle has been implemented in this work. The angle was measured between each pair of spacecraft as was done for the PVI index to get:

$$\theta_{ij}(t) = cos^{-1} \frac{\vec{B}_i(t) \cdot \vec{B}_j(t)}{|\vec{B}_i(t)| \cdot |\vec{B}_j(t)|} \tag{5.3}$$

where i and j denote each pair of the 4 Cluster spacecraft.

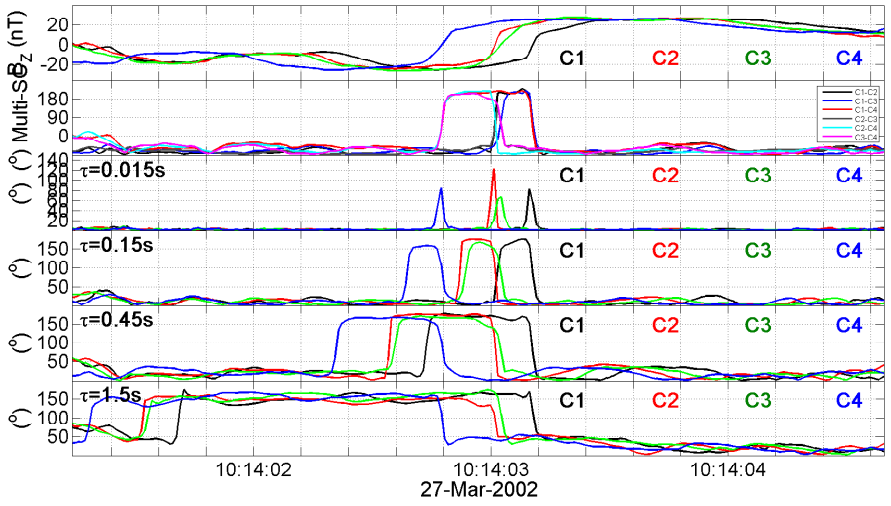

FIGURE 5.6: Magnetic shear angle during the crossing of a current sheet detected in the Earth's magnetosheath. The multi-spacecraft approach is shown in the second panel. The single-spacecraft approach for $\tau = 0.015s$, $0.15s$, $0.45s$ and $1.5s$ is shown on panels 3 to 6. Full resolution Magnetic field data ($67Hz$)in GSE coordinates provided by the Cluster Science Archive.

A comparison of the results of the magnetic shear angle analysis between single and multi-spacecraft approach is shown for the same current sheet in Figure 5.6 for different values of time delay τ. The conclusions that can be drawn are similar as for the PVI above. The observed peak of shear angle in Fig. 5.6 reaches a maximum and then starts to become broader as the time delay increases. Once more, the results of the two methods agree when the chosen time delay is set to $\tau = 0.45s$. In figure 5.7 we see the same rough agreement for the entire population of the current sheets, with the two methods converging for $\tau \sim 0.45s$ as expected. For lower values of τ the single spacecraft method underestimates the shear angle whereas for higher values of τ it tends to saturate towards 180^o. For the same reasons as for the PVI, for a given spatial scale the multi-spacecraft shear angle method is more reliable than the single spacecraft one.

Both multi-spacecraft PVI and magnetic shear angle methods could be in principle used to detect current sheets in the event studied here, as they both select regions of strong current. However, the shear angle method can select by definition only changes in magnetic field orientation (rotation) while the PVI is sensitive to variations of both orientation and amplitude of the magnetic field. It should be noted that, following Ampere's law $\mu_0 \vec{J} = \nabla \times \vec{B}$, a rotation of the magnetic field corresponds to the component of the current parallel to the magnetic field

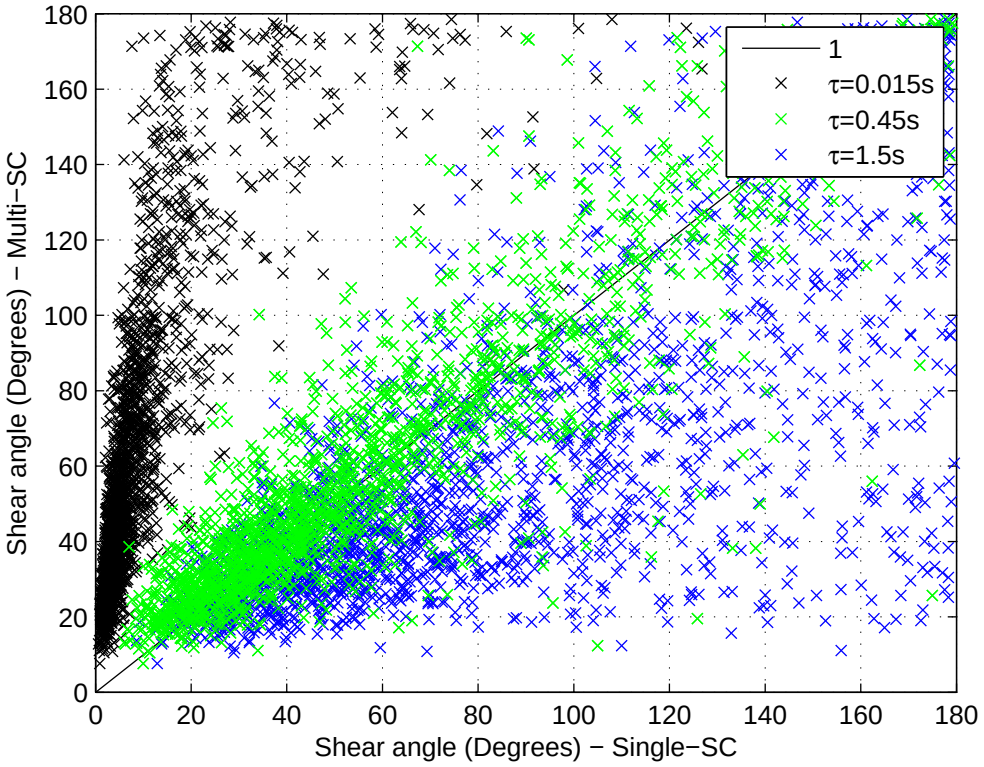

FIGURE 5.7: Comparison between multi-spacecraft and single-spacecraft methods for calculating the magnetic shear angle. Each point represents one current sheet. The maximum shear angle for the multi-spacecraft approach is on the horizontal axis. The maximum for the single-spacecraft approach is on the vertical axis. Black points represent the results for $\tau = 0.015s$, green points for $\tau = 0.45s$ and blue points for $\tau = 1.5s$. The black line has a slope of 1 and corresponds to the best agreement between the two methods obtained for is for $\tau = 0.45s$. Interval of $1h30'$ of in the Earth's magnetosheath. Full resolution Magnetic field data $(67Hz)$in GSE coordinates provided by the Cluster Science Archive.

while a change in the amplitude of the magnetic field corresponds to a perpendicular current. To illustrate that point, we can consider the magnetic field in a cylindrical reference frame ρ, ϕ, z, where the magnetic field vector is parallel to the (ρ, ϕ) plane and varies along the z axis. In such a frame, $B_z = 0$ and the only non-zero derivative is $\frac{\partial}{\partial z}$. Then the expression for $\nabla \times \vec{B}$ can be written as $\nabla \times \vec{B} = -\frac{\partial B_\phi}{\partial z}\hat{\rho} + \frac{\partial B_\rho}{\partial z}\hat{\phi}$. Therefore the magnetic shear can provide informations only on the parallel component of the current, while perpendicular currents are important as well to identify current sheets. While using the magnetic shear angle could be appropriate in the pristine solar wind as done earlier [97, 161], this is not necessarily the case in regions of strong compressions and gradients such as the shock and the magnetosheath, where at least a fraction of current sheets are

expected to be associated with perpendicular currents. In general, relying solely on the magnetic shear angle as a method to detect discontinuities in turbulent plasma may bias the sample by discounting such structures. For these reasons, the multi-spacecraft PVI is more suitable than multi-spacecraft shear angle to identify current sheets in this event and the former was preferred for this study. To further illustrate this aspect, Figure 5.8 shows the multi-spacecraft PVI index and the multi-spacecraft magnetic shear angle of current sheets detected in this event for $PVI > 1$ during an interval of $1h30'$. It can be seen that high PVI current sheets are usually characterized by relatively large rotation angles ($> 90^o$). The low PVI current sheets, on the other hand, have a wide range of values for the magnetic shear angle, that cover essentially all possible angles. However they are not evenly distributed, with the overwhelming majority having relatively small rotation angles ($< 90^o$). In particular, not all regions of strong current have a high magnetic shear angle. There is a substantial number of cases with relatively high PVI $\sim 1-3$ but low shear angle $< 50^0$ for which the current is mostly perpendicular. Such current sheets could be asymmetric current sheet with a strong guide field or small-scale shocks.

As discussed above, the PVI is basically proportional to the total current density. A comparison between the magnitude of the current estimated using the curlometer and the multi-spacecraft PVI index for the current sheets detected in this event, is shown in Figure 5.9. Not surprisingly, the correlation between the two quantities is quite good suggesting that the curlometer itself could be used as a current sheet detection method. However, as discussed in Section 4.1.3 and shown in Fig. 4.3, the curlometer tends to underestimate the current when the scale of the current sheet is smaller than the spacecraft separation, since the measured current is an average over the tetrahedron. Therefore for the purpose of detecting thin current sheets in turbulence the curlometer technique is not optimal, unless having events with a tetrahedron with smaller separation than for this event. This is not possible for Cluster since the smallest separation for the tetrahedron is ~ 100 km, but it will be possible with MMS since the separation in the magnetosheath would be ~ 10 km.

An example of a crossing of one current sheet and the resulting increase of PVI index, shear angle and current from curlometer is shown Figure 5.10. The reversal of the z-component (figure 5.10a,b) indicates when each spacecraft crosses the boundary. Figure 5.10c shows the shear angle between each pair of spacecraft.

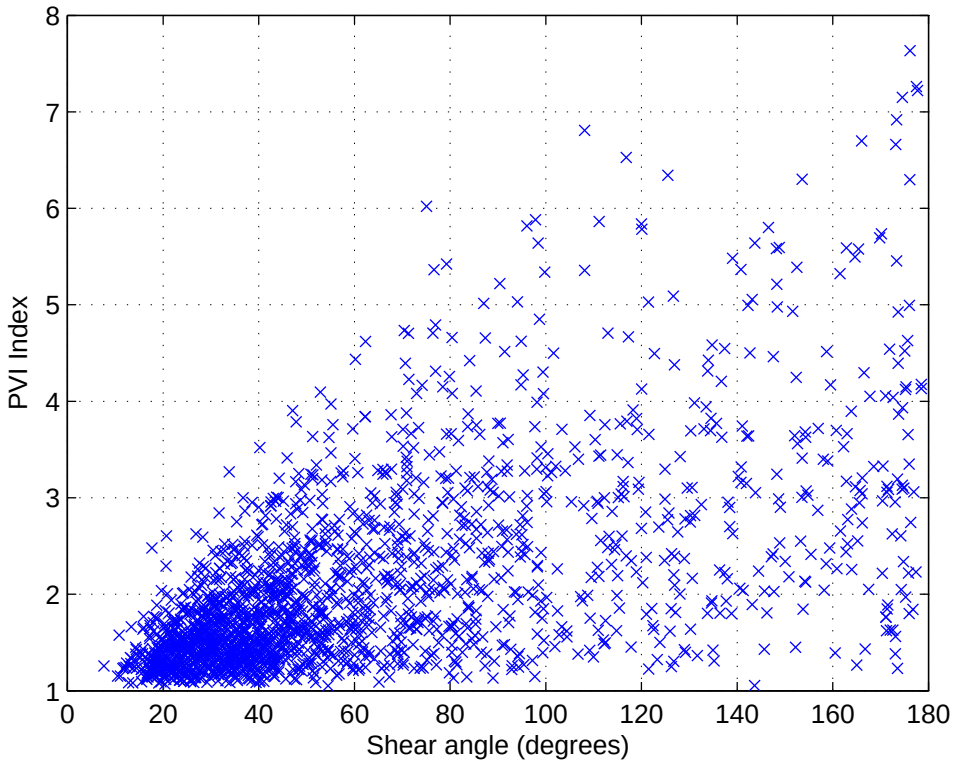

FIGURE 5.8: PVI index and magnetic shear angle of each of the detected current sheets in the interval of of $1h30'$ in the Earth's magnetosheath downstream of the quasi-parallel shock.

The PVI index is shown in Figure 5.10d and exhibits a peak similar to the one of the shear angle. This is expected since this current sheet is characterised by a large rotation but small change of the overall field strength. For such a case, the two methods yield similar results for the detection. Figure 5.10e shows the current estimated by the curlometer, which shows a similar peak as the PVI and the shear angle since in this case the current sheet thickness is comparable with the inter-spacecraft separation. Yet for other cases when the current sheet is thinner (not shown here), the curlometer current does not show very large variations compared to the background. Figure 5.10f shows the estimated electron temperature. The four spacecraft measure an enhancement of the electron temperature within the current sheet. This current sheet is examined in more detail in section 5.2.

Once having tested the different methods and concluded that the multi-spacecraft PVI is the most suitable method for this study, the final step is to define the appropriate thresholds in the PVI method to select the current sheets. The detection of structures using the PVI is done by setting a threshold value and selecting the

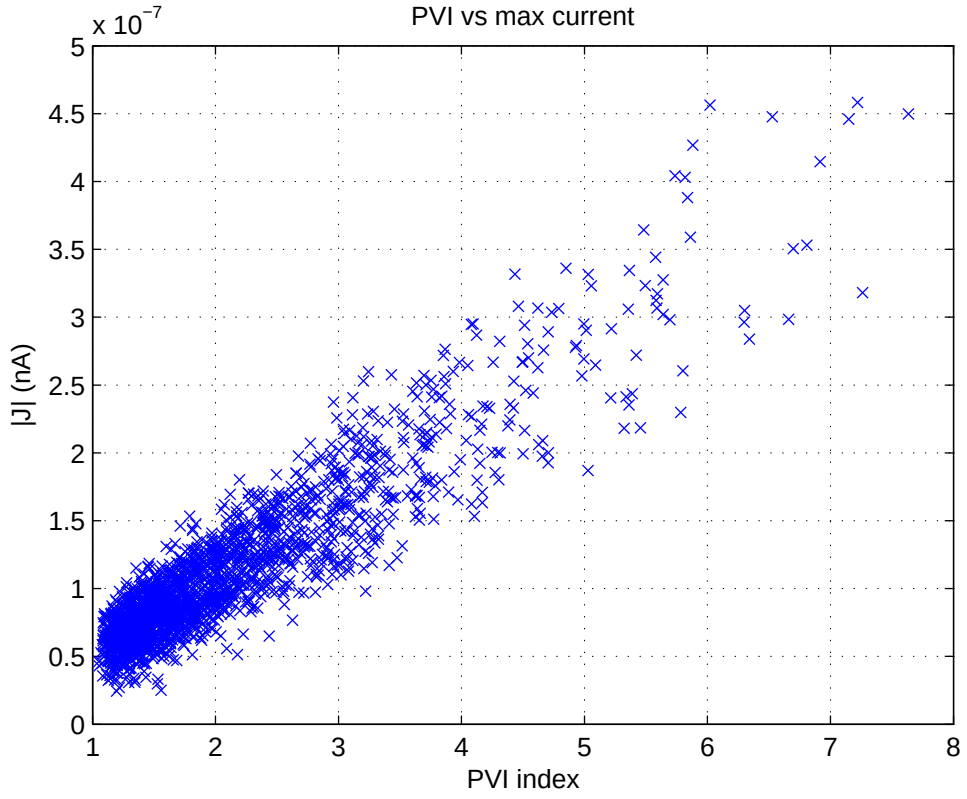

FIGURE 5.9: PVI index and the maximum magnitude of the current estimated using the curlometer technique. Each point represents one current sheets detected in the Earth's magnetosheath downstream of the quasi-parallel shock. Interval of $1h30'$ from 27th of March 2002.

peaks that are above that value [47, 48, 135]. Specifically, I have set the condition to $PVI_{ij} > PVI_{threshold}$ in equations 5.1 and 5.2 for at least one pair of spacecraft (i, j), and selected the portions of the time series that satisfy this condition. This way we select intervals of the time series that begin when the PVI value rises above the set threshold and end when it falls below it. Those intervals where the value of the PVI is above the threshold, are selected as current sheets. The maximum value during each interval is chosen as the PVI index of that specific current sheet. In order to assure that we are limited to proton-scale current sheets one more condition was imposed on the duration of the structures. A limit was set on the duration of the structures choosing the ones which last between $0.25s$ and $8s$. This time-scale corresponds to the proton gyroradius $(100-200km)$, divided by the typical velocities in the magnetosheath, which are in the range of $50 - 400kms^{-1}$. The choice of the specific value for the threshold $PVI_{threshold}$ was done by using results from past studies. Specifically, studies that have investigated the PVI

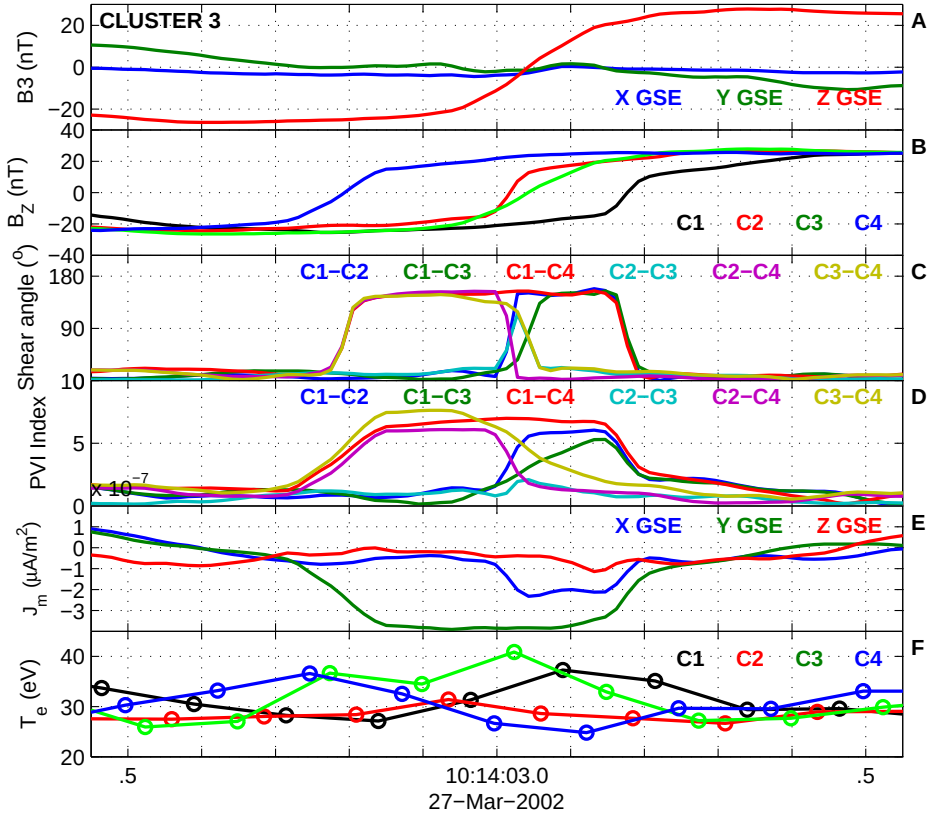

FIGURE 5.10: Example of a detected current sheet. Panel A shows the magnetic field measured by Cluster 3. Panel B shows the z-component in GSE coordinates for the four spacecraft. Panels C, D show the shear angle, PVI index for each pair of spacecraft computed through multi-spacecraft method. Panel E shows the current from the curlometer. Panel F shows the estimated electron temperature for each spacecraft.

technique using numerical simulations and observations have suggested an association between different values of the PVI index and different types of intermittent structures [47, 48, 104]. It was found that peaks of the PVI index correspond to intermittent structures that form in turbulence, with the stronger peaks having a higher probability to be associated with current sheets. According to this categorization, values of the PVI below $PVI < 1$ correspond to low-amplitude Gaussian fluctuations. Intermediate values $1 < PVI < 3$ correspond to structures such as magnetic islands and vortices. High values ($PVI > 3$) are associated to small-scale current sheets. The relevant numerical simulations by [48] are shown in Figure 5.11, where we observe how these different values correspond to regions that contain the corresponding types of structures. The same threshold values of the PVI index were used for this work and in [17].

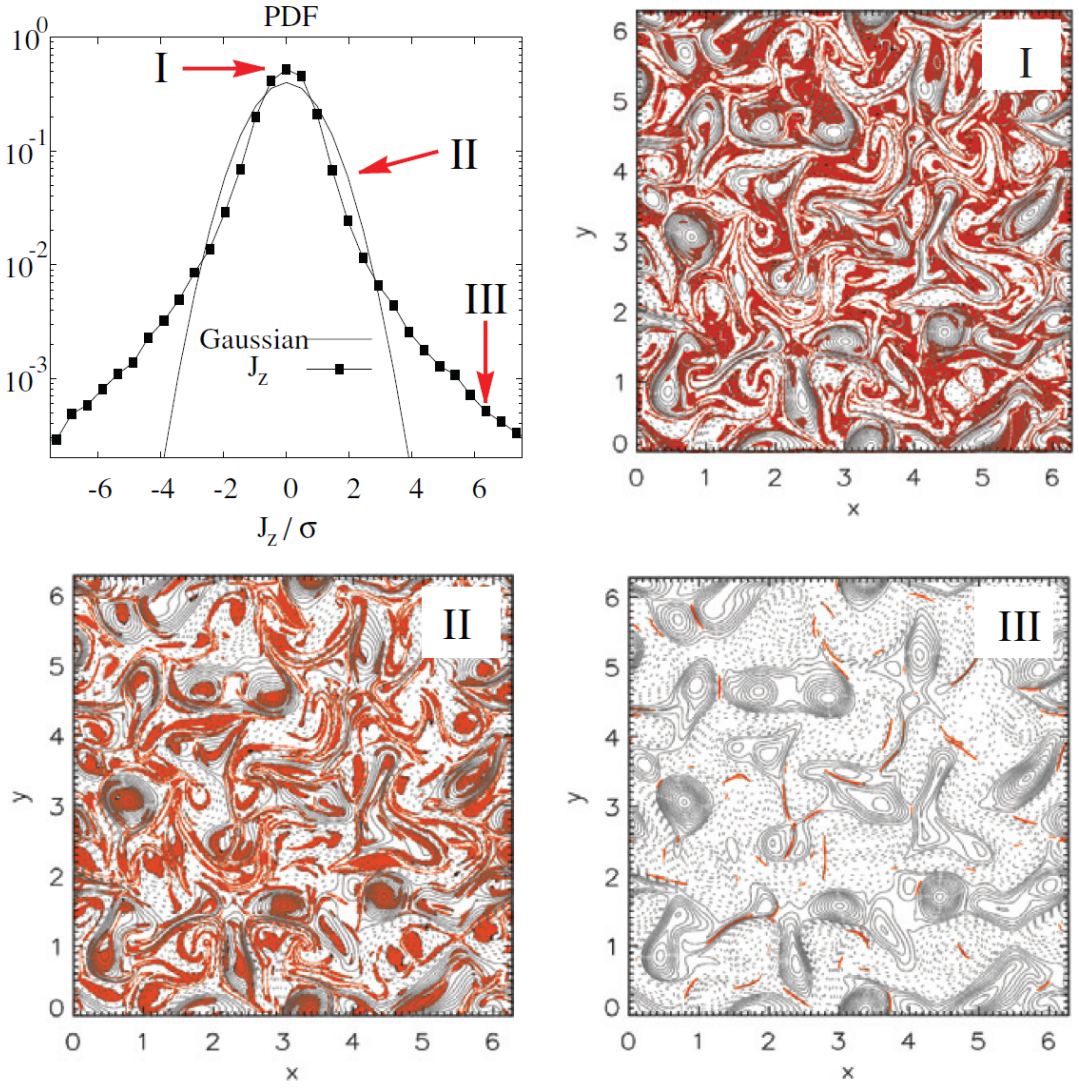

FIGURE 5.11: Results by [48] using a Hall-MHD simulation. Probability Distribution of the out-of-plane electric current density J_z from the simulation, compared to a reference Gaussian. Three regions were identified by and are marked in the plot. A super-Gaussian core (region I), a sub-Gaussian midsection (region II), and super-Gaussian tails (region III). For each region I, II, and III, magnetic field lines are shown. The colored red regions correspond to the selected band (I, II, or III) of the distribution. Adapted from [48].

PVI index	% of reconnecting current sheets
> 1	9.8%
> 2	23.0%
> 3	34.8%
> 4	43.7%
> 5	57.5%
> 6	72.0%
> 7	93.7%
> 8	100%

TABLE 5.1: Percentage of current sheets that are reconnecting with respect to the value of the PVI index. Results from numerical simulations by [135].

It must be also noted that numerical simulations by [135] have demonstrated that the likelihood of reconnection within current sheets increases for higher values of the PVI index. The correlation between the PVI index and the likelihood of reconnection are shown in table 5.1. Recent observations of turbulent reconnection in the solar wind seem to qualitatively verify this conclusion [105].

5.1.2 Properties of current sheets

After having established a robust method for the detection of current sheets, I have compiled a list of about 1800 current sheets for this event through the multi-spacecraft PVI method. By using this list, I examined some of the current sheet properties in order to understand how they relate to the overall properties of the turbulence in the quasi-parallel magnetosheath. Although similar observations have been carried out in the pristine solar wind [48, 97, 104, 105], this is the first detailed study of thin current sheets in the Earth's magnetosheath and therefore most of the available literature to compare to refers to studies in the pristine solar wind.

The first step was to look into the distribution of the detected current sheets as a function of the PVI index and of the magnetic shear angle. Such distribution could provide important information about the formation mechanisms of the current sheets, as suggested by earlier studies in the pristine solar wind [11, 97]. Observations by Miao et al. [97] found two distinct populations with high and low magnetic shear angles (shown in Figure 5.12), which have been interpreted as produced by two different physical mechanisms, with the low shear structures being

formed locally in the turbulence and the high shear ones being flux tube boundaries that originate in the solar corona and are convected across the interplanetary space [10]. Regarding the event studied here, the distribution of the current sheets with respect to their shear angle is shown in figure 5.13 for different values of the PVI threshold. We observe two distinct populations. One comprises the bulk of the overall population ($\sim 85\%$) with low PVI ($1 < PVI < 3$) and mostly low magnetic shear angles. A second, smaller population of high PVI ($3 < PVI < 5$) index with relatively large shear angles. Finally, the few cases with a very high PVI ($PVI > 5$) have shear angles larger than $\sim 90^o$. The distribution of the number of current sheets relative to the magnetic shear angle appears similar to the one found by [97]. As was the case for the current sheets in that study, the existence of the two populations in our data points to different formation mechanisms. Following that line of thought, it can be argued that the first population detected in this event, consisting of structures with low shear and low PVI index, is generated locally in the turbulence of the magnetosheath. The second population, which is much smaller and consists of high shear-high PVI index cases, could be created by compression at the bow-shock and convected downstream or originate in the pristine solar wind and then convected across the shock down to the magnetosheath. It has not been possible, however, to differentiate between such mechanisms and further analysis is needed to clarify this aspect.

The next step was to study the waiting time, which is defined as the time interval between two consecutive current sheets. The waiting time gives important information about the spatial distribution of current sheets within the turbulence, for example on the filling factor that is the fraction of the volume that consists of current sheets. As demonstrated by recent kinetic simulations of turbulence [156, 157], strong intermittency at kinetic scales due to current sheet formation lead to strong heating and dissipation that is highly patchy. Understanding and quantifying the filling factor from experimental point of view is very important to quantify heating and dissipation, as attempted for the same event discussed here by [141]. Additionally, the waiting time distribution, along with the distribution of the magnetic shear angle, can provide information about the formation mechanism of the current sheets, e.g. if they are formed spontaneously in the turbulence or by some other mechanism. In the case of the pristine solar wind, the survey by [97] has found that the two different populations mentioned in the previous section follow two distinct distributions, with the low shear population following an exponential decay and is thought to be locally generated, whereas the high shear

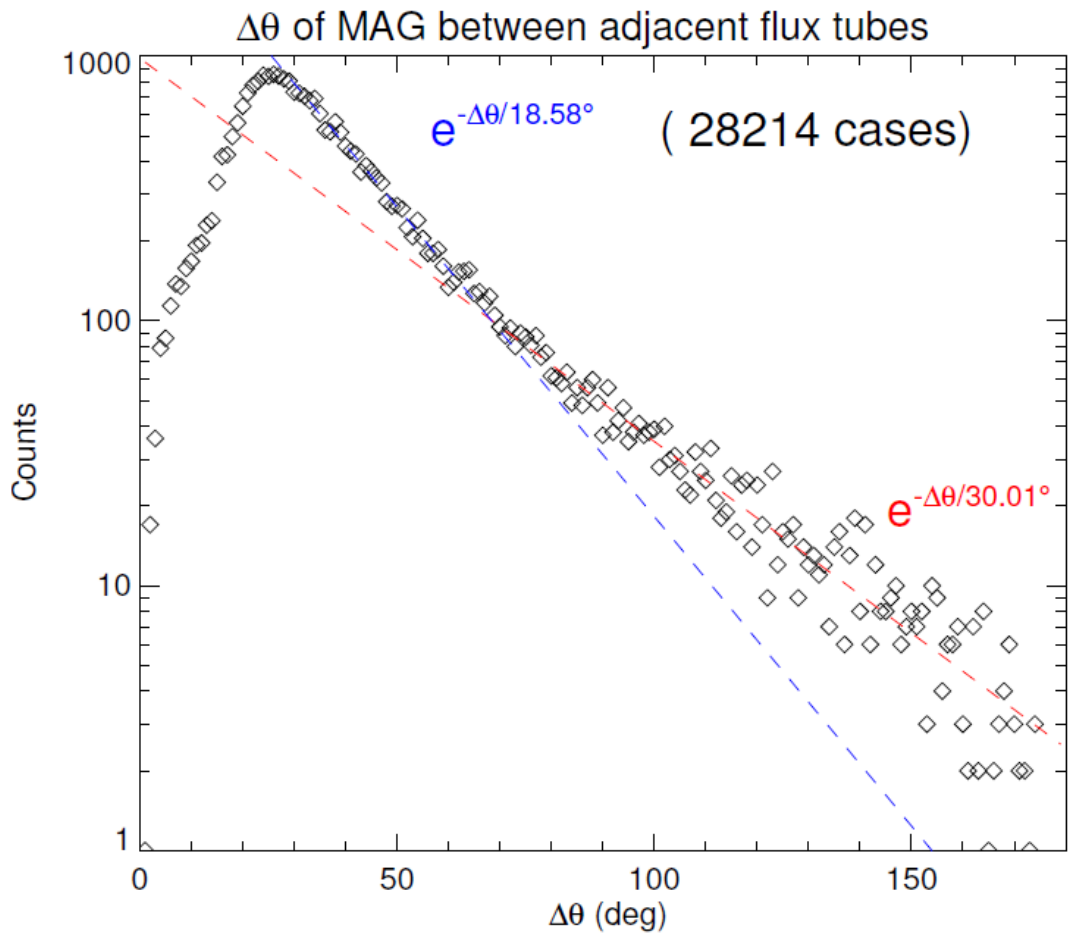

FIGURE 5.12: Distribution of the number of current sheets with respect to the measured magnetic shear angle, detected in the solar wind. From [97]

current sheets follow a power-law distribution and are thought to originate in the solar corona (see Figure 5.14). For the current sheets studied in this event, the distribution of the waiting time is shown in Figure 5.15. The sample size of the distribution shown in this figure is small. Therefore, it is not possible to identify the two populations discussed in the previous paragraph, as well as determining any scaling of the distribution. One significant difference, however, is that the average time is much smaller in the data presented in this work compared to [97], which suggests that thin current sheets are more abundant in the quasi-parallel magnetosheath compared to the pristine solar wind.

Finally, I have studied the spatial distribution of the current sheets with respect to the distance from the bow shock, in order to examine how the turbulence in the quasi-parallel magnetosheath is influenced by the bow-shock itself and evolve as function of the distance from the shock. A previous study by [159] has shown that

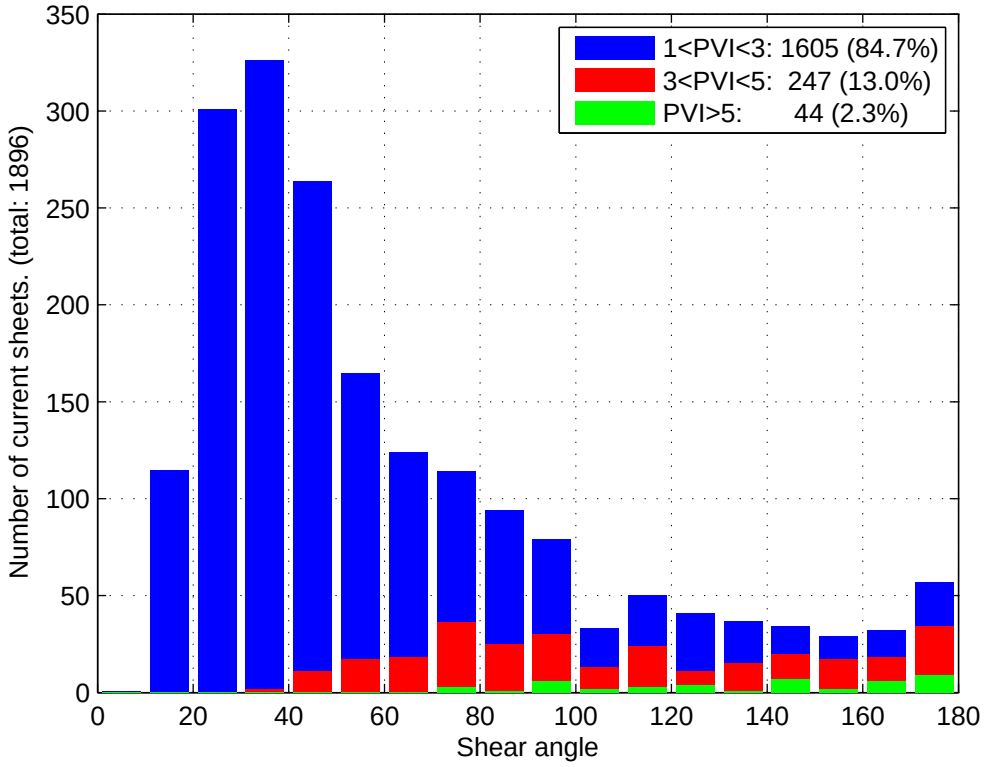

FIGURE 5.13: Distribution of the detected current sheets as a function of the magnetic shear angle. Each color represents a different value of the PVI threshold. The total number of detected current sheets is 1896.

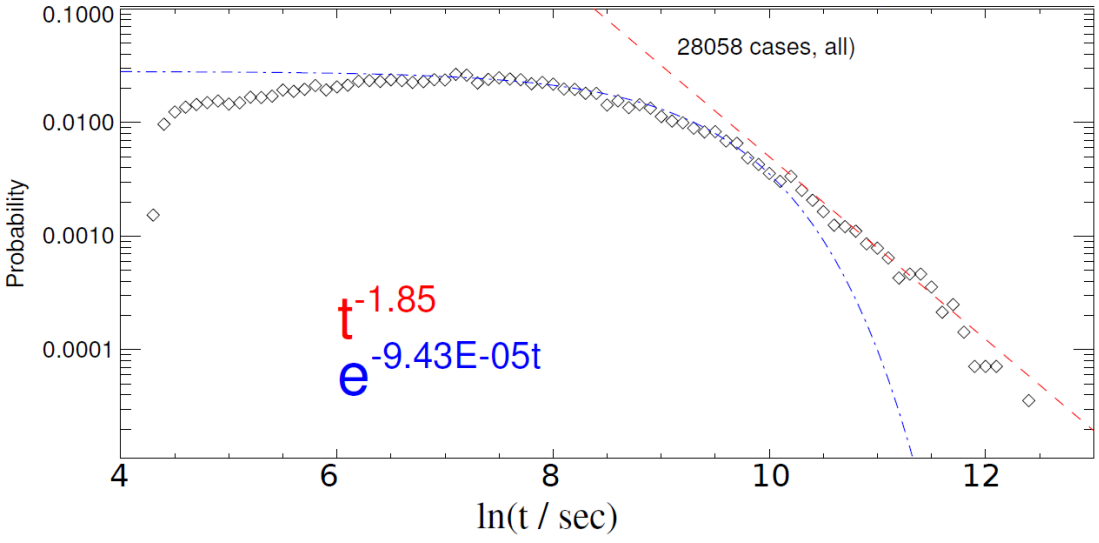

FIGURE 5.14: Distribution of waiting time between current sheets detected in the solar wind. From [97]

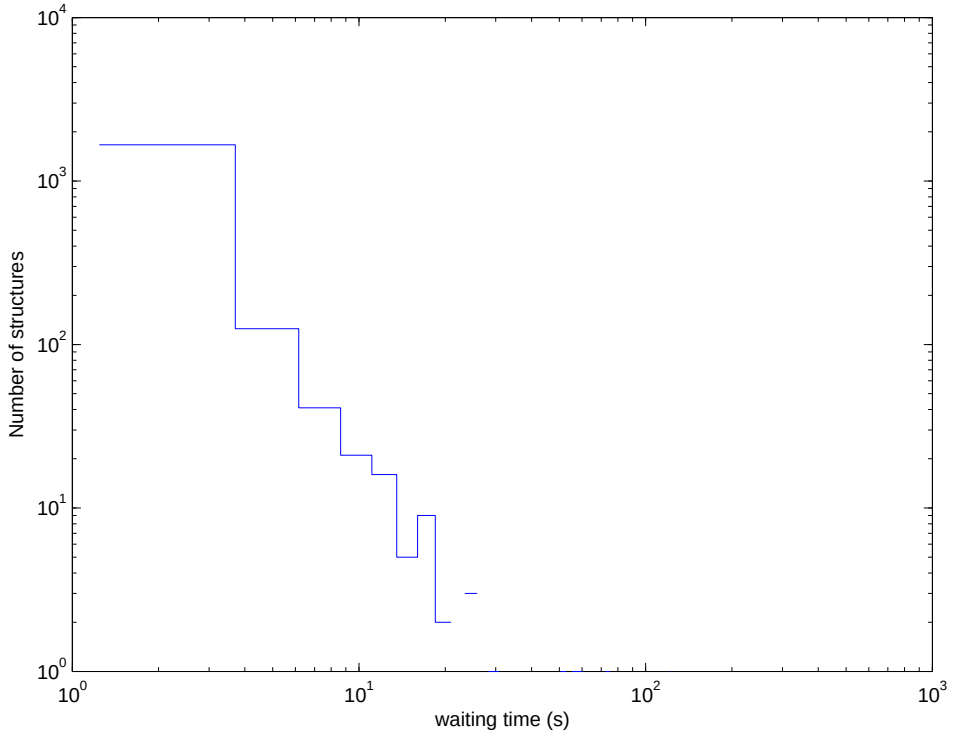

FIGURE 5.15: Distribution of the waiting time between each detected current sheet. Interval of $1h30'$ in the Earth's magneotsheath, downstream of the quasi-parallel shock.

the intermittency, which is associated with the presence of coherent structures such as current sheets, increases with distance from the shock.

In order to compare with Yordanova et al. [159], I separated the event into intervals of 12.5 minutes and computed the distribution of the high and low PVI populations across each interval, which is shown in Figure 5.16. The time corresponds to increased distance from the shock since the spacecraft travel downstream and away from the shock. We note that the high PVI structures are detected mostly close to the shock with their numbers decreasing as we move downstream, whereas low PVI structures are distributed evenly across all intervals. This result could be interpreted as evidence that intermittency decreases away from the shock, in contradiction with the results presented in [159]. However, there are few caveats to such a conclusion. First, the shock is not a stationary boundary especially for the quasi-parallel case therefore the position of the shock boundary may change substantially during the event. Also, the low velocity of the spacecraft ($v_{sc} \sim 1km/s$) means that in the one and a half hour of the duration of this event, they travel a relatively short distance and remain still in close proximity to the bow shock,

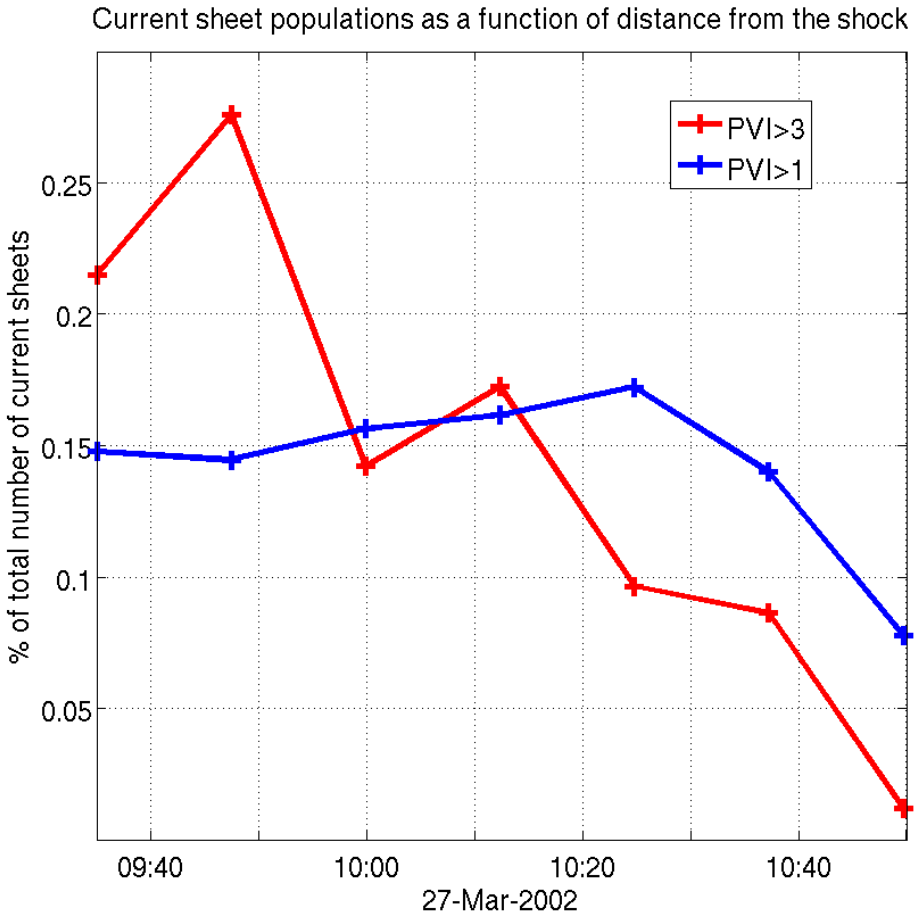

FIGURE 5.16: Distribution of the detected current sheets as a function of the time for the high and low PVI population. The spacecraft cross the bow-shock at approximately $9h35$ and head downstream, towards the magnetopause.

while [159] examined the evolution of intermittency at a much larger distance from the bow shock. Finally, the shock changes from quasi-parallel to quasi-perpendicular shortly after (around $11h30$). The magnetosheath downstream of the quasi-perpendicular shock is characterized by lower levels of intermittency compared to the quasi-parallel case [63]. This means that the observed decrease of the high PVI population could be due to a gradual change of the configuration from quasi-parallel to quasi-perpendicular.

5.1.3 Electron heating

As discussed in Chapter 1, a key problem is to understand how energy is dissipated at kinetic scales in turbulence and how charged particles are heated. Many theoretical and simulation studies suggest that such dissipation and heating is

highly non-uniform and concentrated in coherent structures resulting from the intermittent behavior of the turbulence. In particular, recent kinetic simulations [13, 61, 63, 156, 157] have shown that dissipation and electron heating occur in thin current sheets and suggested that turbulent magnetic reconnection is the dominant dissipation mechanism. A few observational studies suggesting that turbulent reconnection leads to efficient dissipation and heating have been reported [104, 105]. However, in such statistics the association to kinetic scales could not be done due to limitation in the time resolution of measurements. The study done in this thesis is the first statistical analysis of current sheets in turbulence at kinetic scales. Apart from studying the general properties of current sheets in turbulence, the current sheet list obtained in this study has been used to test energy dissipation in the form of electron heating within the current sheet. The results of this study are reported in [17] (see Appendix A) and discussed in this section. The direct link between electron heating and turbulent reconnection could not be established in this study due to limitations of Cluster data, namely the time resolution of plasma data which are necessary to identify, for example, reconnection jets. However, such link has been verified for a few current sheets, as discussed later in Section 5.2.

Despite the many limitations of Cluster data, the detailed study of the electron heating within thin current sheets has been possible thanks to a few specific conditions. First, during the event the PEACE instrument was operating in Burst Mode which allowed to have continuous measurements of the proxy of the electron temperature at sub-spin time resolution, as discussed in Section 4.3. This time resolution $125ms$ has been crucial to resolve the temperature variations across the current sheets. Furthermore the properties of the electrons downstream of the shock into the magnetosheath allow for a robust estimation of electron temperature. High fluxes correspond to higher particle counts over a wide range of energies even at sub-spin time resolution, so that one does not have issues related to count statistics. Also, the average electron temperature is well above the energy corresponding to the spacecraft potential, reducing the impact of contamination from photoelectrons and leading to a better sampling of the thermal part of the distribution. Finally as electrons flow past the shock they become less anisotropic compared to the pristine solar wind. This increases the reliability of estimating the temperature from partial sub-spin distributions since for that estimation the core of the distribution function is assumed to be isotropic.

Using these data, we were able for the first time to investigate the electron heating

within proton-scale current sheets in turbulence. This was done by computing the local increase of the proxy of the electron temperature within each structure. For each current sheet we calculated the maximum and the median electron temperature within the current sheet, observed by each spacecraft. The local heating was estimated for each case by subtracting the maximum electron temperature from the median, for each spacecraft. The values of the electron heating in each current sheet, as measured for each spacecraft are shown in figure 5.17. The standard deviation of the electron temperature during this event is $6eV$ (marked with a dashed red line in figure 5.17), and can be used to compare the increase of the temperature expected due to random fluctuations to actual local heating within the current sheet. It must be noted that, on average, the four individual estimations from each spacecraft showed a similar profile. However, there are deviations due to the fact that different spacecraft may cross different parts of the structure and therefore observe different values of the electron temperature. In order to obtain a single, more robust estimation of the heating, the four estimations were averaged to yield the final value within each detected structure, which is shown in Figure 5.18.

Figure 5.18A shows local increase in the estimated electron temperature for each detected current sheet as a function of their PVI index. Figure 5.18B shows normalized histograms of ΔT_e for different intervals of the PVI value. Most of the structures with low PVI ($1 < PVI < 3$) show a small increase of the electron temperature. Most of the structures with high PVI ($PVI > 3$), however, exhibit a significantly larger increase, indicating substantial electron heating in those structures. The observed heating corresponds to an increase up to ~ 0.5 times the background temperature. This is shown in more detail in Table 2. For $\sim 90\%$ of the low PVI population, the temperature increase is below 1σ. Most of the high PVI structures show a temperature increase between $1\sigma_{T_e}$ and $3\sigma_{T_e}$, with a small percentage being above 3σ. This trend becomes even more significant for the structures with very high PVI index ($PVI > 5$), where $\sim 80\%$ have $\Delta T_e > 1\sigma$ and $\sim 10\%$ are above $3\sigma_{T_e}$. Such high PVI structures have been associated with an increased probability to be sites of magnetic reconnection in numerical and recent observational studies [105, 135], as discussed in Section 5.1.1 and shown in and table 5.1. We also note that significant heating is observed in a few low PVI cases. These results demonstrate for the first time that significant electron heating occurs within thin current sheets in turbulence, and indicates their importance for the dissipation of energy at kinetic scales.

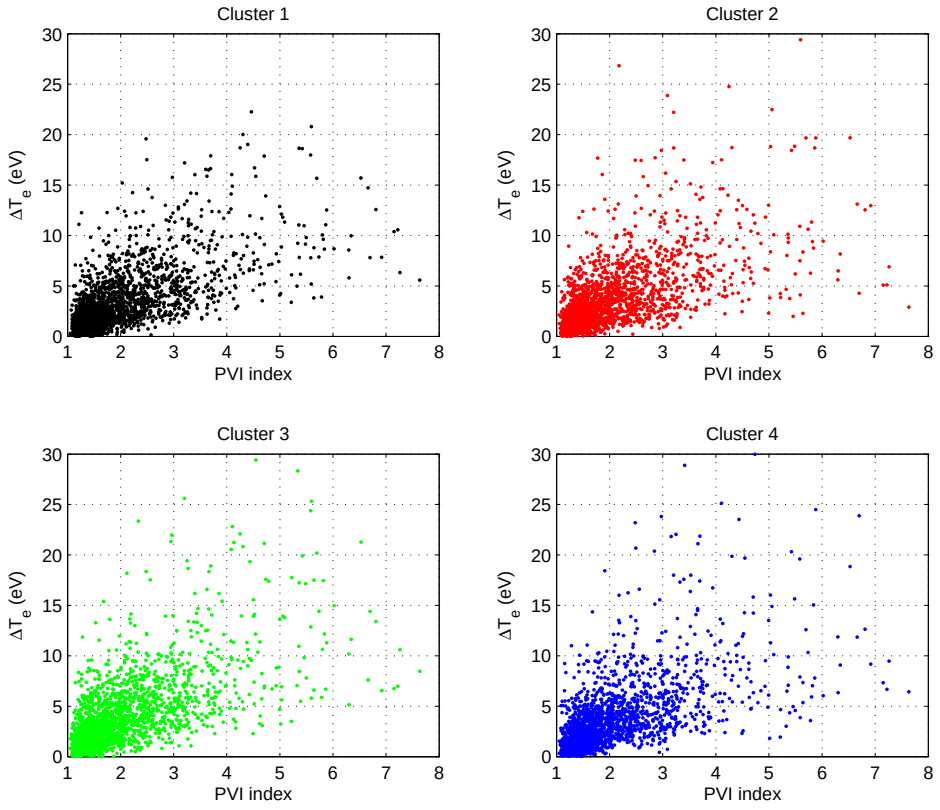

FIGURE 5.17: Local increase of the electron temperature observed by each spacecraft and corresponding PVI index for each of the detected structures.

PVI	$\Delta T < 1\sigma$	$1\sigma < \Delta T < 2\sigma$	$2\sigma < \Delta T < 3\sigma$	$\Delta T > 3\sigma$	Total
Low ($PVI < 3$)	90.7 %	8.7 %	0.5 %	0.1 %	100.0 %
High ($3 < PVI < 5$)	43.3 %	43.7 %	9.3 %	3.7 %	100.0 %
Very High ($PVI > 5$)	20.4 %	52.3 %	18.2 %	9.1 %	100.0 %

TABLE 5.2: Percentage distribution of the electron heating for structures with different PVI values.

5.1.4 Energy partition

A final aspect that I attempted to investigate was how the observed electron heating is related to the total amount of magnetic field energy dissipated within the current sheets. This requires the knowledge of the specific dissipation mechanism, which was not possible to determine in this study. Turbulent reconnection is very likely to be the actual dissipation mechanism for high PVI current sheets, however for lower PVI current sheets other dissipation mechanisms such as small-scale

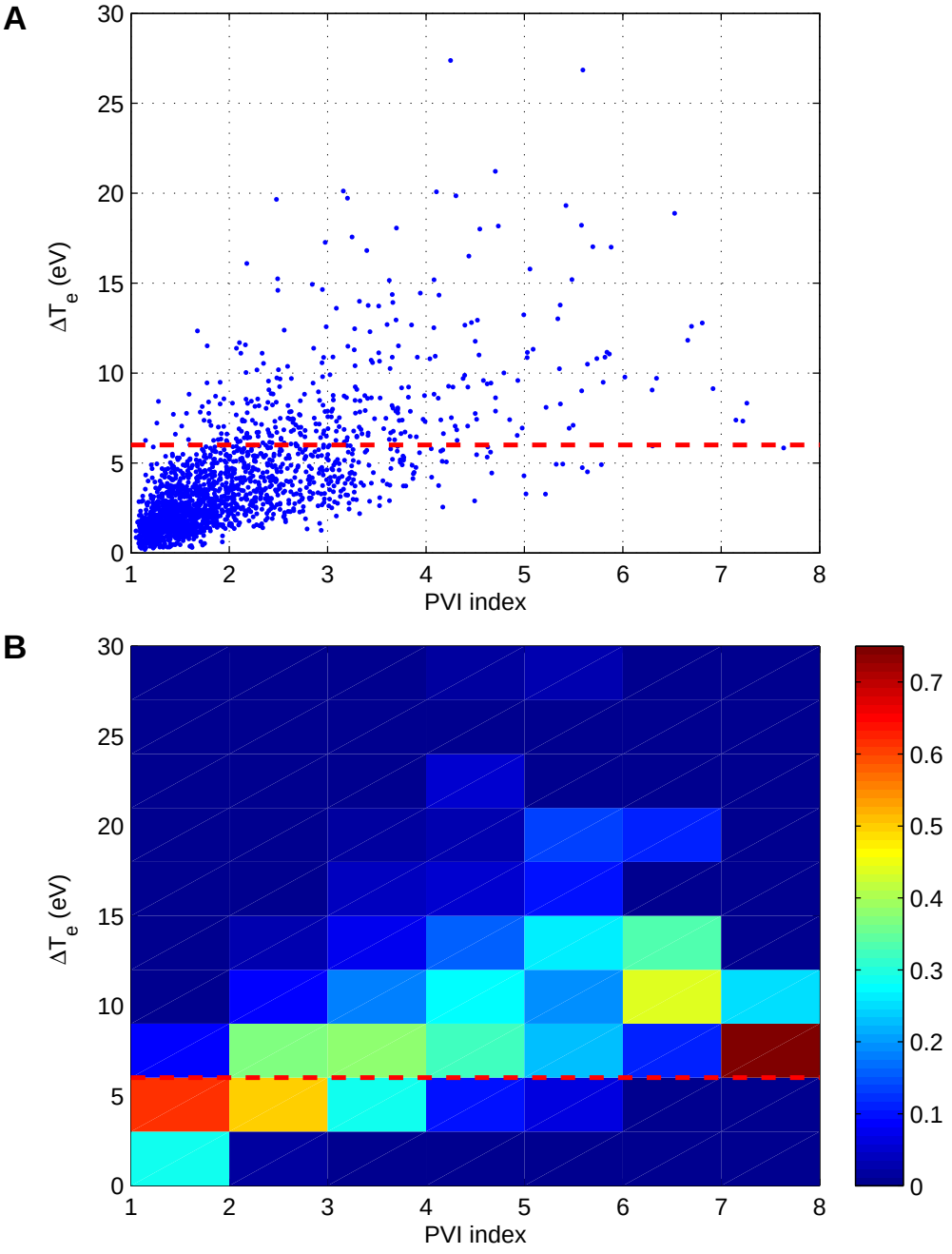

FIGURE 5.18: Local increase of the electron temperature and corresponding PVI index for each of the detected structures. Panel A: Scatter plot of the values for each detected current sheet. Panel B: Normalized histograms are shown along the y-axis for each slice of PVI index values. The dashed red line in both plots denotes the $1\sigma_{T_e}$ level for the estimated electron temperature during the whole interval.

shocks or wave-particle interaction could also be important. Therefore here I only attempted to compare with earlier literature for the case of magnetic reconnection.

Recent observations of reconnection at the magnetopause by [114] have indicated that the electron bulk heating is linearly proportional to the inflowing magnetic energy. They have demonstrated an empirical relation regarding the amount of magnetic field energy that is converted to electron heating. That relation was $\Delta T_e = 0.017 m_i V_{A,assym}^2$, where $V_{A,assym}$ is defined by [14] as the asymmetric Àlfven velocity and is equal to $V_{A,assym} = [B_{L,sh}B_{L,sph}(B_{L,sh}+B_{L,sph})/0(_{sh}B_{L,sph}+_{sph}B_{L,sh})]^0.5$. The empirical equation $\Delta T_e = 0.017 m_i V_{A,assym}^2$ indicates that $\sim 1.7\%$ of the magnetic energy is converted into electron bulk heating. The observations of this scaling by [114] are shown in Figure 5.19. Recent kinetic simulations by [136] also postulated that this finding is applicable in general to symmetric reconnection, while the results by [114] are obtained for asymmetric reconnection. The simulation results are shown in Figure 5.20. However, the scaling was found to depend on the mass ratio of the simulation. In this case the equation is generalized as $\Delta T_e = 0.017 m_i V_{A,inflow}^2$, where $V_{A,inflow}$ is the inflow Alfvn speed. Equivalently, this equation can be expressed as $\Delta T_e 0.017 B_{L,inflow}^2/\mu_0 N_{inflow}$, where $B_{L,inflow}$ and N_{inflow} are the reconnecting magnetic field and density in the inflow region.

In order to examine whether this scaling also applies to the results presented here, I have estimated the available magnetic energy as defined by [114] for each of the detected current sheets and retained the maximum value of the quantity $m_i V_A^2$ over the time interval of the current sheet. Assuming that the scaling found by [114] and [136] is indeed universal for reconnection, a good agreement between the dataset studied here and the scaling would indicate that reconnection is the dominant heating mechanism for this dataset. Figure 5.21 shows how this compares to the estimated electron heating. The correlation is low, with the correlation coefficient at 0.54. However, the value of the slope is 0.0178, which is very close to 0.017 which was found by [114]. Based on this test, it is not possible to conclude that most of the observed heating in the thin current sheets is due to reconnection, which is consistent with the fact that several low PVI current sheets in this event are associated to electron heating but do not look like reconnecting current sheets, as further discussed in 6. A possibility could be to restrict the test only to reconnecting current sheets, however as discussed above, for this event a full identification of thin current sheets with reconnection has not been possible due to the lack of high resolution plasma data. Such test could be performed with MMS

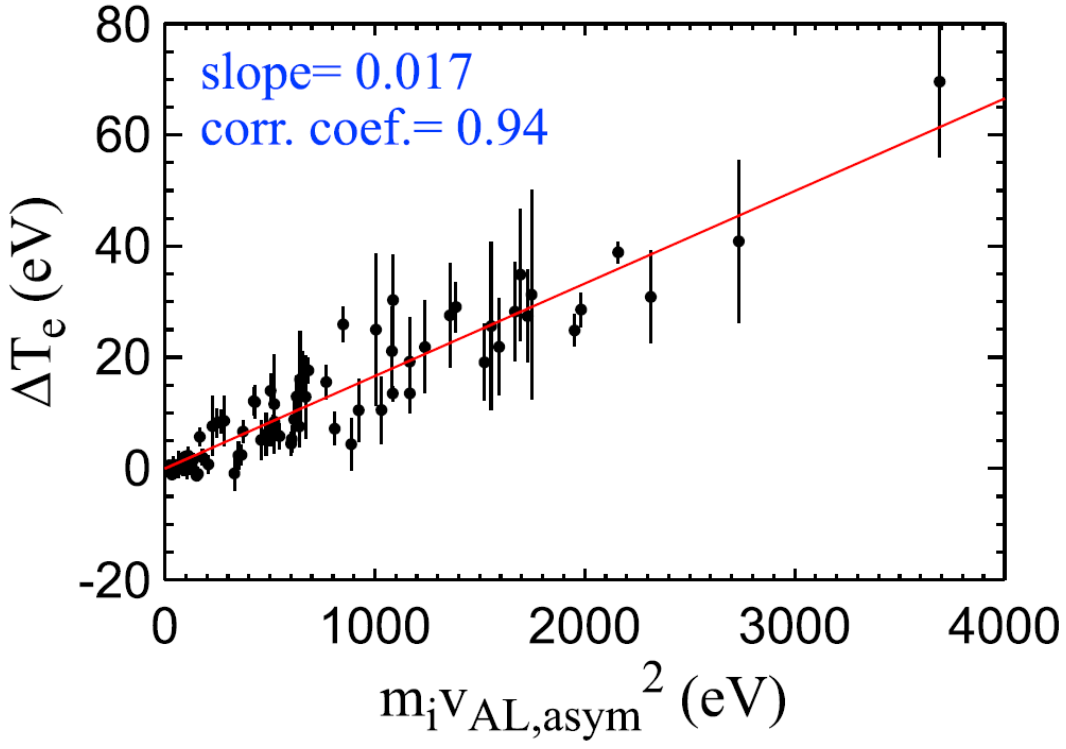

FIGURE 5.19: Observations of electron heating in the Earth's magnetopause by [114]. Electron heating as a function of the total inflowing magnetic energy.

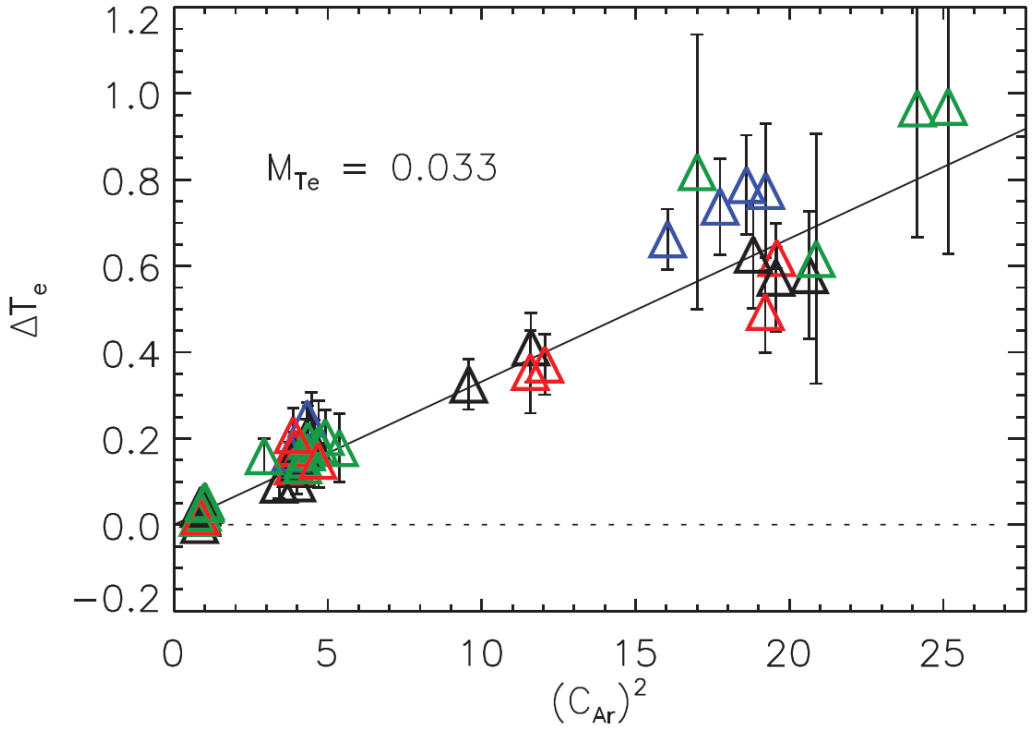

FIGURE 5.20: Results of kinetic particle-in-cell simulations by [136]. Electron heating as a function of the square of the Alfvèn velocity.

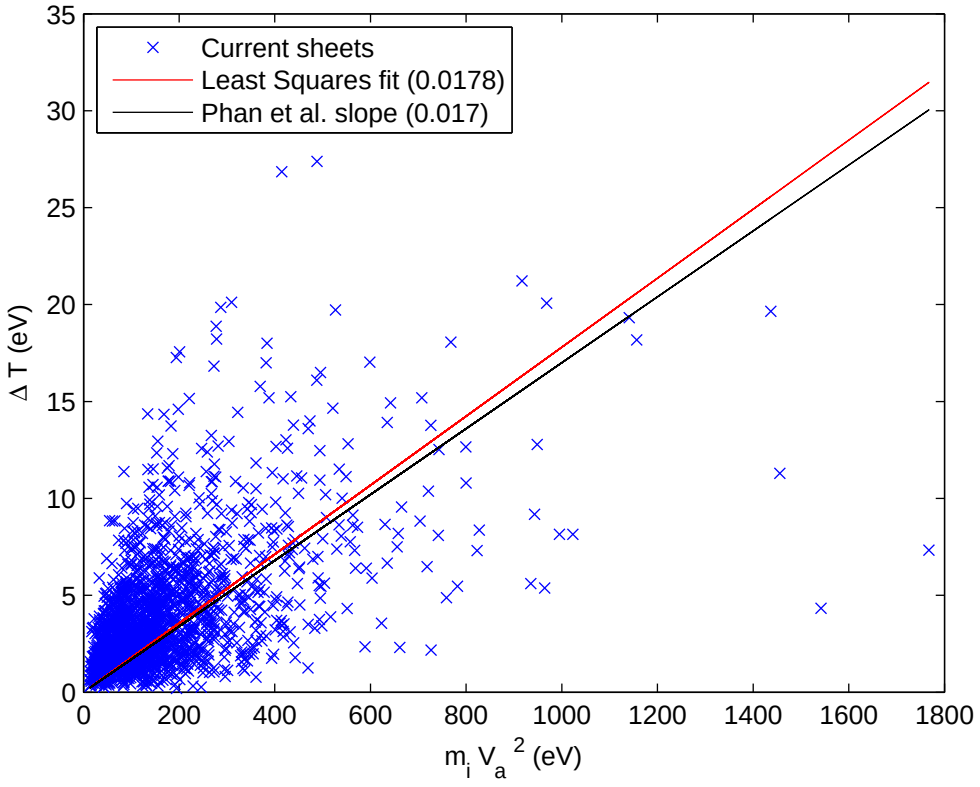

FIGURE 5.21: Scatter plot of electron heating and the available magnetic energy defined as $m_i V_a^2$. The red line represents a least squares fit of this data. It yields a slope of 0.0178, with a correlation coefficient of 0.5419. The black line is the slope of 0.017 produced by [114].

data that will be soon available in the magnetosheath and could verify if the same scaling observed at large-scale laminar boundaries such as the magnetopause is found for turbulent reconnection. The electron heating observed in a few cases during this event seems to be higher than the one expected from the scaling, as discussed in Section 5.2.3, possibly indicating that electron heating during turbulent reconnection is stronger than for the laminar case.

5.2 Electron heating within reconnecting current sheet

The first part of the results, discussed in Section 5.1, was focused on providing evidence of electron heating within thin current sheets in turbulence. Magnetic reconnection is suggested to be the dominant mechanism for high PVI current sheets, while for low PVI current sheets other mechanisms different from reconnection, such as heating within small-scale shocks or wave-particle interaction, could also occur. Such other mechanisms are the subject of future studies, as discussed in chapter 6.

Despite of the fact that reconnection is accepted as dominant dissipation and heating mechanisms for reconnection at kinetic scales, the exact way particles are heated and accelerated during reconnection is not yet fully understood both from theoretical and observational point of view. In this study, we focus on the heating of electrons. Several possibilities exist, e.g. heating due to the reconnection parallel electric field, to adiabatic Fermi and betatron mechanisms and to resonant interaction with different wave modes within current sheets. The relative importance of such mechanisms is not fully understood, as well the dependence of different boundary conditions such as guide field as well as magnetic field and density asymmetries. In this second part of the thesis, I have studied in detail one reconnecting current sheet having symmetric density, symmetric magnetic field and a very small guide field. Observations are done in the diffusion region very close to the X-line. For such current sheet, I have focused on the detailed observations of the electron distribution functions and I have attempted to evaluate the role of different heating mechanisms. The results of this part are still preliminary, in particular regarding the analysis of different wave modes in the current sheet and of their role for possible electron heating, and the study is still ongoing. The analysis of other current sheets with different values of guide field and asymmetries and the comparison of the heating mechanisms with the current sheet studied here has been left for future studies.

5.2.1 Electron heating and acceleration mechanisms

The mechanisms of electron acceleration and heating in reconnecting regions is a long standing topic, central to the study of magnetic reconnection. Even though

supra-thermal particle acceleration has been explored to a certain degree [30, 31, 49, 119], thermal heating of electrons has just recently begun to be fully addressed. A number of different studies has attempted to investigate this question both by kinetic simulations [22, 23, 136, 140] and spacecraft observations in the Earth's magnetotail [19, 57, 101], Earth's magnetopause [45, 123] and the solar wind [121]. Different mechanisms has been explored and compared, such as heating due to reconnection parallel electric field [35, 37, 45, 55, 61, 63, 140], Fermi-type acceleration due to the curvature of magnetic field lines [23, 31, 41, 49, 57, 160], betatron acceleration [41, 57, 125] and wave-particle interactions inside the diffusion region or along the separatrices [16, 45, 55, 81, 123, 125]. All these results have not yet brought to general consensus, partly because they depend strongly on the numerical limitations of each model and on observational constraints of each environment.

Numerical simulations have limitations that depend on the model, for example gyrokinetic codes are limited to strong guide fields while PIC codes are computationally heavy and are constrained to smaller simulation boxes, often unrealistic mass ratios and low velocity space resolution. Furthermore, different mechanisms are expected to occur for different configurations such as anti-parallel or strong guide field and/or symmetric or asymmetric magnetic field and density. Additionally, the previous research indicates that the contribution of each mechanism varies also at different regions inside the current sheet itself (e.g. near the x-line, in the outflow downstream from the x-line, along the separatrices), giving rise to a rather complex image with a combination of those mechanisms to different degrees at different regions.

An important problem from the experimental point of view is the fact that the detailed understanding of the heating mechanisms requires very high temporal and energy/angular resolution of particle distribution functions in thin reconnecting current sheets together with accurate measurements of the magnetic and electric field, in particular of the parallel electric field. Such measurements are seldom available in current spacecraft data. The recently launched mission MMS is going to soon provide much higher time resolution for particle measurements and therefore will improve these studies. Beyond MMS, the best available particle data currently available to resolve thin current sheets are those from Cluster at sub-spin resolution discussed in Section 4.3 and used here.

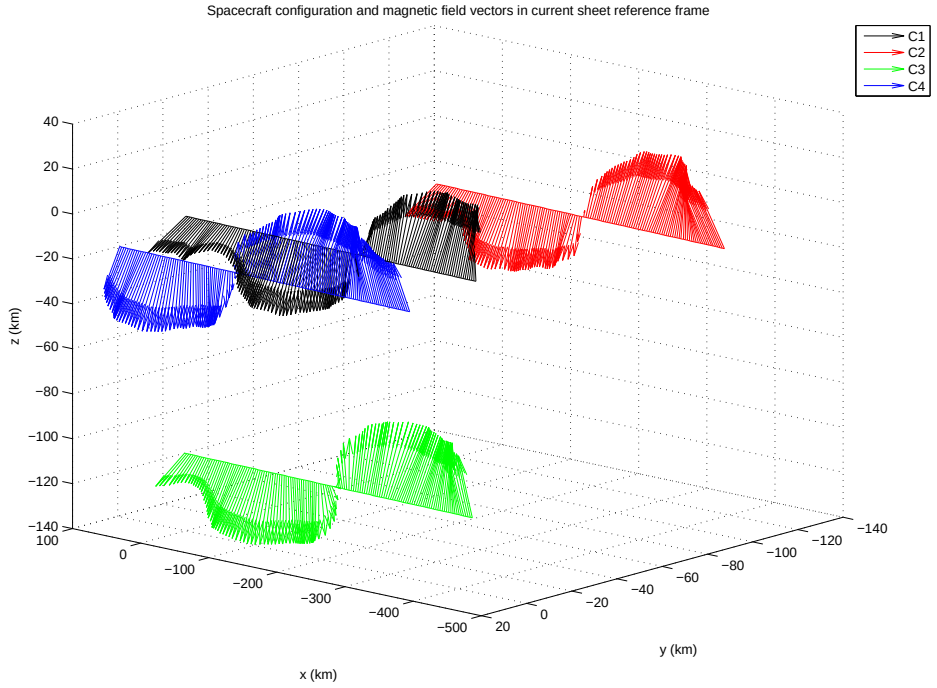

FIGURE 5.22: Configuration of the 4 spacecraft during the crossing of the current sheet in the reference frame of the current sheet. Position of the 4 spacecraft is expressed in km from the initial position of Cluster 1. The distance between Cluster 2 and Cluster 3 is $140Km$, which is comparable to the ion gyroradius.

5.2.2 Evidence of reconnection

The selected current sheet is similar to that studied in detail by [124] since it has very small guide field (the magnetic shear angle is about 170^o) and it is approximately symmetric. Yet an important difference is that the crossing of current sheet studied here is occurring closer to the X-line, with at least one spacecraft (Cluster 2) likely located around the electron diffusion region of reconnection. This allows to investigate differences in heating mechanisms very close to the X-line on scales of the order of a few ion inertial lengths.

Figure 5.23 shows the observed electric and magnetic field in the current sheet reference frame for Cluster 2 and Cluster 3. The magnetic field measurements used here is full resolution FGM data product that has a time resolution of $67Hz$. Given that the rapid changes in the magnetic field during the crossing, we combined the FGM and the STAFF data into one time series with a time resolution of $450Hz$. The comparison of the two time series verified the consistency of the profile of the magnetic field. Therefore, for this analysis the FGM time series

was sufficient, and was used throughout this investigation. Regarding the electric field measurements, only the two components of the electric field are measured directly by the spacecraft. The third component is calculated from the relation $\vec{E} \cdot \vec{B} = 0$, and that way the final data has the 3-dimensional electric field. The default value for this angle set by the instrument team at 15^o. This condition was not met at a small interval inside the current sheet, leading to the data gap in the data product provided by Cluster Science Archive. In this case we recalculated the 3-dimensional electric field from the 2 components measured directly by the spacecraft relaxing this condition for the angle to 10^o. This allowed us to have a continuous electric field measurements during the crossing.

The orientation of the current sheet was estimated by performing a Minimum Variance Analysis of the magnetic field on the two spacecraft. The results of such analysis are summarized in Tables 5.3 and 5.4. The reference frames were found to be within $\sim 10-15^o$ of each other and from GSE frame, as well as from the spin axis of the spacecraft. That fact also leads to the conclusion that at the scales of the separation of the spacecraft the current sheet is approximately planar. A timing analysis was performed to estimate the velocity of the structure which was found to be $V_cs = 170Km/s$. The normal estimated by the timing was consistent with the ones estimated by the Minimum Variance Analysis confirming the consistency of the assumptions regarding the orientation and velocity of the current sheet. The velocity of the current sheet allowed us to compute the electric field in the current sheet reference frame $\vec{E'} = \vec{E} - \vec{V_c s} \times \vec{B}$, that is the relevant frame to study reconnection inflow and outflow. In that reference frame the components (l, m, n) refer to the reconnecting component, the out-of-plane component and the normal component. The observed electric and magnetic field show signatures of ongoing reconnection in the diffusion region [33, 98, 124, 150]: a non-zero value of the normal magnetic field B_n, a quadrupolar pattern of out-of-plane B_m (Hall magnetic field) and a bipolar pattern of the perpendicular electric field E_n (Hall electric field). The fact that $B_n < 0$ and the observed polarity of B_m is negative and then positive is consistent with crossing the current sheet below the X-point.

Figure 5.23a shows that the variation in the reconnecting component B_l is sharper at Cluster 2 than at Cluster 3, consistent with the fact that C2 cross the current sheet closer to the X-line than C3. The duration of the current sheet crossing is $\sim 50ms$, $\sim 200ms$ which correspond to a thickness of $\sim 10km$, $\sim 40km$ for C2, C3 respectively by using the current sheet velocity $v_{CS} \sim 170km/s$. The ion,

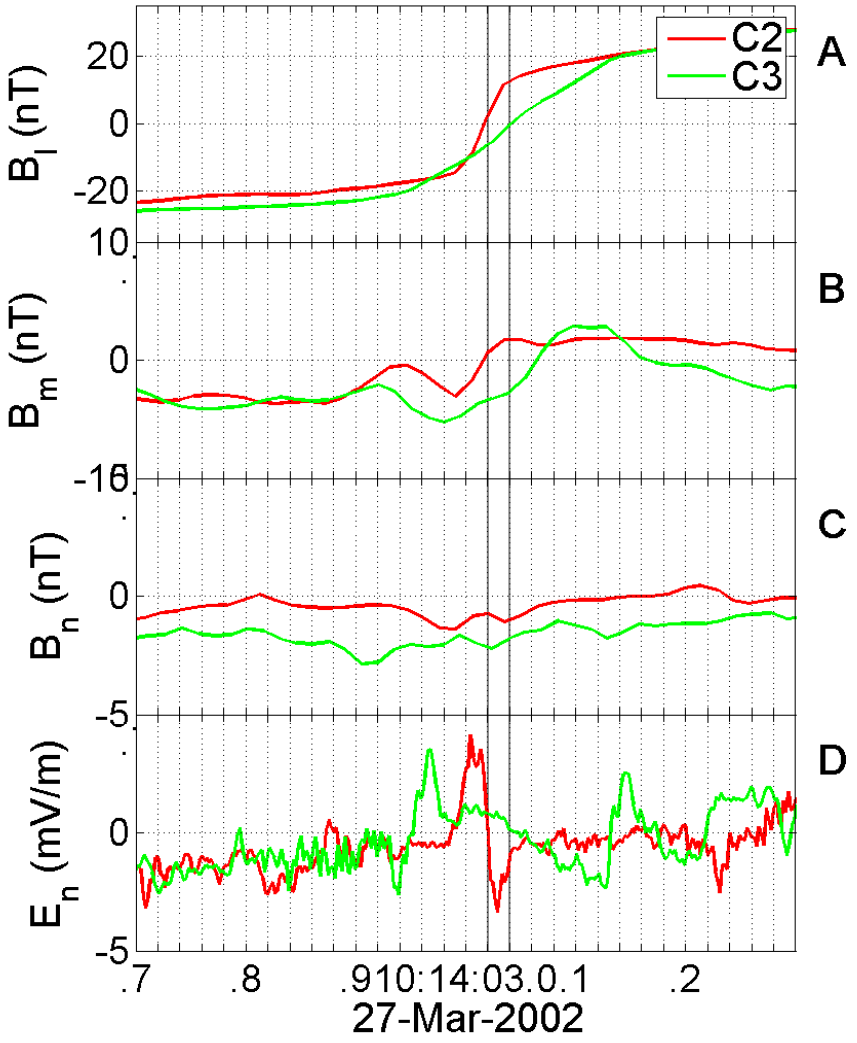

FIGURE 5.23: Cluster 2 and Cluster 3 magnetic and electric field measurements inside the current sheet. The measurements are in the reference frame of the current sheet (l, m, n). The three directions (l, m, n) refer to the reconnecting component (l), the out-of-plane component (m) and the component normal to the current sheet plane (n). Panel A shows the evolution of the reconnecting component of the magnetic field B_l. Panel B shows the out-of-plane component of the magnetic field (B_m). Panel C shows the normal component of the magnetic field (B_n). Panel D shows the normal component of the electric field (E'_n). The grey lines mark the points where each spacecraft crosses the center of the current sheet. The magnetic field was measured by FGM. The electric field was measured by EFW.

C2 MVA	X_{GSE}	Y_{GSE}	Z_{GSE}
n	0.971	-0.222	-0.077
m	0.235	0.907	0.350
l	-0.007	-0.359	0.933

TABLE 5.3: Orientation of the current sheet reference frame for Cluster 2 with respect to the GSE frame

C3 MVA	X_{GSE}	Y_{GSE}	Z_{GSE}
n	0.891	-0.448	-0.065
m	0.453	0.887	0.092
l	-0.015	-0.112	0.993

TABLE 5.4: Orientation of the current sheet reference frame for Cluster 3 with respect to the GSE frame

electron inertial range are $d_i = 100km$,$d_e = 2km$ leading to a thickness of $\sim 5d_e$, $\sim 0.5d_i$ for C2,C3 respectively. The second and fourth panel of Figure 5.23 show that the distance between the peaks in the Hall magnetic B_m and electric E_n fields (marked by vertical lines) is larger at C3 than at C2. This further substantiate the fact that C3 cross further away from the X-line than C2, as illustrated by Figure 5.24 that shows two-dimensional maps of the magnetic and electric field and electric current from a particle-in-cell simulation of reconnection by [117] over which the trajectories of C2 and C3 are overlaid. The distance between the positive and negative peaks in the normal component of the electric field E_n observed by C2 and C3 (seen in panel D of Figure 5.23) is $24ms$ for C2 and $160ms$ for C3. For the estimated velocity of the current sheet $v_{CS} \sim 170km/s$, this leads to a distance between peaks of $4km$ for C2 and $27km$ for C3. The distance between the spacecraft at that time is $141km$. This gives us an estimation of the opening angle of the outflow region $\theta = 9^o$ and of the distance from the x-line of $d_{C2} \sim 25km$ for C2 and of $d_{C3} \sim 167km$ for C3. All these estimations strongly suggest that Cluster 2 pass very close to the electron diffusion region of reconnection. It must be noted that while observations of the electron diffusion region have been reported in the Earth's magnetopause [99, 113, 133], no such reports exist for the case of reconnecting thin current sheets in turbulence. A schematic of the current sheet summarizing the observations discussed above is shown in figure 5.25. The other spacecraft Cluster 1 and Cluster 4 also cross the current sheet close to the X-line, as seen in Figure 5.22, but here I focus on the differences between Cluster 2 and Cluster 3 only.

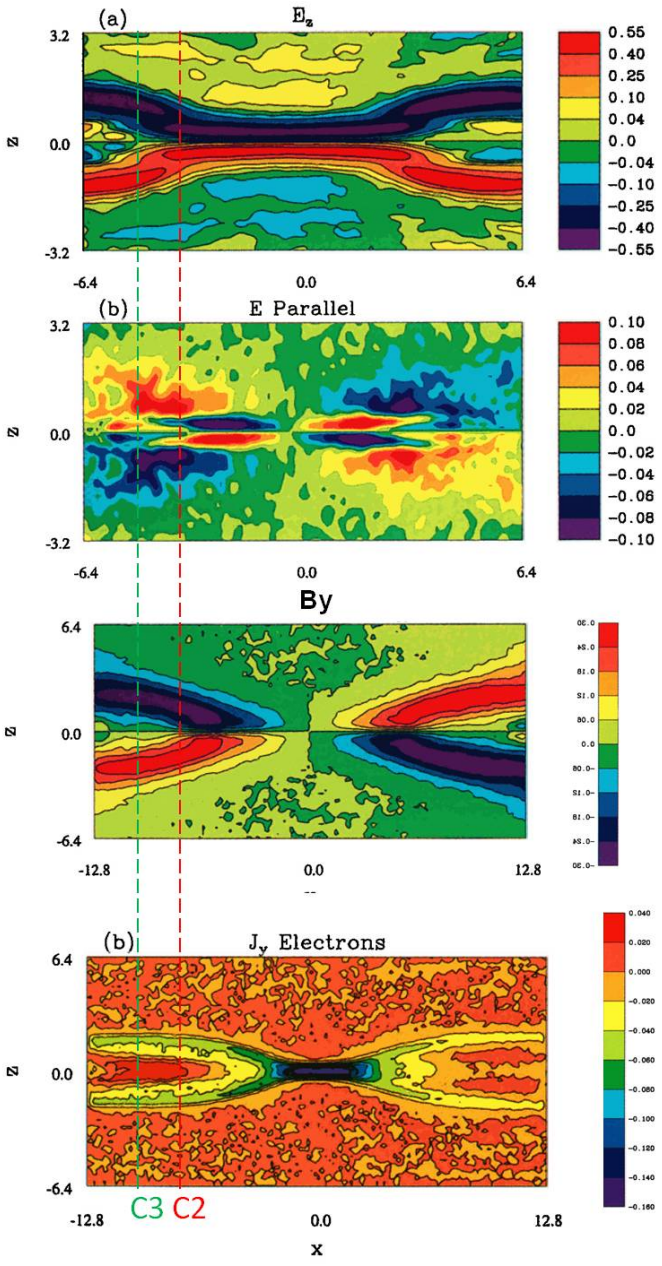

FIGURE 5.24: Simulation of magnetic reconnection using a 3-D PIC model. The dashed red and green lines mark the trajectories of Cluster 2 and Cluster 3 respectively, overlaid according to the observed magnetic and electric field configuration. Adapted from [117].

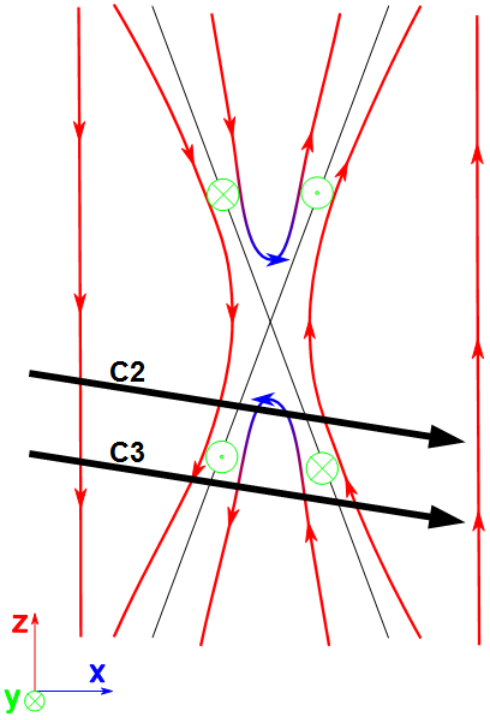

FIGURE 5.25: Schematic representation of the current sheet and the trajectories of Cluster 2 and Cluster 3.

Figure 5.26 provides additional signatures further substantiating ongoing reconnection in the current sheet for C2. The first panel of Figure 5.26 shows the reconnecting component changing sign across the current sheet center where the magnitude of the magnetic field $|B|$ is minimum (second panel of Figure 5.26). This magnetic field rotation corresponds to a strong out-of-plane electric current J_m, shown in the seventh panel of Figure 5.26). One can notice that J_m computed from single spacecraft through Faradays law (solid line), is much larger than the current provided by the curlometer method (dotted line) since the curlometer can provide only the average current over the spacecraft tetrahedron that has a scale of $\sim 100km$ while the actual current sheet thickness is smaller. The large J_m current is supported mainly by $\vec{E} \times \vec{B}$ motion of electrons within the diffusion region, as shown in the fifth panel of Figure 5.26. As expected during magnetic reconnection, plasma inflow towards the center of the current sheet, in the current sheet reference frame, is observed. This is shown in the sixth panel of Figure 5.26, where $V_n > 0$ on the left side and $V_n < 0$ on the right side, corresponding to an average reconnecting electric field (in the current sheet frame) of $E_m \sim -0.9mV/m$. It should be noted that the velocity is obtained from $\vec{E} \times \vec{B}$ since the time resolution of plasma measurements ($4s$) is too low with respect to the duration of the current

sheet crossing. One can observe also plasma outflow in the center of the current sheet with $V_l < 0$ on the fourth panel of Figure 5.26. This is consistent with crossing below the X-point and in agreement with $B_n < 0$ and the observed polarity of the quadrupolar magnetic field B_m. The observed outflow speed $V_out \sim 50km/s$ is smaller than the Alfven speed, however one should note that it is not possible to get the $\vec{E} \times \vec{B}$ flow in the very center of the current sheet because of the condition $\vec{E} \cdot \vec{B} = 0$ and a data gap is present. Such condition is necessary to compute the three components of the electric field for the two components actually measured by EFW instrument onboard Cluster. The outflow velocity V_l could be indeed higher in the center of the current sheet, where a super-alfvenic electron jet is expected from simulations and observations [113, 124]. An increase in the electron temperature in the direction parallel to the magnetic field is observed in the current sheet (ninth panel of Figure 5.26), consistent with electron heating expected during reconnection as shown in Figure 5.27 from numerical simulations [136]. This local heating is consistent with the positive value of the quantity $\vec{E} \cdot \vec{J}$ within the current sheet shown in Figure 5.26h, indicating that magnetic energy is being converted into plasma energy.

From the average inflow velocity $V_n \sim 50km/s$, one can estimate a reconnection rate $R = V_n/V_{A0} \sim 0.3$ where $V_a \sim 150km/s$ is the Alfven speed computed in the inflow region. This is consistent with a fast reconnection rate as expected for collisionless reconnection [8]. This rate is higher than found in earlier measurements during turbulent reconnection [124] but it should be considered that errors in the determination of the electric field frame are large so it is not obvious to conclude that reconnection in turbulent plasma can be faster than laminar reconnection, as indeed found in numerical simulations [134]. The reconnection rate computed as the ratio $< B_n > /B_0$ (ratio between the average normal component and the total magnetic field in the inflow region) yields $R \sim 0.1 - 0.15$ but the errors on the determination of the minimum variance frame and thus of B_n are also large. Finally, the angle of the opening of the outflow region was estimated $\theta = 9^o$, which yields a similar estimation of the reconnection rate ($R \sim 0.15$). The only conclusion that can be drawn is that reconnection is fast, as also found in previous cases [124, 141].

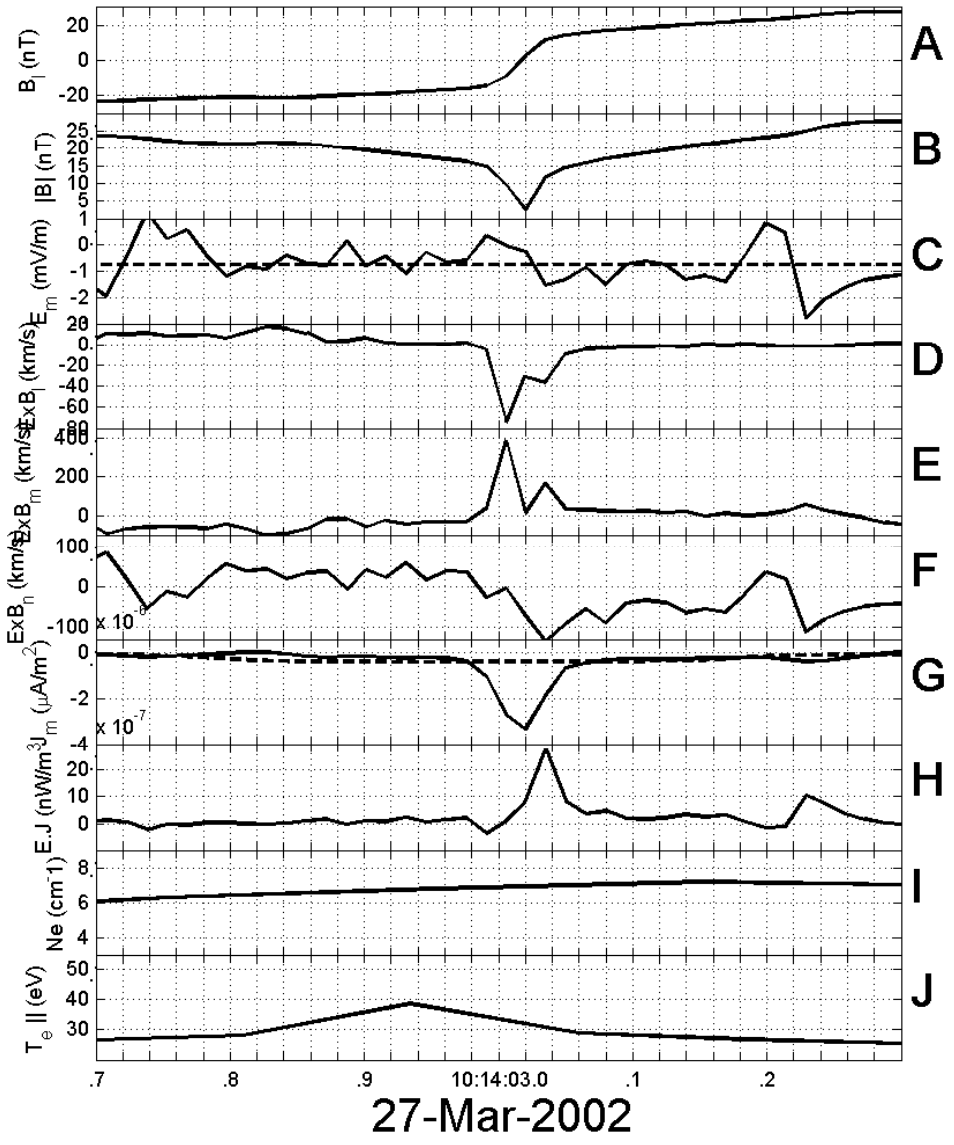

FIGURE 5.26: Cluster 2 measurements of the current sheet in the current sheet frame. Panel A shows the reconnecting magnetic field B_l. Panel B shows the magnitude of the magnetic field $|B|$. Panel C shows the out-of-plane component of the electric field E_m, the dashed lined denotes the average value inside the current sheet $< E_m >= -0.72mV/m$. Panel D shows the l component of the $\vec{E} \times \vec{B}$ flow. Panel E shows the m component of the $\vec{E} \times \vec{B}$ flow. Panel F shows the n component of the $\vec{E} \times \vec{B}$ flow. Panel G shows the out of plane component of the current J_m. The dashed line is the multi-spacecraft estimation. The solid line is the current estimated from Cluster 2 measurements using Ampere's law. Panel H shows $\vec{E} \cdot \vec{J}$. Panel I shows the density estimated by EFW potential. Panel J shows the electron temperature in the direction parallel to the magnetic field estimated from partial electron distribution functions given by PEACE 3DXPL data.

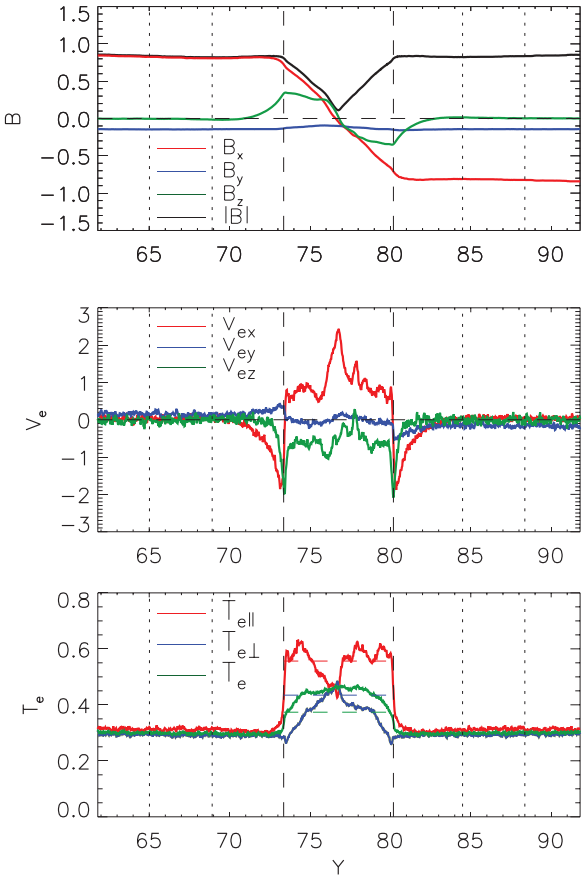

FIGURE 5.27: Results of a kinetic particle-in-cell simulation of magnetic reconneciton by [136]. The first panel shows magnetic field. The second panel shows the electron flow velocities. The third panel shows the electron temperature. The dashed vertical lines show exhaust region and the dotted vertical lines show inflow regions.

5.2.3 Electron distributions and heating

Figure 5.26j shows that electrons are substantially heated during reconnection within the diffusion region. In order to understand which is the mechanism responsible for such heating, I have compared the electron distributions in the inflow region and in center of the current sheet for both Cluster 2, closer to X-line, and Cluster 3, further downstream. During the current sheet crossings, the orientation of the current sheet is such that the direction of the reconnecting magnetic field is roughly aligned with the spin axis of the spacecraft, with an offset of $\sim 10^o$. That means that the field of view of the 12 anodes of the PEACE detector cover 180^o, from the parallel to the anti-parallel direction with respect to the magnetic field. This allowed the spacecraft to simultaneously measure both the parallel and perpendicular electron distribution functions at sub-spin time resolution $125ms$,along with the perpendicular direction that is always measured. A similar approach was

used elsewhere with Cluster data, e.g. at the bow shock [132]. The conversion from elevation angle to instrument pitch-angle was done by using the average magnetic field as measured by FGM during the $125ms$ of each sweep by PEACE. The duration of the crossing compared to that time-scale meant that the magnetic field direction used to compute the pitch angle distribution remained largely aligned with the reconnecting field. In other words the variation of the magnetic field was fast enough not to impact the validity of the pitch angle calculation. These measurements are shown in Figure 5.28.

Figure 5.28b,c show that electrons in the inflow regions on both sides of the current sheet are isotropic for both Cluster 2 and Cluster 3 and their temperature is comparable to each other $\sim 25 - 30eV$. Such electrons are heated by reconnection in the current sheet up to about $\sim 40eV$. After decomposing the electron temperature into parallel and perpendicular components, shown in the first and second panels of Figure 5.28, one can notice that closer to the X-line (at C2) electrons from the inflow region are heated mainly in the parallel direction within the current sheet while the perpendicular temperature doesn't change much. On the other hand, further downstream (at Cluster 3) both parallel and perpendicular temperatures are increased with respect to the inflow region. As discussed in the previous section, C2 is likely to be close to the electron diffusion region while C3 crosses the current sheet further away in the downstream region. For this reason, its reasonable to assume that electrons from the inflow region are first heated at C2 and that such heated electrons represent the source populations that is further heated and finally observed at C3. The distance between the two spacecraft is $140km$, which is comparable to the ion gyroradius. The observations shown in Figure 5.28 demonstrate that differences in the total temperature exist at such scales, suggesting that heating occurs at very small scales.

For the case of symmetric, anti-parallel reconnection as the case studied here, numerical simulations indicate that parallel heating can be explained by parallel electric field and/or by Fermi mechanism due to the shortening of reconnecting flux tubes [22, 37, 136]. By comparing the electron distribution function in parallel direction measured by C2 in the inflow region and in the center of the current sheet (black and blue lines respectively on the bottom left panel of figure 5.28), as well as the parallel temperature (red line on the top panel of figure5.28), we get an estimate for the parallel heating $\Delta T_e \sim 15eV$.

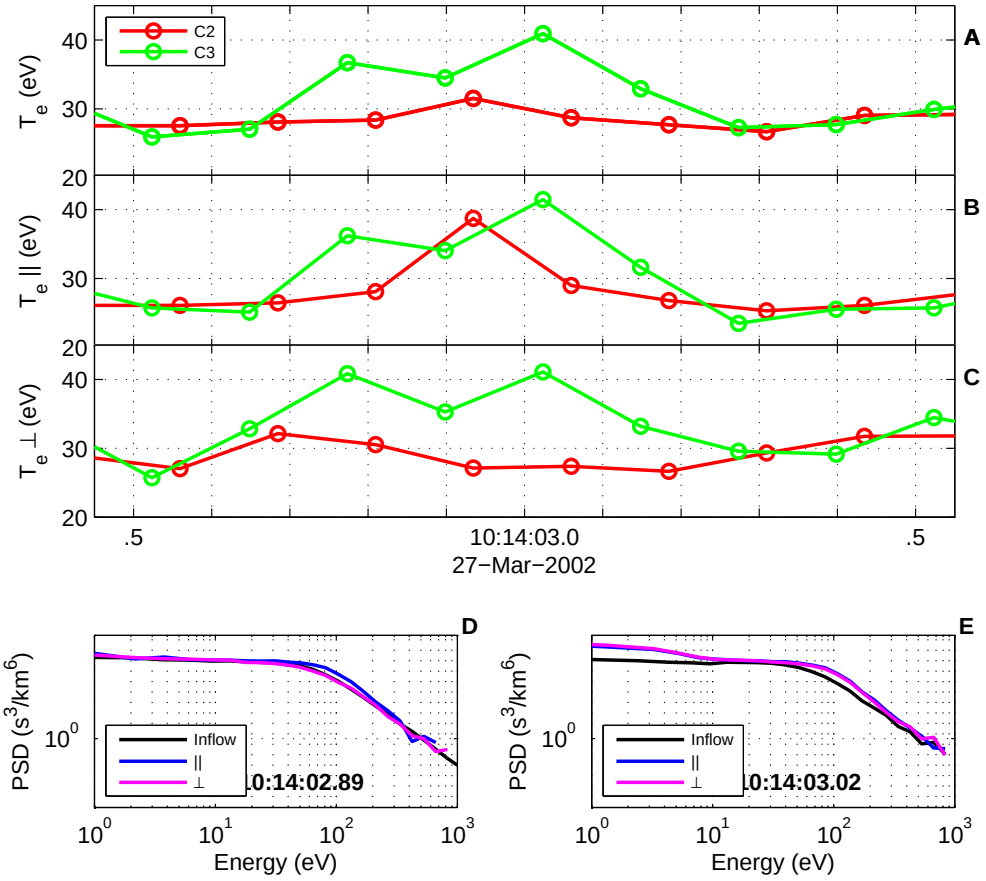

FIGURE 5.28: Electron temperature and electron distributions for Cluster 2 and Cluster 3 measured by PEACE, inside the current sheet. Panel A shows the total electron temperature for Custer 2 (red line) and Cluster 3 (green line). Panel B shows the parallel electron temperature for Custer 2 (red line) and Cluster 3 (green line). Panel C shows the perpendicular electron temperature for Custer 2 (red line) and Cluster 3 (green line). Panel D shows the electron distribution inside the current sheet for Cluster 2 in the parallel direction (blue line) and the perpendicular direction (magenta line). The black line is inflow distribution outside the current sheet. Panel E shows the electron distribution inside the current sheet for Cluster 3 in the parallel direction (blue line) and the perpendicular direction (magenta line). The black line is the electron distribution in the inflow region outside the current sheet.

If the observed heating is due to a parallel electric field distributed over the electron diffusion region having a size $\lambda_e \sim 2km$, then by taking the observed parallel electric potential $e\dot{\Phi}_{||} \sim 15eV$ one would obtain $E_{||} \sim 7.5mV/m$ that is consistent with the parallel electric fields observed in the electron diffusion region [99], although it is much larger than the reconnection electric field $\sim 1mV/m$ found in this event. Unfortunately the EFW instrument onboard Cluster cannot measure the parallel electric field, so that we cannot confirm that the estimated parallel field does actually exist. This measurement will be provided by MMS. One possibility that could be consistent with smaller values of $E_{||}$ for the same observed $\Phi_{||}$ is that the parallel electric field exist on spatial scales that are larger than the electron inertial scale as suggested by [37]. In the simulation by [37] the parallel electric potential can exist within the current sheet over several ion inertial lengths, where electrons are trapped and accelerated by the parallel field. [37] find that $ne\Phi_{||} \sim B_0^2/2mu_0$ so that the pressure associated to the parallel heated electrons balances the magnetic pressure in the inflow region. By considering in our case $B_0 = 20nT$ and $n = 7cm^{-}3$, one finds an upper limit for the parallel potential $\sim 1keV$ that is much larger than the observed $15eV$. Thus even assuming a parallel electric field distributed over a region larger than $\lambda_e \sim 2km$, it seems that heating by the parallel electric field would be sufficient to account for the observations.

Another possible mechanism to explain the observed parallel heating is the Fermi mechanism, during which energization in parallel direction is due to reflection within shortening reconnected flux tubes. Recent kinetic simulations by [22] find that for the case of a small guide field (20% of the reconnecting magnetic field) heating is dominated by the Fermi reflection of electrons downstream of X-lines, where the tension of newly reconnected field lines drives the reconnection outflow. It is not possible to quantify with our data the importance of Fermi mechanism and compare to the heating by parallel electric field. It should be noted however that the Fermi mechanism is adiabatic and it is not straightforward that electrons can remain adiabatic in the vicinity of the X-line, where spatial inhomogeneities and gradients could be comparable with the electron gyroradius and therefore could scatter the electrons, violating the conservation of the second adiabatic invariant. The current sheet thickness at C2 is $\sim 10km$, that is comparable to the gyroradius of heated electrons in the center of the current sheet at C2 (computed by using $T_e \sim 40eV$ and $B \sim B_n \sim 1.5nT$. Fermi mechanism could be more efficient further away from the X-line when reconnected flux tubes shorten to release magnetic

tension, while observations at C2 are done less than an ion inertial length away from the X-line

At Cluster 3, the observed distribution function is more isotropic. The bottom right panel of Figure 5.28 shows the electron distribution functions measured by C3 both in the inflow region and in the center of the current sheet downstream of C2. The electron distribution function in the parallel and perpendicular directions in the center of the current sheet are very similar (blue and magenta lines respectively on the bottom right panel of figure 5.28), resulting in similar parallel and perpendicular temperatures (green lines on the panels B and C of figure5.28). By taking the electron distribution measured by C2 as source population for C3, one can observe an increase in the perpendicular temperature of $\sim 15eV$ while the parallel temperature does not change. One possible explanation of such observations is that electrons from the inflow region are first accelerated in the parallel direction close to the X-line (at C2) and then they gain energy in perpendicular direction due to betatron mechanism downstream of the X-line (at C3) where the magnetic field is slightly compressed. The increase of perpendicular energy $42eV/27eV \sim 1.5$ is consistent with the compression of the magnetic field, computed as the ratio between the minimum value of $|B|$ for C2 and C3 within the center of the current sheet $|B_{C3}|/|B_{C2}| \sim 1.3$. This suggests that the isotropic temperature eventually observed at Cluster 3 in the current sheet might be the result of betatron heating of the perpendicular component. As discussed above for C2, it should be however noted that the betatron mechanism is adiabatic while the first adiabatic moment (magnetic moment) could not be conserved in the current sheet due to scattering by spatial inhomogeneities and/or waves that are observed therein, as it will be discussed in the next session. Therefore another possibility is that the observed isotropic distribution could result by scattering such as stochastic particle motion or interaction with waves [78]. In the antiparallel reconnection case discussed in recent simulations by [136], the parallel heating produced close to the X-line is isotropized downstream due to scattering mechanism. In that simulation, however, the downstream distribution is sampled far away from the X-line while in our observations C3 is located only a few ion inertial lengths away.

As discussed in Section 5.1.4, the observations of electron heating in this study show a low correlation with the empirical scaling proposed by [114] for which $\Delta T_e = 0.017 m_i V_{A,inflow}^2$. One of the reasons for such poor correlation can be the fact that in the dataset studied here reconnection is not occurring in all current

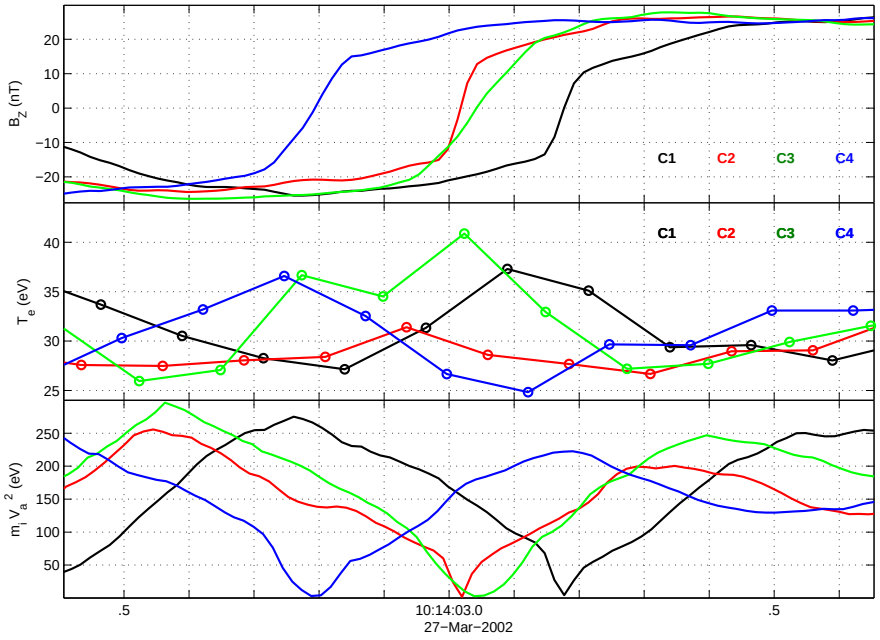

FIGURE 5.29: Evolution of the B_z component of the magnetic field, the electron temperature T_e and the available magnetic energy defined as $m_i V_a^2$.

sheets but only in those having high PVI index. It is therefore interesting to check the validity of the scaling for those current sheet where reconnection has been proved to occur. For the current sheet studied in this section, the available magnetic energy in the inflow region $m_i V_{A,inflow}^2$ is $\sim 250 - 300eV$. According to the scaling, 1.7% of this energy is converted into bulk electron heating, leading to an expected electron heating of $4 - 5eV$. This is in accordance with the heating observed by Cluster 2. However, the other three spacecraft observed significantly higher increases in electron temperature. The reason for this difference is not yet understood. One possibility could be that the heating during turbulent reconnection is on average more efficient than during laminar reconnection such as that occurring at the magnetopause, from which the scaling law is derived [114]. However more cases need to be studied to clarify this point.

5.2.4 Wave measurements

Another possibility for heating and acceleration of electrons within reconnecting current sheets is wave-particle interaction with different waves that are produced in current sheets due to reconnection dynamics [42]. Examples are Kinetic Alfven

waves, lower hybrid waves, whistler waves and high frequency plasma waves, including solitary structures such as electron holes. The wave data from instruments onboard Cluster (EFW, STAFF, WHISPER) are not fully adequate to study such waves for this event, mostly due to limitation in the sampling frequency and time resolution of spectra computed onboard. Yet, several interesting observations can be done and are discussed below. It should be noticed, however, that this part of the research work is still rather preliminary and due to lack of time several tests on wave data have not been performed yet and are part of ongoing study. Therefore the conclusions made here on heating by waves must be taken as qualitative.

One important example that have been extensively study in reconnecting current sheets are lower hybrid (LH) waves. Such waves are usually produced by the Lower Hybrid Drift Instability (LHDI) at the separatrices of reconnection due to gradients in density and magnetic field there [102, 139, 149]. LH waves have been suggested to be an important source of anomalous resistivity and diffusion for reconnection [6, 149] as well as being able to heat electrons in the direction parallel to the magnetic field through Landau resonance [12, 45, 123, 125]. The LH waves that have been earlier observed in reconnection regions are typically electrostatic with a broadband electric field spectrum near or below the local lower hybrid frequency f_{lh} [45, 64, 102, 123, 125]. Such electrostatic modes propagate perpendicular to the magnetic field ($\vec{k}\vec{B} = 0$ with $k_{\perp}\rho_e \sim 1$, where ρ_e is the electron gyroradius [45, 102]. LH waves are strongly damped at large plasma beta as shown by [6], therefore during antiparallel reconnection (as the case studied here) they are typically observed around the magnetic separatrices since in the center of the current sheet the magnitude of the magnetic field is very small.

Figure 5.30b,c shows the spectra of the out-of-plane electric field component E_m computed from electric field time series measured by the EFW instrument. A broadband electric field power is observed by C2 below the local f_{lh} (dashed line) within the current sheet, with largest amplitude at the edges of the current sheet corresponding to the separatrix region. C3 observe similar emission within the current sheet, with larger amplitude than C2. A data gap can be seen for the electric field spectra of Cluster 3 in Figure 5.30 and Figure 5.31 right after the crossing of the current sheet. The WHISPER instrument on-board Cluster 3 switches to active mode right after the spacecraft crosses the current sheet. In that mode due to the activity of the plasma sounder, electric field spectra are not calculated. The electric field observed here is similar to that found in previously

studied reconnecting current sheets, for which the electric field was demonstrated to be associated to LH waves [45, 102, 123, 149]. This suggests that LH waves are also observed in this case. Further analysis e.g. determination of wavelength and phase speed is yet necessary to confirm such interpretation. It should be noted that such waves cannot be observed by the STAFF/SA instrument, that computes wave spectra directly onboard, since $f_{lh} = 13Hz$ and the lowest frequency for which the STAFF/SA provides data in this interval is $70Hz$. In order for the electrons to be heated in the parallel direction by the LH waves, the waves must resonate with the electrons in the current sheet. This translates into the fact that their parallel phase velocity $v_{||}$ must be comparable to the local electron thermal speed $v_{Te} = 3.84Mm/s$. The resonant condition is:

$$v_{||} = \frac{\omega_{LH}}{k_{||}} = (\frac{m_i}{m_e})^{1/2}\frac{\omega_{LH}}{k_{\perp}} \tag{5.4}$$

where $v_{||}$ is the parallel phase velocity, ω_{LH} is the angular frequency of the LH waves, and $k_{||}, k_{\perp}$ are the parallel and perpendicular wavenumbers. For the case of electrostatic LH waves typically observed in reconnecting current sheets $k_{\perp} = \rho_e^{-1}$, that yields a parallel phase velocity of the waves $v_{||} = 3.77Mm/s \sim v_{Te}$. Therefore the observed LH waves observed in this case could in principle heat the electrons in parallel direction within the current sheet. Yet for the electrons to get efficiently heated by the LH waves, the electrons must stay in the current sheet for a time comparable to or longer than the typical damping time scale of the waves, as discussed in [45]. According to the study by [12], this time is $\sim$ 10 ion cyclotron times Ω_i^-1, where Ω_i is the ion cyclotron frequency. In the case of Cluster 2 the inflow velocity was $\sim 50km/s$ and the current sheet had a thickness of $\sim 10km$. Hence, the electrons remain in the diffusion region for $\sim 0.2s < \Omega_i^-1$, where $\Omega_i \sim 0.2Hz$ within the current sheet. Therefore even if the resonant condition is satisfied, it seems that the electrons do not spend enough time in the current sheet to efficiently resonante with the LH waves and thus the LH waves may not be important for electron heating in this case. This is further suggested by the fact that the electric field associated to the LH waves is stronger at C3 than at C2, so that one would expect a stronger parallel heating at C3 while the parallel heating is observed at C2. It should be noted that there are important limitations to the LH wave analysis performed here, mostly related to the poor time resolution of Cluster spacecraft, despite being in burst mode. The time resolution of electric field wave spectra from the EFW instrument is $\sim 200ms$ and this is not fully

adequate to correlate LH waves and electron distribution functions at different locations around the current sheet.

As discussed above, other wave modes have been invoked to explain electron heating and acceleration within reconnecting current sheets through wave-particle resonant interactions, e.g. whistler waves. Such waves are expected to be found in the diffusion region as a result of Hall physics leading to fast reconnection [25, 85]. Whistler waves have also been observed in the downstream region of reconnection as a result of temperature anisotropy ($T_{\perp}/T_{||} > 1$) produced by betatron acceleration in compressed magnetic field [66]. For this case, increased magnetic field wave power measured by STAFF/SA is observed between the electron gyrofrequency f_{ce} and $f_{ce}/4$ for Cluster 2 within the current sheet, as shown in Figure 5.31. Such frequency range is the range where whistler waves are typically observed within reconnection regions [66, 125]. The observed wave amplitude seems to be larger at Cluster 3, Figure 5.31e, than at Cluster 2, Figure 5.31b. Under such condition, whistler waves could resonantly heat electrons in perpendicular direction. This seems consistent with the fact that the strongest waves are observed at Cluster 3 where the heating is mostly perpendicular. However, although wave power observations indicate the possible presence of whistler waves in the current sheet, important instrumental limitations prevent in this case to make further confirmations. The time resolution of wave spectra by STAFF/SA is $\sim 200ms$ ([100]) but the time resolution of polarization measurements is lower $\sim 1s$ ([100]), and therefore it is not possible to directly verify the actual polarization of the candidate whistler waves. Such analysis, as well as the computation of Poynting vector, could be performed directly by combining EFW electric field measurement with STAFF/SC search coil magnetometer measurements, yet the sampling frequency of Cluster in burst mode is $450Hz$ while such high-frequency waves are observed around $\sim 500Hz$ and above.

Higher frequency wave modes have also been invoked to explain electron heating and acceleration in reconnection regions. Examples are waves around the local plasma frequency and the upper hybrid frequency [123, 149] and electrostatic solitary sructures such as electron holes and double layers [16, 65]. For this event, we do not have access to high-frequency electric field waveforms at several kHz that are provided by the Wideband (WDB) instrument onboard Cluster only in normal mode, due to telemetry limitations. On the other hand, electric field spectra from WHISPER instrument can still be used. Whisper provides an integrated

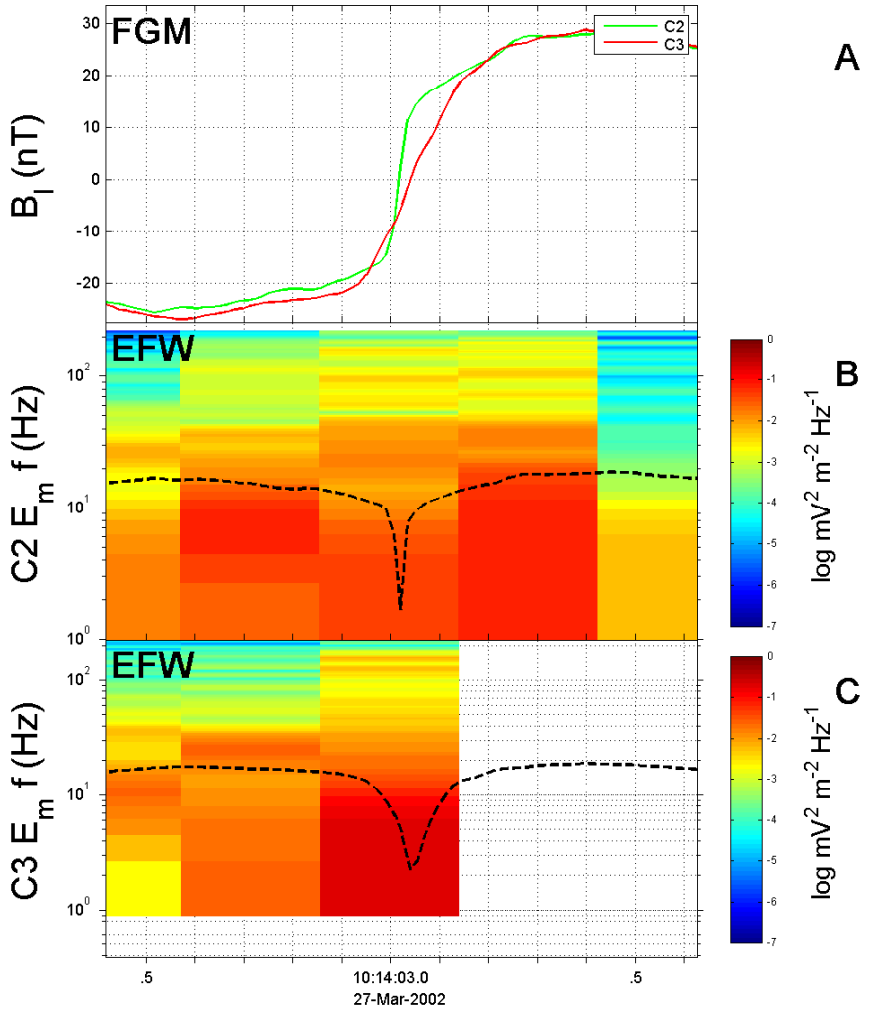

FIGURE 5.30: Magnetic field measurements of the B_l component measured by FGM (Panel A)and the electric field spectra calculated from data by EFW for Cluster 2 (Panel B) and Cluster 3 (Panel C). The dashed black line denotes the lower hybrid freqency f_{LH}. The left half of panel C is empty since there is a data gap due to WHISPER switching to active mode.

power of electric field at time resolution of $16ms$ ($62.5Hz$) and in the frequency range of $2-80kHz$ as well as spectra computed during $112ms$ every $320ms$ and frequency range of $2-80kHz$. Figure 5.32 show that enhanced wave emission in the frequency range of $2-80kHz$ is observed when Cluster 2 and Cluster 3 cross the magnetic separatrices. Such signatures at separatrices is consistent with ongoing reconnection as shown earlier [123, 150] and is associated to the acceleration of electrons at supra-thermal energies. Yet, the emissions shows high temporal variability and are not always located at the separatrices. As seen in 5.32 they are observed simultaneously by all 4 Cluster spacecraft, but at the moment when

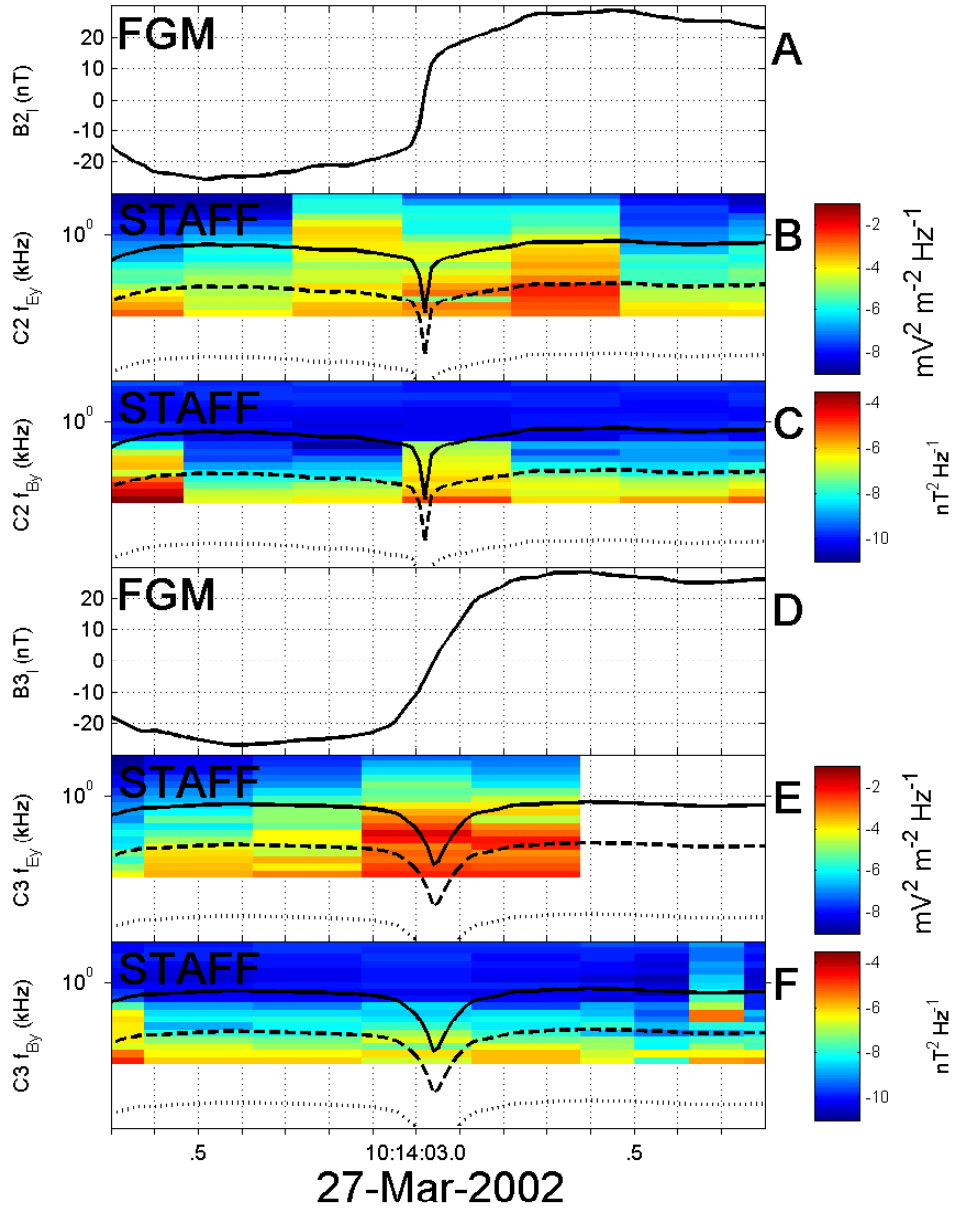

FIGURE 5.31: Magnetic field measurements of the B_l component measured by FGM for Cluster 2 (Panel A) and Cluster 3 (Panel D)and the spectra by STAFF/SA of the electric field (Panel B for Cluster 2 and Panel E for Cluster 3) and the magnetic field (Panel C for Cluster 2 and Panel F for Cluster 3). The solid black line denotes the electron gyrofrequency f_{ce}, the dashed black line denotes the frequency $f_{ce}/4$. The dotted black line denotes the lower hybrid freqency f_{LH}.

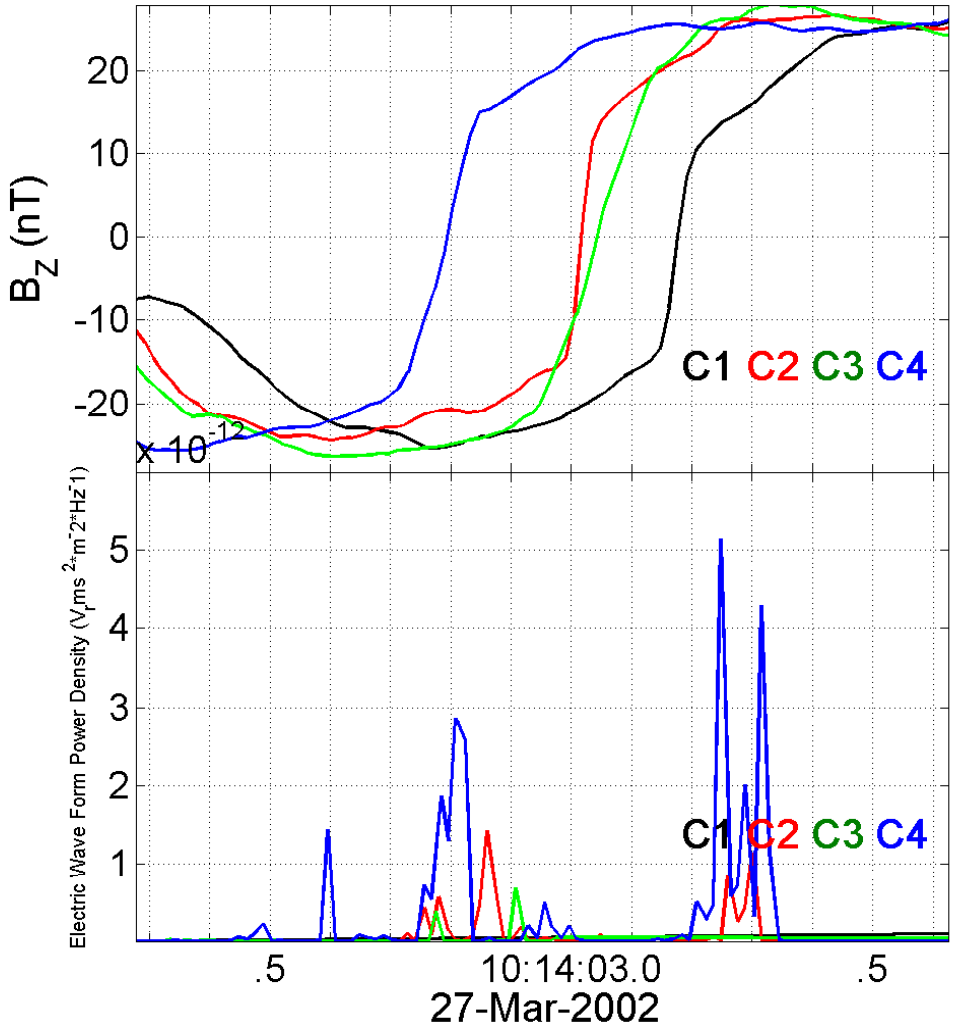

FIGURE 5.32: Magnetic field measurements of the B_z component measured by FGM and the integrated wave power measured by WHISPER.

these peaks are observed only Cluster 2 and Cluster 3 are near the separatrices, while Cluster 1 and 4 are elsewhere. This suggests that temporal effects possibly also not related to local reconnection physics (e.g. beams from shock regions) might be also at play. Unfortunately WHISPER cannot provide spectra at such time resolution, and the measured spectra (which are computed during $112ms$ once every $320ms$) do not coincide with the observed peaks, therefore we have no information regarding the frequency of these emissions and it is therefore difficult to identify the specific wave mode.

Chapter 6

Conclusion and future work

6.1 Conclusion

In this thesis I performed a study of thin current sheets in the Earth's magnetosheath downstream of the quasi-parallel shock. For the first time, evidence of electron heating within current sheets at kinetic scale was provided. Additionally, a detailed analysis of the electron heating mechanisms in the diffusion region of a reconnecting current sheet was performed.

The detection of the current sheets was done by implementing the Partial Variance of Increments technique for multi-spacecraft data instead of the single-spacecraft technique that was used in past studies. The multi-spacecraft approach allowed us to focus on proton-scale structures, which has not been possible until now. This highlights the importance of multi-spacecraft missions such as Cluster and MMS for the study of magnetic reconnection and turbulent dissipation at kinetic scales. The use of the PVI technique as a detection method was compared against alternative approaches, namely the magnetic shear angle and a direct estimation of the current using the curlometer technique. These diagnostics validated this method as an optimal choice for the detection of current sheets in turbulence.

The proton-scale current sheets that were detected using the PVI technique were divided into two main populations. The first population includes $\sim 85\%$ of the total number of structures. It is characterized by low values of the PVI index, which indicates relatively weak electric current. For the majority of this population, the magnetic shear angle had values lower than 90^o. The second population includes

the remaining $\sim 15\%$. It is characterized by high values of the PVI index, and therefore strong current. The observed magnetic shear angles were larger than 90^o. The existence of two distinct populations may point to different formation mechanisms [97]. According to this argument, the low PVI structures are generated locally by the turbulence, while the high-PVI/high-shear structures could originate from the bow-shock or the solar wind, and be convected through the magnetosheath.

In order to study the electron heating occurring within such structures, measurements of the electron temperature at high time resolution were needed. The electron moments are computed by the Cluster spacecraft from the full distribution functions which are available once per spin. That time resolution of $4s$ was not sufficient, since the duration of proton-scale structures was below that. Therefore, a proxy of the temperature was estimated the partial distribution functions measured by the PEACE instrument at sub-spin resolution of $125ms$. The electron temperature obtained by this approach was used to estimate local enhancement of the temperature which indicates the amount of bulk electron heating inside each current sheet. For the overwhelming majority of the low PVI current sheets no significant heating was observed. Specifically, for $\sim 90\%$ of structures with $PVI < 3$ the temperature increase was below $1\sigma_T e$. $\sigma_T e$ was defined as the standard deviation of the temperature during the event and denotes possible temperature increase we expect to observe due to random fluctuations. This was not the case, however, for the high PVI current sheets. About half of the current sheets with $PVI > 3$ showed an increase in temperature above $1\sigma_T e$, with a small percentage having a temperature increase larger than $3\sigma_T e$. This trend was even more pronounced for current sheets with very high PVI index. The temperature enhancement was larger than $1\sigma_T e$ for $\sim 80\%$ of current sheets with $PVI > 5$. Additionally, heating above $3\sigma_T e$ was observed in $\sim 10\%$ of those cases. Although earlier observational studies have attempted to study the role of intermittent structures such as current sheets in turbulence [105, 141, 161], evidence of particle heating within such structures was limited to specific case studies of single current sheets [124]. On the other hand, studies that did examine electron heating in turbulence, did so in statistical surveys over long time intervals without being able to identify where the observed heating occurs [104]. Here, for the first time, we were able to demonstrate that significant localized electron heating occurs within proton-scale current sheets. These results indicate that such structures have an important contribution to dissipation at kinetic scales [17].

One current sheet was studied in detail in order to examine the properties of the observed electron heating and investigate the underlying physical mechanisms. For this current sheet, the magnetic field and density where symmetric on the inflow regions of the current sheet. The magnetic shear angle was $\sim 170^o$, making it a case of very small guide field (anti-parallel) current sheet. The Hall magnetic and electric fields and the $\vec{E} \times \vec{B}$ flows showed evidence of ongoing reconnection. Two of the spacecraft, Cluster 2 and Cluster 3, crossed the current sheet almost simultaneously. The electric and magnetic field measurements were consistent with the two spacecraft crossing at the same side with respect to the x-line, and with Cluster 2 crossing close to the x-line while Cluster 3 crossed further away downstream. The estimated distance of Cluster 2 from the x-line was a fraction of an ion gyro-radius, while the distance between the two spacecraft was of the order of an ion gyro-radius. Additionally, the orientation of the current sheet was such that meant that partial electron distributions provided by PEACE were covering the pitch angle directions both the parallel and perpendicular to the magnetic field. This provided a unique opportunity to compare the parallel and perpendicular electron distributions inside the diffusion region at different distances from the x-line. The heating observed close to the x-line by Cluster 2 was almost exclusively parallel to the magnetic field, while no heating was observed in the perpendicular direction by Cluster 2. In contrast, Cluster 3 observed a more isotropic distribution with increased temperature in both parallel and perpendicular direction with respect to the inflow region. The parallel heating observed by Cluster 2 in close proximity to the x-line is consistent with heating due to parallel electric field. However, an interpretation of the heating via a Fermi-type mechanism due to field line curvature or wave-particle interactions with Lower Hybrid mode waves cannot be excluded. The apparent enhancement of the perpendicular temperature of the electron distribution downstream from the x-line observed by Cluster 3, can be due to betatron acceleration or wave-particle scattering. However, the limitations of the available wave data provided by Cluster did not allow for conclusive results regarding the mechanisms of electron heating. While past studies have investigated the mechanisms of electron heating in large-scale reconnection at the Earth's magnetopause and magnetotail [45, 114, 125], it must be noted that this is the first such study in a thin current sheet in turbulence. The observed evolution of the electron distributions over such small scales and at such proximity to the x-line mean that the electron heating mechanisms develop over a just few ion inertial lengths. However, further investigation is necessary in order to provide

definitive answers regarding the specific heating mechanisms that dominate inside the diffusion region.

6.2 Future Work

The results presented here have offered valuable insights into the properties of current sheets at kinetic scales in turbulent plasma and the physics of magnetic reconnection that takes place within those structures. However, they also gave rise to a number important topics and questions that could not be investigated in detail during this thesis. The limitations of the present work, to an extent imposed by the capabilities of the instruments, indeed left a number of open questions which serve to outline future directions of inquiry.

A topic that was not investigated in depth here, concerns different kinds of structures such as vortices and shocklets that can also lead to particle heating and acceleration. Such structures have been identified in our data set, and in a few cases significant electron heating was observed even though they were characterized by relatively moderate values of the PVI index. A more detailed study of such cases will allow us to investigate dissipation mechanisms at kinetic scales alternative to magnetic reconnection.

I also examined an interval of Cluster data in the pristine solar wind. The motivation behind the investigation in the solar wind was two fold. First, it is important to examine whether the results obtained here are valid in the pristine solar wind, where the properties of the turbulence are different from those in the shocked solar wind plasma of the magnetosheath. Second, it would allow us to directly compare the results presented here with previous studies which were performed in the solar wind [104, 105, 111], although most of those studies have not directly addressed the kinetic scales. The method used here to estimate the electron temperature at sub-spin resolution could also be applied in the solar wind. However, the properties of the electron distribution in the solar wind make this approach less reliable. The main problem is that the electron temperature in the solar wind is on average lower than that in the magnetosheath. An electron temperature of the order of $\sim 5 - 10eV$, which is typical for the solar wind is very close to typical values of the spacecraft potential. This means that a significant part of the thermal core of the distribution is contaminated by photo-electrons. Assuming that the relative

electron heating is similar to what was observed in the magnetosheath, in the order of $\Delta T_e/T_e$ up to $\sim 50\%$, an estimation of the actual $\Delta T_e/T_e$ would be very difficult with the available instruments. Additionally, the high energy tail (halo) is more prominent with respect to the thermal part (core). This makes it more difficult to sufficiently sample the thermal part of the distribution and to make a reliable estimation of its temperature, although fitting the core and the halo simultaneously by a bi-maxwellian or maxwellian and a kappa distribution, could mitigate this issue. Finally, for such a study it is necessary that the instruments operate in Burst Mode, which is rare when the Cluster spacecraft are in the solar wind. Therefore, we were not able to obtain an estimation of electron temperature at sub-spin time resolution in this case.

Another important aspect is to investigate in what way the properties of the intermittent structures depend on the parameters of the turbulence. Data from the Cassini mission allowed us to examine the turbulence in the Saturn system. The available data allow us to examine intervals of magnetosheath data for a wide range of bow-shock parameters, which is not possible in near-Earth space. The Kronian bow-shock has a higher Mach number [88], different plasma parameters, and the size of the system is much larger compared to Earth. The turbulence of Saturn's magnetosheath has not been explored until very recently. Studies of Saturn's magnetosheath [52] and magnetosphere [154] have opened the way to a more concrete understanding of the properties of the turbulence in the Kronian system. However, such an investigations had to rely mainly on magnetic field measurements, since the particle data measurements by Cassini are of relatively low quality. A preliminary investigation, performed during this thesis, involved using a single spacecraft PVI technique to identify structures in Saturn's magnetosheath, downstream of the quasi-parallel shock. We notice a similar pattern to the one observed in the terrestrial magnetosheath and the solar wind, with two distinct populations emerging. A large population with low PVI index and low magnetic shear angles and a smaller population with high PVI index and high magnetic shear angle. The limitations of the instruments on board Cassini are such that a study of turbulent reconnection and the associated particle heating and acceleration could not be completed at this stage.

Finally, it is important to note that the observations of proton-scale current sheets in the magnetosheath hint at magnetic reconnection as an underlying mechanism of bulk heating. In particular, the high PVI population had characteristics that

appear to be consistent with magnetic reconnection. Numerical studies [135] and solar wind observations [105] have indicated a link between high values of the PVI index and the probability of reconnection. The observed electron heating inside those current sheets also points to magnetic reconnection, although it must be noted that other mechanisms can account for such localized heating at kinetic scales. However, due to the limitations of the available instruments, no conclusive evidence can be provided with the current data. Further studies are necessary in order to determine with certainty how frequent reconnection is in intermittent structures that form in turbulent plasma and how significant is its contribution to dissipation at kinetic scales. Additionally, the contribution to dissipation of other processes, either localized such as shocklets and vortices or more uniform such as wave-particle interactions via Landau damping will provide a full picture of the physics of turbulent dissipation at kinetic scales. Furthermore, although an investigation of the properties of electron heating inside the diffusion region of a reconnecting current sheet was performed, the analysis of the mechanisms that cause the observed electron heating in turbulent reconnection could not be completed. At this stage, the particular mechanisms behind the heating and acceleration of particles within thin reconnecting current sheets in turbulence remain largely under investigation. The results of this investigation will allow for a more complete image of the energy conversion mechanisms in turbulent reconnection and the properties of the resulting particle heating and acceleration.

The MMS mission (`http://mms.gsfc.nasa.gov/`) will provide the data needed to further investigate these questions. The presence of eight top-hat electrostatic analyzers allows for the measurement of full distribution functions and the calculation of particle moments at higher time resolution than Cluster ($30ms$ for electrons $150ms$ for ions). Additionally, rigid antennas will allow to measure the third component of the electric field along the direction of the spin axis, thus permitting to measure the full three dimensional electric field. Also the small spacecraft separation will lead to better estimation of the current through the curlometer technique, in particular at electron scales.

Additionally, data from future missions such as the proposed THOR mission (`http://thor.irfu.se/`) will allow to further understand turbulent reconnection as an energy dissipation mechanism. THOR will be fully devoted to solve the problem of energy dissipation and particle energization in turbulent plasma at kinetic scales. The proposed mission will provide particle data at an even

higher resolution in particular in the velocity space via an increased energy resolution as well as more accurate wave measurements, which are necessary in order to investigate wave-particle interactions within reconnecting current sheets. Such measurements will not only make a statistical study of reconnection in thin current sheets in turbulence feasible but will also allow for detailed observations of the kinetic phenomena inside intermittent structures.

The results of these investigations would have far reaching implications, not only in the study of turbulent reconnection in near-Earth space, but in every domain where turbulence and reconnection co-exist, from laboratory experiments to astrophysical systems.

Bibliography

[1] O. Alexandrova, C. Lacombe, and A. Mangeney. Spectra and anisotropy of magnetic fluctuations in the Earth's magnetosheath: Cluster observations. *Annales Geophysicae*, 26:3585–3596, November 2008. doi: 10.5194/angeo-26-3585-2008.

[2] O. Alexandrova, C. Lacombe, A. Mangeney, R. Grappin, and M. Maksimovic. Solar Wind Turbulent Spectrum at Plasma Kinetic Scales. *Astrophysical Journal*, 760:121, December 2012. doi: 10.1088/0004-637X/760/2/121.

[3] O. Alexandrova, C. H. K. Chen, L. Sorriso-Valvo, T. S. Horbury, and S. D. Bale. Solar Wind Turbulence and the Role of Ion Instabilities. *Space Science Reviews*, 178:101–139, October 2013. doi: 10.1007/s11214-013-0004-8.

[4] Vassilis Angelopoulos, James P. McFadden, Davin Larson, Charles W. Carlson, Stephen B. Mende, Harald Frey, Tai Phan, David G. Sibeck, Karl-Heinz Glassmeier, Uli Auster, Eric Donovan, Ian R. Mann, I. Jonathan Rae, Christopher T. Russell, Andrei Runov, Xu-Zhi Zhou, and Larry Kepko. Tail reconnection triggering substorm onset. *Science*, 321(5891):931–935, 2008. doi: 10.1126/science.1160495.

[5] M. J. Aschwanden. *Physics of the Solar Corona. An Introduction.* Praxis Publishing Ltd, August 2004.

[6] S. D. Bale, F. S. Mozer, and T. Phan. Observation of lower hybrid drift instability in the diffusion region at a reconnecting magnetopause. *Geophysical Research Letters*, 29(24):33–1–33–4, 2002. ISSN 1944-8007. doi: 10.1029/2002GL016113. 2180.

[7] W. Baumjohann and R.A. Treumann. *Basic Space Plasma Physics.* Imperial College Press, 2012. ISBN 9781848168947.

[8] J. Birn and M. Hesse. Geospace Environment Modeling (GEM) magnetic reconnection challenge: Resistive tearing, anisotropic pressure and hall effects. *Journal of Geophysics Research*, 106:3737–3750, March 2001. doi: 10.1029/1999JA001001.

[9] R. Bruno and V. Carbone. The Solar Wind as a Turbulence Laboratory. *Living Reviews in Solar Physics*, 10:2, May 2013. doi: 10.12942/lrsp-2013-2.

[10] R. Bruno, V. Carbone, P. Veltri, E. Pietropaolo, and B. Bavassano. Identifying intermittency events in the solar wind. *Planetary and Space Science*, 49:1201–1210, October 2001. doi: 10.1016/S0032-0633(01)00061-7.

[11] R. Bruno, V. Carbone, L. Primavera, F. Malara, L. Sorriso-Valvo, B. Bavassano, and P. Veltri. On the probability distribution function of small-scale interplanetary magnetic field fluctuations. *Annales Geophysicae*, 22:3751–3769, October 2004. doi: 10.5194/angeo-22-3751-2004.

[12] I. H. Cairns and B. F. McMillan. Electron acceleration by lower hybrid waves in magnetic reconnection regions. *Physics of Plasmas*, 12(10):102110, October 2005. doi: 10.1063/1.2080567.

[13] E. Camporeale and D. Burgess. The Dissipation of Solar Wind Turbulent Fluctuations at Electron Scales. *Astrophysical Journal*, 730:114, April 2011. doi: 10.1088/0004-637X/730/2/114.

[14] P. A. Cassak and M. A. Shay. Scaling of asymmetric magnetic reconnection: General theory and collisional simulations. *Physics of Plasmas*, 14(10): 102114, October 2007. doi: 10.1063/1.2795630.

[15] P. A. Cassak and M. A. Shay. Scaling of asymmetric Hall magnetic reconnection. *Geophysical Research Letters*, 35:L19102, October 2008. doi: 10.1029/2008GL035268.

[16] C. Cattell, J. Dombeck, J. Wygant, J. F. Drake, M. Swisdak, M. L. Goldstein, W. Keith, A. Fazakerley, M. André, E. Lucek, and A. Balogh. Cluster observations of electron holes in association with magnetotail reconnection and comparison to simulations. *Journal of Geophysical Research (Space Physics)*, 110:A01211, January 2005. doi: 10.1029/2004JA010519.

[17] A. Chasapis, A. Retinò, F. Sahraoui, A. Vaivads, Y. V. Khotyaintsev, D. Sundkvist, A. Greco, L. Sorriso-Valvo, and P. Canu. Thin Current Sheets

and Associated Electron Heating in Turbulent Space Plasma. *Astrophysical Journal, Letters*, 804:L1, May 2015. doi: 10.1088/2041-8205/804/1/L1.

[18] C. C. Chaston, T. D. Phan, J. W. Bonnell, F. S. Mozer, M. Acuña, M. L. Goldstein, A. Balogh, M. Andre, H. Reme, and A. Fazakerley. Drift-kinetic alfvén waves observed near a reconnection x line in the earth's magnetopause. *Phys. Rev. Lett.*, 95:065002, Aug 2005. doi: 10.1103/PhysRevLett.95.065002.

[19] L.-J. Chen, N. Bessho, B. Lefebvre, H. Vaith, A. Fazakerley, A. Bhattacharjee, P. A. Puhl-Quinn, A. Runov, Y. Khotyaintsev, A. Vaivads, E. Georgescu, and R. Torbert. Evidence of an extended electron current sheet and its neighboring magnetic island during magnetotail reconnection. *Journal of Geophysical Research (Space Physics)*, 113:A12213, December 2008. doi: 10.1029/2008JA013385.

[20] A. C.-L. Chian and P. R. Muñoz. Detection of Current Sheets and Magnetic Reconnections at the Turbulent Leading Edge of an Interplanetary Coronal Mass Ejection. *Astrophysical Journal, Letters*, 733:L34, June 2011. doi: 10.1088/2041-8205/733/2/L34.

[21] S. C. Cowley and Jr. J. Peoples. *Plasma Science: Advancing Knowledge in the National Interest*. The National Academies Press, Washington, DC. ISBN 978-0-309-10943-7.

[22] J. T. Dahlin, J. F. Drake, and M. Swisdak. The mechanisms of electron heating and acceleration during magnetic reconnection. *Physics of Plasmas*, 21(9):092304, September 2014. doi: 10.1063/1.4894484.

[23] J. T. Dahlin, J. F. Drake, and M. Swisdak. Electron Acceleration in 3D Magnetic Reconnection with a Guide Field. *ArXiv e-prints*, March 2015.

[24] W. Daughton, V. Roytershteyn, H. Karimabadi, L. Yin, B. J. Albright, B. Bergen, and K. J. Bowers. Role of electron physics in the development of turbulent magnetic reconnection in collisionless plasmas. *Nature Physics*, 7: 539–542, July 2011. doi: 10.1038/nphys1965.

[25] X. H. Deng and H. Matsumoto. Rapid magnetic reconnection in the Earth's magnetosphere mediated by whistler waves. *Nature*, 410:557–560, March 2001.

[26] P. Dmitruk and W. H. Matthaeus. Structure of the electromagnetic field in three-dimensional Hall magnetohydrodynamic turbulence. *Physics of Plasmas*, 13(4):042307, April 2006. doi: 10.1063/1.2192757.

[27] P. Dmitruk and W. H. Matthaeus. Test particle acceleration in three-dimensional Hall MHD turbulence. *Journal of Geophysical Research (Space Physics)*, 111:A12110, December 2006. doi: 10.1029/2006JA011988.

[28] P. Dmitruk, W. H. Matthaeus, and N. Seenu. Test Particle Energization by Current Sheets and Nonuniform Fields in Magnetohydrodynamic Turbulence. *Astrophysical Journal*, 617:667–679, December 2004. doi: 10.1086/425301.

[29] Yue Dong. *Analyse spectrale des mócanismes de propagation et de dissipation de la turbulence dans les plasmas de vent solaire et de tokamaks*. PhD thesis, Ecole Polytechnique, 2014.

[30] J. F. Drake, M. A. Shay, W. Thongthai, and M. Swisdak. Production of Energetic Electrons during Magnetic Reconnection. *Physical Review Letters*, 94(9):095001, March 2005. doi: 10.1103/PhysRevLett.94.095001.

[31] J. F. Drake, M. Swisdak, H. Che, and M. A. Shay. Electron acceleration from contracting magnetic islands during reconnection. *Nature*, 443:553–556, October 2006. doi: 10.1038/nature05116.

[32] J. W. Dungey. Conditions for the occurence of electrical discharges in astrophysical systems. *Philosophical Magazine*, 44(354):725–738, 1953. ISSN 0031-8086.

[33] J. P. Eastwood, T. D. Phan, M. Øieroset, and M. A. Shay. Average properties of the magnetic reconnection ion diffusion region in the Earth's magnetotail: The 2001-2005 Cluster observations and comparison with simulations. *Journal of Geophysical Research (Space Physics)*, 115:A08215, August 2010. doi: 10.1029/2009JA014962.

[34] J. P. Eastwood, T. D. Phan, J. F. Drake, M. A. Shay, A. L. Borg, B. Lavraud, and M. G. G. T. Taylor. Energy Partition in Magnetic Reconnection in Earth's Magnetotail. *Physical Review Letters*, 110(22):225001, May 2013. doi: 10.1103/PhysRevLett.110.225001.

[35] J. Egedal, W. Daughton, J. F. Drake, N. Katz, and A. Lê. Formation of a localized acceleration potential during magnetic reconnection with a guide field. *Physics of Plasmas*, 16(5):050701, May 2009. doi: 10.1063/1.3130732.

[36] J. Egedal, A. Lê, Y. Zhu, W. Daughton, M. Øieroset, T. Phan, R. P. Lin, and J. P. Eastwood. Cause of super-thermal electron heating during magnetotail reconnection. *Geophysical Research Letters*, 37:L10102, May 2010. doi: 10.1029/2010GL043487.

[37] J. Egedal, W. Daughton, and A. Le. Large-scale electron acceleration by parallel electric fields during magnetic reconnection. *Nature Physics*, 8:321–324, April 2012. doi: 10.1038/nphys2249.

[38] C. P. Escoubet, R. Schmidt, and M. L. Goldstein. Cluster - Science and Mission Overview. *Space Science Reviews*, 79, January 1997.

[39] A.N. Fazakerley and the PEACE Operations Team. *User Guide to the PEACE measurements in the Cluster Active Archive*. Doc.No.: CAA-EST-UG-PEA, Issue: 2.5, ESA, 2015.

[40] W. C. Feldman, S. J. Bame, S. P. Gary, J. T. Gosling, D. McComas, M. F. Thomsen, G. Paschmann, N. Sckopke, M. M. Hoppe, and C. T. Russell. Electron heating within the earth's bow shock. *Physical Review Letters*, 49:199–201, July 1982. doi: 10.1103/PhysRevLett.49.199.

[41] H. S. Fu, Y. V. Khotyaintsev, A. Vaivads, A. Retinò, and M. André. Energetic electron acceleration by unsteady magnetic reconnection. *Nature Physics*, 9:426–430, July 2013. doi: 10.1038/nphys2664.

[42] M. Fujimoto, I. Shinohara, and H. Kojima. Reconnection and waves: A review with a perspective. *Space Science Reviews*, 160(1-4):123–143, 2011. ISSN 0038-6308. doi: 10.1007/s11214-011-9807-7.

[43] P. W. Daly G. Paschmann. *Analysis Methods for Multi-Spacecraft Data*. International Space Science Institute, Bern, Switzerland, 2000.

[44] J. T. Gosling. Observations of Magnetic Reconnection in the Turbulent High-Speed Solar Wind. *Astrophysical Journal, Letters*, 671:L73–L76, December 2007. doi: 10.1086/524842.

[45] D. B. Graham, Y. V. Khotyaintsev, A. Vaivads, M. André, and A. N. Fazakerley. Electron Dynamics in the Diffusion Region of an Asymmetric Magnetic Reconnection. *Physical Review Letters*, 112(21):215004, May 2014. doi: 10.1103/PhysRevLett.112.215004.

[46] H. L. Grant and A. Moilliet. The spectrum of a cross-stream component of turbulence in a tidal stream. *Journal of Fluid Mechanics*, 13:237–240, 6 1962. ISSN 1469-7645. doi: 10.1017/S0022112062000658.

[47] A. Greco, P. Chuychai, W. H. Matthaeus, S. Servidio, and P. Dmitruk. Intermittent MHD structures and classical discontinuities. *Geophysical Research Letters*, 35:L19111, October 2008. doi: 10.1029/2008GL035454.

[48] A. Greco, W. H. Matthaeus, S. Servidio, P. Chuychai, and P. Dmitruk. Statistical Analysis of Discontinuities in Solar Wind ACE Data and Comparison with Intermittent MHD Turbulence. *Astrophysical Journal Letters*, 691:L111–L114, February 2009. doi: 10.1088/0004-637X/691/2/L111.

[49] F. Guo, Y.-H. Liu, W. Daughton, and H. Li. Particle Acceleration and Plasma Dynamics during Magnetic Reconnection in the Magnetically Dominated Regime. *Astrophysical Journal*, 806:167, June 2015. doi: 10.1088/0004-637X/806/2/167.

[50] G. Gustafsson, R. Bostrom, B. Holback, G. Holmgren, A. Lundgren, K. Stasiewicz, L. Ahlen, F. S. Mozer, D. Pankow, P. Harvey, P. Berg, R. Ulrich, A. Pedersen, R. Schmidt, A. Butler, A. W. C. Fransen, D. Klinge, M. Thomsen, C.-G. Falthammar, P.-A. Lindqvist, S. Christenson, J. Holtet, B. Lybekk, T. A. Sten, P. Tanskanen, K. Lappalainen, and J. Wygant. The Electric Field and Wave Experiment for the Cluster Mission. *Space Science Reviews*, 79:137–156, January 1997. doi: 10.1023/A:1004975108657.

[51] E. Lucek P. Brown L. N. Alconcel T. Oddy H. Lewtas, C. Carr. *User Guide to the FGM measurements in the Cluster Active Archive*. Doc.No.: CAA-EST-UG-FGM, Issue: 6, ESA, 2015.

[52] L. Hadid. Nature of the MHD and kinetic scale turbulence in the magnetosheath of Saturn: Cassini Observations. *In review, The Astrophysical Journal, Letters*, 2015.

[53] C. T. Haynes, D. Burgess, and E. Camporeale. Reconnection and Electron Temperature Anisotropy in Sub-proton Scale Plasma Turbulence. *The Astrophysical Journal*, 783:38, March 2014. doi: 10.1088/0004-637X/783/1/38.

[54] M. Hoshino. Stochastic Particle Acceleration in Multiple Magnetic Islands during Reconnection. *Physical Review Letters*, 108(13):135003, March 2012. doi: 10.1103/PhysRevLett.108.135003.

[55] M. Hoshino, K. Hiraide, and T. Mukai. Strong electron heating and non-Maxwellian behavior in magnetic reconnection. *Earth, Planets, and Space*, 53:627–634, June 2001. doi: 10.1186/BF03353282.

[56] G. G. Howes, J. M. Tenbarge, and W. Dorland. A weakened cascade model for turbulence in astrophysical plasmas. *Physics of Plasmas*, 18(10):102305, October 2011. doi: 10.1063/1.3646400.

[57] S. Y. Huang, A. Vaivads, Y. V. Khotyaintsev, M. Zhou, H. S. Fu, A. Retinò, X. H. Deng, M. André, C. M. Cully, J. S. He, F. Sahraoui, Z. G. Yuan, and Y. Pang. Electron acceleration in the reconnection diffusion region: Cluster observations. *Geophysical Research Letters*, 39:L11103, June 2012. doi: 10.1029/2012GL051946.

[58] S. Y. Huang, F. Sahraoui, X. H. Deng, J. S. He, Z. G. Yuan, M. Zhou, Y. Pang, and H. S. Fu. Kinetic turbulence in the terrestrial magnetosheath: Cluster observations. *Astrophysical Journal Letters*, 789(2):L28, 2014.

[59] P. S. Iroshnikov. Turbulence of a Conducting Fluid in a Strong Magnetic Field. *Soviet Astronomy*, 7:566, February 1964.

[60] Harald Jeszenszky. *User Guide to the ASPOC measurements in the Cluster Active Archive*. Doc.No.: CAA-EST-UG-ASP, Issue: 1.0, ESA, 2015.

[61] H. Karimabadi and A. Lazarian. Magnetic reconnection in the presence of externally driven and self-generated turbulence. *Physics of Plasmas*, 20(11): 112102, November 2013. doi: 10.1063/1.4828395.

[62] H. Karimabadi, W. Daughton, and J. Scudder. Multi-scale structure of the electron diffusion region. *Geophysical Research Letters*, 34:L13104, July 2007. doi: 10.1029/2007GL030306.

[63] H. Karimabadi, V. Roytershteyn, H. X. Vu, Y. A. Omelchenko, J. Scudder, W. Daughton, A. Dimmock, K. Nykyri, M. Wan, D. Sibeck, M. Tatineni, A. Majumdar, B. Loring, and B. Geveci. The link between shocks, turbulence, and magnetic reconnection in collisionless plasmas. *Physics of Plasmas*, 21(6):062308, June 2014. doi: 10.1063/1.4882875.

[64] Y. V. Khotyaintsev, A. Vaivads, A. Retinò, M. André, C. J. Owen, and H. Nilsson. Formation of Inner Structure of a Reconnection Separatrix Region. *Physical Review Letters*, 97(20):205003, November 2006. doi: 10.1103/PhysRevLett.97.205003.

[65] Y. V. Khotyaintsev, A. Vaivads, M. André, M. Fujimoto, A. Retinò, and C. J. Owen. Observations of Slow Electron Holes at a Magnetic Reconnection Site. *Physical Review Letters*, 105(16):165002, October 2010. doi: 10.1103/PhysRevLett.105.165002.

[66] Y. V. Khotyaintsev, C. M. Cully, A. Vaivads, M. André, and C. J. Owen. Plasma Jet Braking: Energy Dissipation and Nonadiabatic Electrons. *Physical Review Letters*, 106(16):165001, April 2011. doi: 10.1103/PhysRevLett.106.165001.

[67] Khurom H. Kiyani, Kareem T. Osman, and Sandra C. Chapman. *Dissipation and heating in solar wind turbulence: from the macro to the micro and back again*, volume 373. The Royal Society, 2015. ISBN 1471-2962. doi: 10.1098/rsta.2014.0155.

[68] A. Kolmogorov. The Local Structure of Turbulence in Incompressible Viscous Fluid for Very Large Reynolds' Numbers. *Akademiia Nauk SSSR Doklady*, 30:301–305, 1941.

[69] G. Kowal, A. Lazarian, E. T. Vishniac, and K. Otmianowska-Mazur. Numerical Tests of Fast Reconnection in Weakly Stochastic Magnetic Fields. *The Astrophysical Journal*, 700:63–85, July 2009. doi: 10.1088/0004-637X/700/1/63.

[70] G. Kowal, E. M. de Gouveia Dal Pino, and A. Lazarian. Magnetohydrodynamic Simulations of Reconnection and Particle Acceleration: Three-dimensional Effects. *Astrophysical Journal*, 735:102, July 2011. doi: 10.1088/0004-637X/735/2/102.

[71] R. H. Kraichnan. Inertial-Range Spectrum of Hydromagnetic Turbulence. *Physics of Fluids*, 8:1385–1387, July 1965. doi: 10.1063/1.1761412.

[72] B. Lavraud, M. J. Owens, and A. P. Rouillard. In Situ Signatures of Interchange Reconnection between Magnetic Clouds and Open Magnetic Fields: A Mechanism for the Erosion of Polar Coronal Holes? *Solar Physics*, 270: 285–296, May 2011. doi: 10.1007/s11207-011-9717-6.

[73] B. Lavraud, A. Ruffenach, A. P. Rouillard, P. Kajdic, W. B. Manchester, and N. Lugaz. Geo-effectiveness and radial dependence of magnetic cloud erosion by magnetic reconnection. *Journal of Geophysical Research (Space Physics)*, 119:26–35, January 2014. doi: 10.1002/2013JA019154.

[74] A. Lazarian and E. T. Vishniac. Reconnection in a Weakly Stochastic Field. *Astrophysical Journal*, 517:700–718, June 1999. doi: 10.1086/307233.

[75] A. Lazarian, G. L. Eyink, and E. T. Vishniac. Relation of astrophysical turbulence and magnetic reconnection. *Physics of Plasmas*, 19(1):012105, January 2012. doi: 10.1063/1.3672516.

[76] A. Lazarian, L. Vlahos, G. Kowal, H. Yan, A. Beresnyak, and E. M. de Gouveia Dal Pino. Turbulence, Magnetic Reconnection in Turbulent Fluids and Energetic Particle Acceleration. *Space Science Reviews*, 173:557–622, November 2012. doi: 10.1007/s11214-012-9936-7.

[77] A. Le, J. Egedal, W. Daughton, J. F. Drake, W. Fox, and N. Katz. Magnitude of the Hall fields during magnetic reconnection. *Geophysical Research Letters*, 37:L03106, February 2010. doi: 10.1029/2009GL041941.

[78] A. Le, J. Egedal, O. Ohia, W. Daughton, H. Karimabadi, and V. S. Lukin. Regimes of the Electron Diffusion Region in Magnetic Reconnection. *Physical Review Letters*, 110(13):135004, March 2013. doi: 10.1103/PhysRevLett.110.135004.

[79] G. R. Lewis, N. André, C. S. Arridge, A. J. Coates, L. K. Gilbert, D. R. Linder, and A. M. Rymer. Derivation of density and temperature from the Cassini Huygens CAPS electron spectrometer. *Planetary and Space Science*, 56:901–912, May 2008. doi: 10.1016/j.pss.2007.12.017.

[80] N. F. Loureiro, D. A. Uzdensky, A. A. Schekochihin, S. C. Cowley, and T. A. Yousef. Turbulent magnetic reconnection in two dimensions. *Monthly*

Notices of the Royal Astronomical Society, 399:L146–L150, October 2009. doi: 10.1111/j.1745-3933.2009.00742.x.

[81] N. F. Loureiro, A. A. Schekochihin, and A. Zocco. Fast Collisionless Reconnection and Electron Heating in Strongly Magnetized Plasmas. *Physical Review Letters*, 111(2):025002, July 2013. doi: 10.1103/PhysRevLett.111.025002.

[82] E. A. Lucek, D. Constantinescu, M. L. Goldstein, J. Pickett, J. L. Pincon, F. Sahraoui, R. A. Treumann, and S. N. Walker. The magnetosheath. *Space Science Reviews*, 118(1-4):95–152, 2005. ISSN 0038-6308. doi: 10.1007/s11214-005-3825-2. URL `http://dx.doi.org/10.1007/s11214-005-3825-2`.

[83] H. Maehara, T. Shibayama, S. Notsu, Y. Notsu, T. Nagao, S. Kusaba, S. Honda, D. Nogami, and K. Shibata. Superflares on solar-type stars. *Nature*, 485:478–481, May 2012. doi: 10.1038/nature11063.

[84] M. Maksimovic, I. Zouganelis, J.-Y. Chaufray, K. Issautier, E. E. Scime, J. E. Littleton, E. Marsch, D. J. McComas, C. Salem, R. P. Lin, and H. Elliott. Radial evolution of the electron distribution functions in the fast solar wind between 0.3 and 1.5 au. *Journal of Geophysical Research: Space Physics*, 110 (A9):n/a–n/a, 2005. ISSN 2156-2202. doi: 10.1029/2005JA011119. A09104.

[85] M. E. Mandt, R. E. Denton, and J. F. Drake. Transition to whistler mediated magnetic reconnection. *Geophysical Research Letters*, 21:73–76, January 1994. doi: 10.1029/93GL03382.

[86] E. Marsch. *Reviews in Modern Astronomy*, chapter Turbulence in the solar wind. Springer, 1990.

[87] Eckart Marsch. Kinetic physics of the solar corona and solar wind. *Living Reviews in Solar Physics*, 3(1), 2006. doi: 10.12942/lrsp-2006-1.

[88] A. Masters, L. Stawarz, M. Fujimoto, S. J. Schwartz, N. Sergis, M. F. Thomsen, A. Retinò, H. Hasegawa, B. Zieger, G. R. Lewis, A. J. Coates, P. Canu, and M. K. Dougherty. Electron acceleration to relativistic energies at a strong quasi-parallel shock wave. *Nature Physics*, 9:164–167, March 2013. doi: 10.1038/nphys2541.

[89] Y. Matsumoto, T. Amano, T. N. Kato, and M. Hoshino. Stochastic electron acceleration during spontaneous turbulent reconnection in a strong shock wave. *Science*, 347(6225):974–978, 2015. doi: 10.1126/science.1260168.

[90] W. H. Matthaeus and S. L. Lamkin. Turbulent magnetic reconnection. *Physics of Fluids*, 29:2513–2534, August 1986. doi: 10.1063/1.866004.

[91] W. H. Matthaeus and D. Montgomery. Selective decay hypothesis at high mechanical and magnetic Reynolds numbers. *Annals of the New York Academy of Sciences*, 357:203–222, December 1980. doi: 10.1111/j.1749-6632.1980.tb29687.x.

[92] W. H. Matthaeus and M. Velli. Who Needs Turbulence?. A Review of Turbulence Effects in the Heliosphere and on the Fundamental Process of Reconnection. *Space Science Reviews*, 160:145–168, October 2011. doi: 10.1007/s11214-011-9793-9.

[93] W. H. Matthaeus and Y. Zhou. Extended inertial range phenomenology of magnetohydrodynamic turbulence. *Physics of Fluids B*, 1:1929–1931, September 1989. doi: 10.1063/1.859110.

[94] W. H. Matthaeus, J. J. Ambrosiano, and M. L. Goldstein. Particle-acceleration by turbulent magnetohydrodynamic reconnection. *Physical Review Letters*, 53:1449–1452, October 1984. doi: 10.1103/PhysRevLett.53.1449.

[95] W. H. Matthaeus, S. Dasso, J. M. Weygand, L. J. Milano, C. W. Smith, and M. G. Kivelson. Spatial Correlation of Solar-Wind Turbulence from Two-Point Measurements. *Physical Review Letters*, 95(23):231101, December 2005. doi: 10.1103/PhysRevLett.95.231101.

[96] William H. Matthaeus and Melvyn L. Goldstein. Measurement of the rugged invariants of magnetohydrodynamic turbulence in the solar wind. *Journal of Geophysical Research: Space Physics*, 87(A8):6011–6028, 1982. ISSN 2156-2202. doi: 10.1029/JA087iA08p06011. URL `http://dx.doi.org/10.1029/JA087iA08p06011`.

[97] B. Miao, B. Peng, and G. Li. Current sheets from Ulysses observation. *Annales Geophysicae*, 29:237–249, February 2011. doi: 10.5194/angeo-29-237-2011.

[98] F. S. Mozer, S. D. Bale, and T. D. Phan. Evidence of Diffusion Regions at a Subsolar Magnetopause Crossing. *Physical Review Letters*, 89(1):015002, June 2002. doi: 10.1103/PhysRevLett.89.015002.

[99] F. S. Mozer, S. D. Bale, T. D. Phan, and J. A. Osborne. Observations of Electron Diffusion Regions at the Subsolar Magnetopause. *Physical Review Letters*, 91(24):245002, December 2003. doi: 10.1103/PhysRevLett.91.245002.

[100] C. Lacombe N. Cornilleau-Wehrlin, Rodrigue Piberne and STAFF team. *User Guide to the STAFF measurements in the Cluster Active Archive*. Doc.No.: CAA-EST-UG-002, Issue: 3.4, ESA.

[101] R. Nakamura, W. Baumjohann, Y. Asano, A. Runov, A. Balogh, C. J. Owen, A. N. Fazakerley, M. Fujimoto, B. Klecker, and H. RèMe. Dynamics of thin current sheets associated with magnetotail reconnection. *Journal of Geophysical Research (Space Physics)*, 111:A11206, November 2006. doi: 10.1029/2006JA011706.

[102] C. Norgren, A. Vaivads, Y. V. Khotyaintsev, and M. André. Lower Hybrid Drift Waves: Space Observations. *Physical Review Letters*, 109(5):055001, August 2012. doi: 10.1103/PhysRevLett.109.055001.

[103] M. Øieroset, T. D. Phan, M. Fujimoto, R. P. Lin, and R. P. Lepping. In situ detection of collisionless reconnection in the Earth's magnetotail. *Nature*, 412:414–417, July 2001. doi: 10.1038/35086520.

[104] K. T. Osman, W. H. Matthaeus, A. Greco, and S. Servidio. Evidence for Inhomogeneous Heating in the Solar Wind. *Astrophysical Journal Letters*, 727:L11, January 2011. doi: 10.1088/2041-8205/727/1/L11.

[105] K. T. Osman, W. H. Matthaeus, J. T. Gosling, A. Greco, S. Servidio, B. Hnat, S. C. Chapman, and T. D. Phan. Magnetic Reconnection and Intermittent Turbulence in the Solar Wind. *ArXiv e-prints*, March 2014.

[106] E. N. Parker. Sweet's Mechanism for Merging Magnetic Fields in Conducting Fluids. *Journal of Geophysical Research (Space Physics)*, 62:509–520, December 1957. doi: 10.1029/JZ062i004p00509.

[107] G. Paschmann. Space Physics: Breaking through the lines. *Nature*, 439: 144–145, January 2006. doi: 10.1038/439144a.

[108] A. Pedersen. Solar wind and magnetosphere plasma diagnostics by spacecraft electrostatic potential measurements. *Annales Geophysicae*, 13:118–129, February 1995. doi: 10.1007/s00585-995-0118-8.

[109] A. Pedersen, B. Lybekk, M. André, A. Eriksson, A. Masson, F. S. Mozer, P.-A. Lindqvist, P. M. E. DéCréAu, I. Dandouras, J.-A. Sauvaud, A. Fazakerley, M. Taylor, G. Paschmann, K. R. Svenes, K. Torkar, and E. Whipple. Electron density estimations derived from spacecraft potential measurements on Cluster in tenuous plasma regions. *Journal of Geophysical Research (Space Physics)*, 113:A07S33, July 2008. doi: 10.1029/2007JA012636.

[110] Yuri Khotyaintsev Per-Arne Lindqvist, Chris Cully and the EFW team. *User Guide to the EFW measurements in the Cluster Active Archive*. Doc.No.: CAA-EST-UG-EFW, Issue: 3.5, ESA, 2015.

[111] S. Perri, M. L. Goldstein, J. C. Dorelli, and F. Sahraoui. Detection of Small-Scale Structures in the Dissipation Regime of Solar-Wind Turbulence. *Physical Review Letters*, 109(19):191101, November 2012. doi: 10.1103/PhysRevLett.109.191101.

[112] T. D. Phan, L. M. Kistler, B. Klecker, G. Haerendel, G. Paschmann, B. U. Ö. Sonnerup, W. Baumjohann, M. B. Bavassano-Cattaneo, C. W. Carlson, A. M. DiLellis, K.-H. Fornacon, L. A. Frank, M. Fujimoto, E. Georgescu, S. Kokubun, E. Moebius, T. Mukai, M. Øieroset, W. R. Paterson, and H. Reme. Extended magnetic reconnection at the Earth's magnetopause from detection of bi-directional jets. *Nature*, 404:848–850, April 2000.

[113] T. D. Phan, J. F. Drake, M. A. Shay, F. S. Mozer, and J. P. Eastwood. Evidence for an Elongated (60 Ion Skin Depths) Electron Diffusion Region during Fast Magnetic Reconnection. *Physical Review Letters*, 99(25):255002, December 2007. doi: 10.1103/PhysRevLett.99.255002.

[114] T. D. Phan, M. A. Shay, J. T. Gosling, M. Fujimoto, J. F. Drake, G. Paschmann, M. Oieroset, J. P. Eastwood, and V. Angelopoulos. Electron bulk heating in magnetic reconnection at Earth's magnetopause: Dependence on the inflow Alfvén speed and magnetic shear. *Geophysical Research Letters*, 40:4475–4480, September 2013. doi: 10.1002/grl.50917.

[115] W. G. Pilipp, H. Miggenrieder, M. D. Montgomery, K. H. Mhlhuser, H. Rosenbauer, and R. Schwenn. Unusual electron distribution functions

in the solar wind derived from the helios plasma experiment: Double-strahl distributions and distributions with an extremely anisotropic core. *Journal of Geophysical Research: Space Physics*, 92(A2):1093–1101, 1987. ISSN 2156-2202. doi: 10.1029/JA092iA02p01093.

[116] E. Priest and T. Forbes, editors. *Magnetic reconnection : MHD theory and applications*, 2000.

[117] P. L. Pritchett. Collisionless magnetic reconnection in a three-dimensional open system. *Journal of Geophysical Research: Space Physics*, 106(A11): 25961–25977, 2001. ISSN 2156-2202. doi: 10.1029/2001JA000016.

[118] P. L. Pritchett. Geospace environment modeling magnetic reconnection challenge: Simulations with a full particle electromagnetic code. *Journal of Geophysical Research: Space Physics*, 106(A3):3783–3798, 2001. ISSN 2156-2202. doi: 10.1029/1999JA001006.

[119] P. L. Pritchett. Relativistic electron production during guide field magnetic reconnection. *Journal of Geophysical Research (Space Physics)*, 111:A10212, October 2006. doi: 10.1029/2006JA011793.

[120] P. L. Pritchett and F. V. Coroniti. Three-dimensional collisionless magnetic reconnection in the presence of a guide field. *Journal of Geophysical Research (Space Physics)*, 109:A01220, January 2004. doi: 10.1029/2003JA009999.

[121] M. P. Pulupa, C. Salem, T. D. Phan, J. T. Gosling, and S. D. Bale. Core Electron Heating in Solar Wind Reconnection Exhausts. *Astrophysical Journal, Letters*, 791:L17, August 2014. doi: 10.1088/2041-8205/791/1/L17.

[122] Y. Ren, M. Yamada, S. Gerhardt, H. Ji, R. Kulsrud, and A. Kuritsyn. Experimental Verification of the Hall Effect during Magnetic Reconnection in a Laboratory Plasma. *Physical Review Letters*, 95(5):055003, July 2005. doi: 10.1103/PhysRevLett.95.055003.

[123] A. Retinò, A. Vaivads, M. André, F. Sahraoui, Y. Khotyaintsev, J. S. Pickett, M. B. Bavassano Cattaneo, M. F. Marcucci, M. Morooka, C. J. Owen, S. C. Buchert, and N. Cornilleau-Wehrlin. Structure of the separatrix region close to a magnetic reconnection X-line: Cluster observations. *Geophysical Research Letters*, 33:L06101, March 2006. doi: 10.1029/2005GL024650.

[124] A. Retinò, D. Sundkvist, A. Vaivads, F. Mozer, M. j André, and C. J. Owen. In situ evidence of magnetic reconnection in turbulent plasma. *Nature Physics*, 3:236–238, April 2007. doi: 10.1038/nphys574.

[125] A. Retinò, R. Nakamura, A. Vaivads, Y. Khotyaintsev, T. Hayakawa, K. Tanaka, S. Kasahara, M. Fujimoto, I. Shinohara, J. P. Eastwood, M. André, W. Baumjohann, P. W. Daly, E. A. Kronberg, and N. Cornilleau-Wehrlin. Cluster observations of energetic electrons and electromagnetic fields within a reconnecting thin current sheet in the Earth's magnetotail. *Journal of Geophysical Research (Space Physics)*, 113:A12215, December 2008. doi: 10.1029/2008JA013511.

[126] D. A. Roberts and M. L. Goldstein. Turbulence and waves in the solar wind. *Reviews of Geophysics Supplement*, 29:932–943, 1991.

[127] A. Ruffenach, B. Lavraud, M. J. Owens, J.-A. Sauvaud, N. P. Savani, A. P. Rouillard, P. Démoulin, C. Foullon, A. Opitz, A. Fedorov, C. J. Jacquey, V. Génot, P. Louarn, J. G. Luhmann, C. T. Russell, C. J. Farrugia, and A. B. Galvin. Multispacecraft observation of magnetic cloud erosion by magnetic reconnection during propagation. *Journal of Geophysical Research (Space Physics)*, 117:A09101, September 2012. doi: 10.1029/2012JA017624.

[128] A. Ruffenach, B. Lavraud, C. J. Farrugia, P. Démoulin, S. Dasso, M. J. Owens, J.-A. Sauvaud, A. P. Rouillard, A. Lynnyk, C. Foullon, N. P. Savani, J. G. Luhmann, and A. B. Galvin. Statistical study of magnetic cloud erosion by magnetic reconnection. *Journal of Geophysical Research (Space Physics)*, 120:43–60, January 2015. doi: 10.1002/2014JA020628.

[129] F. Sahraoui, M. L. Goldstein, P. Robert, and Y. V. Khotyaintsev. Evidence of a Cascade and Dissipation of Solar-Wind Turbulence at the Electron Gyroscale. *Physical Review Letters*, 102(23):231102, June 2009. doi: 10.1103/PhysRevLett.102.231102.

[130] F. Sahraoui, M. L. Goldstein, G. Belmont, P. Canu, and L. Rezeau. Three Dimensional Anisotropic k Spectra of Turbulence at Subproton Scales in the Solar Wind. *Physical Review Letters*, 105(13):131101, September 2010. doi: 10.1103/PhysRevLett.105.131101.

[131] K. Schindler, M. Hesse, and J. Birn. General magnetic reconnection, parallel electric fields, and helicity. *Journal of Geophysical Research (Space Physics)*, 93:5547–5557, June 1988. doi: 10.1029/JA093iA06p05547.

[132] S. J. Schwartz, E. Henley, J. Mitchell, and V. Krasnoselskikh. Electron Temperature Gradient Scale at Collisionless Shocks. *Physical Review Letters*, 107(21):215002, November 2011. doi: 10.1103/PhysRevLett.107.215002.

[133] J. D. Scudder, R. D. Holdaway, W. S. Daughton, H. Karimabadi, V. Roytershteyn, C. T. Russell, and J. Y. Lopez. First Resolved Observations of the Demagnetized Electron-Diffusion Region of an Astrophysical Magnetic-Reconnection Site. *Physical Review Letters*, 108(22):225005, June 2012. doi: 10.1103/PhysRevLett.108.225005.

[134] S. Servidio, W. H. Matthaeus, M. A. Shay, P. A. Cassak, and P. Dmitruk. Magnetic Reconnection in Two-Dimensional Magnetohydrodynamic Turbulence. *Physical Review Letters*, 102(11):115003, March 2009. doi: 10.1103/PhysRevLett.102.115003.

[135] S. Servidio, A. Greco, W. H. Matthaeus, K. T. Osman, and P. Dmitruk. Statistical association of discontinuities and reconnection in magnetohydrodynamic turbulence. *Journal of Geophysical Research (Space Physics)*, 116: A09102, September 2011. doi: 10.1029/2011JA016569.

[136] M. A. Shay, C. C. Haggerty, T. D. Phan, J. F. Drake, P. A. Cassak, P. Wu, M. Oieroset, M. Swisdak, and K. Malakit. Electron heating during magnetic reconnection: A simulation scaling study. *Physics of Plasmas*, 21(12): 122902, December 2014. doi: 10.1063/1.4904203.

[137] K. Shibata and S. Tanuma. Plasmoid-induced-reconnection and fractal reconnection. *Earth, Planets, and Space*, 53:473–482, June 2001.

[138] K. Shibata, T. Nakamura, T. Matsumoto, K. Otsuji, T. J. Okamoto, N. Nishizuka, T. Kawate, H. Watanabe, S. Nagata, S. UeNo, R. Kitai, S. Nozawa, S. Tsuneta, Y. Suematsu, K. Ichimoto, T. Shimizu, Y. Katsukawa, T. D. Tarbell, T. E. Berger, B. W. Lites, R. A. Shine, and A. M. Title. Chromospheric Anemone Jets as Evidence of Ubiquitous Reconnection. *Science*, 318:1591–, December 2007. doi: 10.1126/science.1146708.

[139] I. Shinohara and M. Hoshino. Electron heating process of the lower hybrid drift instability. *Advances in Space Research*, 24:43–46, January 1999. doi: 10.1016/S0273-1177(99)00420-2.

[140] J. R. Shuster, L.-J. Chen, M. Hesse, M. R. Argall, W. Daughton, R. B. Torbert, and N. Bessho. Spatiotemporal evolution of electron characteristics in the electron diffusion region of magnetic reconnection: Implications for acceleration and heating. *Geophysical Research Letters*, 42:2586–2593, April 2015. doi: 10.1002/2015GL063601.

[141] D. Sundkvist, A. Retinò, A. Vaivads, and S. D. Bale. Dissipation in Turbulent Plasma due to Reconnection in Thin Current Sheets. *Physical Review Letters*, 99(2):025004, July 2007. doi: 10.1103/PhysRevLett.99.025004.

[142] P. A. Sweet. The Neutral Point Theory of Solar Flares. In B. Lehnert, editor, *Electromagnetic Phenomena in Cosmical Physics*, volume 6 of *IAU Symposium*, page 123, 1958.

[143] M. Swisdak and J. F. Drake. Orientation of the reconnection X-line. *Geophysical Research Letters*, 34:L11106, June 2007. doi: 10.1029/2007GL029815.

[144] M. Swisdak, J. F. Drake, M. A. Shay, and J. G. McIlhargey. Transition from antiparallel to component magnetic reconnection. *Journal of Geophysical Research (Space Physics)*, 110:A05210, May 2005. doi: 10.1029/2004JA010748.

[145] Xiangwei Tang, Cynthia Cattell, John Dombeck, Lei Dai, Lynn B. Wilson, Aaron Breneman, and Adam Hupach. Themis observations of the magnetopause electron diffusion region: Large amplitude waves and heated electrons. *Geophysical Research Letters*, 40(12):2884–2890, 2013. ISSN 1944-8007. doi: 10.1002/grl.50565.

[146] The WHISPER team. *User Guide to the WHISPER Science Datasets in the Cluster Active Archive*. Doc.No.: CAA-EST-UG-WHI, Issue: 1.4, ESA, 2015.

[147] J. M. TenBarge, G. G. Howes, and W. Dorland. Collisionless Damping at Electron Scales in Solar Wind Turbulence. *The Astrophysical Journal*, 774:139, September 2013. doi: 10.1088/0004-637X/774/2/139.

[148] R. A. Treumann and W. Baumjohann. Collisionless Magnetic Reconnection in Space Plasmas. *ArXiv e-prints*, January 2014.

[149] A. Vaivads, M. André, S. C. Buchert, J.-E. Wahlund, A. N. Fazakerley, and N. Cornilleau-Wehrlin. Cluster observations of lower hybrid turbulence within thin layers at the magnetopause. *Geophysical Research Letters*, 31: L03804, February 2004. doi: 10.1029/2003GL018142.

[150] A. Vaivads, Y. Khotyaintsev, M. André, A. Retinò, S. C. Buchert, B. N. Rogers, P. Décréau, G. Paschmann, and T. D. Phan. Structure of the Magnetic Reconnection Diffusion Region from Four-Spacecraft Observations. *Physical Review Letters*, 93(10):105001, August 2004. doi: 10.1103/PhysRevLett.93.105001.

[151] Andris Vaivads, Alessandro Retin, and Mats Andr. Microphysics of magnetic reconnection. *Space Science Reviews*, 122(1-4):19–27, 2006. ISSN 0038-6308. doi: 10.1007/s11214-006-7019-3.

[152] A. Varsani, C. J. Owen, A. N. Fazakerley, C. Forsyth, A. P. Walsh, M. André, I. Dandouras, and C. M. Carr. Cluster observations of the substructure of a flux transfer event: analysis of high-time-resolution particle data. *Annales Geophysicae*, 32:1093–1117, September 2014. doi: 10.5194/angeo-32-1093-2014.

[153] L. Vlahos, H. Isliker, and F. Lepreti. Particle Acceleration in an Evolving Network of Unstable Current Sheets. *Astrophysical Journal*, 608:540–553, June 2004. doi: 10.1086/386364.

[154] M. von Papen, J. Saur, and O. Alexandrova. Turbulent magnetic field fluctuations in Saturn's magnetosphere. *Journal of Geophysical Research (Space Physics)*, 119:2797–2818, April 2014. doi: 10.1002/2013JA019542.

[155] Z. Vörös, Y. L. Sasunov, V. S. Semenov, T. V. Zaqarashvili, R. Bruno, and M. Khodachenko. Reconnection Outflow Generated Turbulence in the Solar Wind. *Astrophysical Journal, Letters*, 797:L10, December 2014. doi: 10.1088/2041-8205/797/1/L10.

[156] M. Wan, W. H. Matthaeus, H. Karimabadi, V. Roytershteyn, M. Shay, P. Wu, W. Daughton, B. Loring, and S. C. Chapman. Intermittent Dissipation at Kinetic Scales in Collisionless Plasma Turbulence. *Physical Review*

Letters, 109(19):195001, November 2012. doi: 10.1103/PhysRevLett.109.195001.

[157] M. Wan, W. H. Matthaeus, V. Roytershteyn, H. Karimabadi, T. Parashar, P. Wu, and M. Shay. Intermittent Dissipation and Heating in 3D Kinetic Plasma Turbulence. *Physical Review Letters*, 114(17):175002, May 2015. doi: 10.1103/PhysRevLett.114.175002.

[158] T. Yokoyama, K. Akita, T. Morimoto, K. Inoue, and J. Newmark. Clear Evidence of Reconnection Inflow of a Solar Flare. *Astrophysical Journal, Letters*, 546:L69–L72, January 2001. doi: 10.1086/318053.

[159] E. Yordanova, A. Vaivads, M. André, S. C. Buchert, and Z. Vörös. Magnetosheath Plasma Turbulence and Its Spatiotemporal Evolution as Observed by the Cluster Spacecraft. *Physical Review Letters*, 100(20):205003, May 2008. doi: 10.1103/PhysRevLett.100.205003.

[160] G. P. Zank, J. A. le Roux, G. M. Webb, A. Dosch, and O. Khabarova. Particle Acceleration via Reconnection Processes in the Supersonic Solar Wind. *Astrophysical Journal*, 797:28, December 2014. doi: 10.1088/0004-637X/797/1/28.

[161] V. Zhdankin, S. Boldyrev, and J. Mason. Distribution of Magnetic Discontinuities in the Solar Wind and in Magnetohydrodynamic Turbulence. *Astrophysical Journal Letters*, 760:L22, December 2012. doi: 10.1088/2041-8205/760/2/L22.

[162] E. G. Zweibel and M. da. Magnetic Reconnection in Astrophysical and Laboratory Plasmas. *Annual Review of Astronomy and Astrophysics*, 47:291–332, September 2009. doi: 10.1146/annurev-astro-082708-101726.